

Winter 2010

# Modeling the self-assembly of functionalized fullerenes on solid surfaces using Monte Carlo simulations

Gregory J. Bubnis

*University of New Hampshire, Durham*

Follow this and additional works at: <https://scholars.unh.edu/dissertation>

---

## Recommended Citation

Bubnis, Gregory J., "Modeling the self-assembly of functionalized fullerenes on solid surfaces using Monte Carlo simulations" (2010). *Doctoral Dissertations*. 550.

<https://scholars.unh.edu/dissertation/550>

This Dissertation is brought to you for free and open access by the Student Scholarship at University of New Hampshire Scholars' Repository. It has been accepted for inclusion in Doctoral Dissertations by an authorized administrator of University of New Hampshire Scholars' Repository. For more information, please contact [nicole.hentz@unh.edu](mailto:nicole.hentz@unh.edu).

MODELING THE SELF-ASSEMBLY OF FUNCTIONALIZED  
FULLERENES ON SOLID SURFACES USING MONTE CARLO  
SIMULATIONS

BY

GREGORY J. BUBNIS  
B.S. Mathematics and Chemistry, University of New Hampshire, 2005

DISSERTATION

Submitted to the University of New Hampshire  
in Partial Fulfillment of  
the Requirements for the Degree of

Doctor of Philosophy  
in  
Chemistry

December, 2010

UMI Number: 3442545

All rights reserved

**INFORMATION TO ALL USERS**

The quality of this reproduction is dependent upon the quality of the copy submitted.

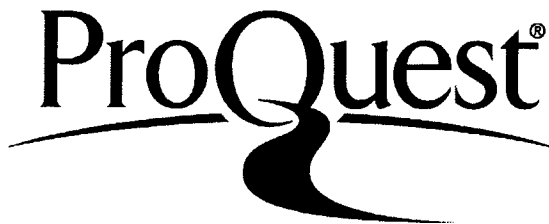
In the unlikely event that the author did not send a complete manuscript and there are missing pages, these will be noted. Also, if material had to be removed, a note will indicate the deletion.



UMI 3442545

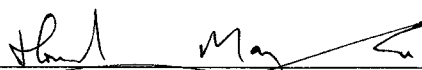
Copyright 2011 by ProQuest LLC.

All rights reserved. This edition of the work is protected against unauthorized copying under Title 17, United States Code.

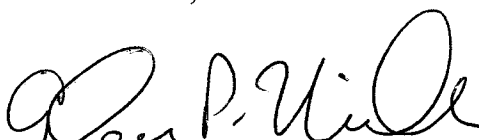


ProQuest LLC  
789 East Eisenhower Parkway  
P.O. Box 1346  
Ann Arbor, MI 48106-1346

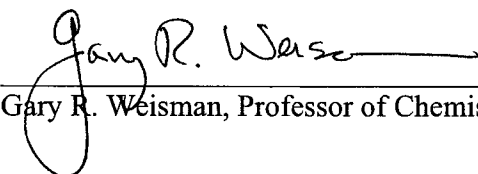
This dissertation has been examined and approved.

  
Dissertation Director, Howard R. Mayne,  
Professor of Chemistry

  
Adam Boucher, Lecturer in Mathematics

  
Glen P. Miller, Professor of Chemistry

  
Karsten Pohl, Associate Professor of Physics

  
Gary R. Weisman, Professor of Chemistry

11/24/2010  
Date

## ACKNOWLEDGEMENTS

The author wishes to acknowledge research support provided by the following sources:

The University of New Hampshire Graduate School

Dissertation Year Fellowship for the 2009-2010 Academic Year

The University of New Hampshire Chemistry Department

Pratt-Diniak Fellowship (2006)

Clarence L. and Helen M. Garland Grant Fellowship (2007 and 2008)

Craig A. West Memorial Award (2009)

The National Science Foundation

Research assistantships through The Center for High-Rate Nanomanufacturing  
under grant number NSF-0425826

TeraGrid resources through The National Center for Supercomputing  
Applications (NCSA) under grant number TG-CHE100096 used for  
calculations in Chapter IV

Computing resources through EPSCOR grant EPS-0701730 used for calculations  
in Chapter IV

## TABLE OF CONTENTS

ACKNOWLEDGEMENTS .....	iii
TABLE OF CONTENTS .....	iv
LIST OF TABLES .....	vi
LIST OF FIGURES .....	vii
LIST OF SYMBOLS AND NOTATION .....	ix
ABSTRACT .....	xi
I. INTRODUCTION .....	1
A. Motivation and Background .....	1
B. The Present Work .....	11
II. SELF-ASSEMBLY AND STRUCTURAL BEHAVIOR OF A MODEL RIGID C <sub>60</sub> - TERMINATED THIOLATE ON Au(111) .....	14
A. Introduction .....	14
B. Calculations .....	18
1. Model Rigid C <sub>60</sub> -terminated Thiolate .....	18
2. Potential Energy Function .....	18
3. Monte Carlo Calculations .....	20
C. Results and Discussion .....	22
D. Conclusions .....	29
III. SELF-ASSEMBLY OF VARIOUS HYDROGEN-BONDING FULLERENE DERIVATIVES ON Au(111) .....	30
A. Introduction .....	30
B. Molecules studied .....	36
C. Potential Energy Functions .....	37
1. UA-UA interactions .....	38
2. UA-Au(111) interactions .....	41
D. Simulation Methods .....	42
1. Monte Carlo Cooling .....	42
2. Energetics and Order Parameters .....	44
E. Results and Discussion .....	46
1. Neat C <sub>60</sub> .....	46
2. Molecule 1 .....	49
3. Molecule 2 .....	54
4. Molecule 3 .....	57
5. Molecule 4 .....	60
6. Molecule 5 .....	63
F. Conclusions .....	66
IV. FREE ENERGY LANDSCAPES OF BIS-FULLERENE CLUSTERS ON MODEL SURFACES .....	69
A. Introduction .....	69
B. Methods .....	74
1. Molecules Studied .....	74
2. The Coarse Grained Force Field .....	76
3. T-REMC Simulation Approach .....	78
4. Order Parameters (reduced coordinates) .....	82

5. Histogram Reweighting, Sampling Strategies, and Free Energy Surfaces.....	85
C. Results .....	90
1. Molecule 6 .....	90
2. Molecule 7 .....	103
3. Molecule 8 .....	112
D. Concluding Remarks.....	125
V. Appendix: Complete Potential Energy Functions.....	127
A. UA-UA interactions .....	127
B. UA-Surface interactions.....	128
VI. LIST OF REFERENCES.....	130

## LIST OF TABLES

TABLE	PAGE
Table III-I.....	38
Table V-I.....	127
Table V-II.....	129



## LIST OF FIGURES

FIGURE	PAGE
Figure II-1.....	23
Figure II-2.....	24
Figure II-3.....	26
Figure II-4.....	27
Figure II-5.....	28
Figure III-1.....	36
Figure III-2.....	39
Figure III-3.....	48
Figure III-4.....	49
Figure III-5.....	51
Figure III-6.....	52
Figure III-7.....	53
Figure III-8.....	55
Figure III-9.....	56
Figure III-10.....	58
Figure III-11.....	59
Figure III-12.....	61
Figure III-13.....	61
Figure III-14.....	64
Figure III-15.....	65
Figure IV-1.....	75
Figure IV-2.....	81
Figure IV-3.....	91
Figure IV-4.....	92
Figure IV-5.....	94
Figure IV-6.....	96
Figure IV-7.....	97
Figure IV-8.....	99
Figure IV-9.....	100
Figure IV-10.....	102
Figure IV-11.....	104
Figure IV-12.....	105
Figure IV-13.....	106
Figure IV-14.....	107
Figure IV-15.....	110
Figure IV-16.....	111
Figure IV-17.....	113
Figure IV-18.....	114
Figure IV-19.....	115
Figure IV-20.....	116
Figure IV-21.....	117
Figure IV-22.....	119

Figure IV-23.....	120
Figure IV-24.....	121
Figure IV-25.....	123

## LIST OF SYMBOLS AND NOTATION

### ABBREVIATIONS

CA	Carboxylic Acid (United Atom)
C <sub>60</sub>	[60]fullerene
MC	Monte Carlo
NN	Nearest Neighbor
PDF	Probability Density Function
Ph	Phenyl (United Atom)
PMF	Potential of Mean Force
REMC	Replica Exchange Monte Carlo
SRR	Short Range Repulsion
STM	Scanning Tunneling Microscopy
T-REMC	Temperature-REMC
UA	United Atom

### INDICES

$a, b$	histogram indices
$i, i'$	replica (or configuration) indices
$j, k$	molecule indices
$j', k'$	atom (UA) indices

### PROBABILITIES

$n$	histogram count
$p$	probability (density)

### CONSTANTS AND PARAMETERS

$k_B$	Boltzmann Constant
$N$	cluster size
$NR$	number of replicas
$T$	temperature
$T_{\min}, T_{\max}$	min and max of an ensemble $\{T_i\}$
$\beta$	inverse temperature ( $1/k_B T$ )
$\theta$	surface coverage density

### ENERGIES AND ASSOCIATED PARAMETERS

$A$	Helmholtz energy
$C_v$	heat capacity
$E$	pairwise potential well depth
$E_{CA}$	minimum energy for two H-Bonded CAs.
$E_{FG}$	fullerene-substrate binding energy
$E_{rep}$	prefactor for CA-substrate SRR
$k_{rep}$	constant for harmonic repulsion $U_{rep}$
$r_e$	preferred separation (LJ, Morse, etc.)
$U$	total system potential energy (sum of $U_{HB}, U_{vdW}, U_{surf}$ )

$U_{ang}$	angle dependent term for the CA-CA potential
$U_{CA-CA}$	CA-CA pairwise potential energy
$U_{HB}$	H-Bonding potential energy
$U_M$	Morse potential
$U_{rep}$	harmonic repulsive potential
$U_{surf}$	surface-adsorbate potential energy
$U_{vdW}$	vdW potential energy
$\rho$	range parameter for CA-CA Morse potential
$\sigma$	patch width for $U_{ang}$
$\kappa$	range parameter for CA-substrate SRR

### COORDINATES, REDUCED COORDINATES, AND ORDER PARAMETERS

$C60ML$	count of surface adsorbed fullerenes
$HBNN$	NN Hydrogen-Bond count
$HB2$	dimer H-Bond count
$\mathbf{p}$	patch vector (assigned to a CA group)
$P_{2x}$	NN $\mathbf{x}_{bf}$ axis alignment
$P_{2z}$	NN $\mathbf{z}_{bf}$ axis alignment
$P_{2t}$	tilt of $\mathbf{z}_{bf}$ axis compared to $\mathbf{z}$
$PhNN$	NN Ph-Ph count
$\mathbf{r}_{j,k}$	vector connecting atoms $j'$ and $k'$
$r_{j,k}$	distance between atoms $j'$ and $k'$ ( $r =  \mathbf{r} $ )
$\mathbf{x}_{bf} \mathbf{y}_{bf} \mathbf{z}_{bf}$	Body-fixed (molecule frame) axis vectors
$\mathbf{x} \mathbf{y} \mathbf{z}$	space fixed cartesian axis vectors
$\Phi_{j,k}$	the azimuth angle of $\mathbf{r}_{j,k}$ (projected on the x-y plane)
$\varphi_{j,k}$	the angle between vectors, $\mathbf{p}_{j'}$ and $\mathbf{r}_{j'k'}$
$\Theta$	a molecule's polar tilt angle (relative to $\mathbf{z}$ )
$\psi$	an arbitrary angle
$\xi$	an arbitrary order parameter or reduced coordinate
$\chi_4^2 \chi_6^2$	2D $C_{60}$ square and hexagonal order parameters

## ABSTRACT

### MODELING THE SELF-ASSEMBLY OF FUNCTIONALIZED FULLERENES ON SOLID SURFACES USING MONTE CARLO SIMULATIONS

by

Gregory J Bubnis

University of New Hampshire, December, 2010

Since their discovery 25 years ago, carbon fullerenes have been widely studied for their unique physicochemical properties and for applications including organic electronics and photovoltaics. For these applications it is highly desirable for crystalline fullerene thin films to spontaneously self-assemble on surfaces. Accordingly, many studies have functionalized fullerenes with the aim of tailoring their intermolecular interactions and controlling interactions with the solid substrate.

The success of these rational design approaches hinges on the subtle interplay of intermolecular forces and molecule-substrate interactions. Molecular modeling is well-suited to studying these interactions by directly simulating self-assembly. In this work, we consider three different fullerene functionalization approaches and for each approach we carry out Monte Carlo simulations of the self-assembly process. In all cases, we use a “coarse-grained” molecular representation that preserves the dominant physical interactions between molecules and maximizes computational efficiency.

The first approach we consider is the traditional gold-thiolate SAM (self-assembled monolayer) strategy which tethers molecules to a gold substrate via covalent

sulfur-gold bonds. For this we study an asymmetric fullerene thiolate bridged by a phenyl group. Clusters of 40 molecules are simulated on the Au(111) substrate at different temperatures and surface coverage densities. Fullerenes and S atoms are found to compete for Au(111) surface sites, and this competition prevents self-assembly of highly ordered monolayers.

Next, we investigate self-assembled monolayers formed by fullerenes with hydrogen-bonding carboxylic acid substituents. We consider five molecules with different dimensions and symmetries. Monte Carlo cooling simulations are used to find the most stable solid structures of clusters adsorbed to Au(111). The results show cases where fullerene-Au(111) attraction, fullerene close-packing, and hydrogen-bonding interactions can cooperate to guide self-assembly or compete to hinder it.

Finally, we consider three bis-fullerene molecules, each with a different “bridging group” covalently joining two fullerenes. To effectively study the competing “standing-up” and “lying-down” morphologies, we use Monte Carlo simulations in conjunction with replica exchange and force field biasing methods. For clusters adsorbed to smooth model surfaces, we determine free energy landscapes and demonstrate their utility for rationalizing and predicting self-assembly.

# CHAPTER I

## INTRODUCTION

### **A. Motivation and Background**

Thin films of molecules, polymers, or nanoscale objects deposited on solids can substantially alter the physical properties of the substrate. Adsorbed thin films can also exhibit novel, non-bulk properties because the surface perturbs the adsorbed species' physical, electronic, and crystallographic environment. These two principles have stimulated the continued scientific interest in the design, fabrication, fundamental properties, and applications of molecular architectures on surfaces.

Several properties of surface adsorbed thin films have been studied recently. These include wetting [1,2], electrochemical activity [3], charge transport [4,5], and light harvesting [6]. Potential applications exist in the fields of tribology [7], chemical and biomolecular sensing [8,9], organic electronics [10], and photovoltaics [11].

Within this broad area, there is continued scientific interest in surface architectures incorporating carbon fullerenes. Discovered 25 years ago [12], C<sub>60</sub> fullerene is a near-spherical carbon allotrope that is intriguing both for its icosahedral symmetry and for its unique photochemical and electrical properties [11,13-16]. Fullerenes are of particular interest for potential applications in molecular electronics [13,14]. Established

methods in fullerene synthetic chemistry have also made it possible to study fullerenes substituted with nearly any organic functional group or supramolecular unit [17-19].

Fullerenes can play multiple roles as components in surface adsorbed thin films. First, they act as functional components in applications such as photovoltaics [11] and molecular electronics [13,14]. In addition, fullerenes strongly bind to many substrates (particularly coinage metals copper, gold and silver) with energies on the order of 20-60 kcal/mol [20-25]. While adsorbed, they can diffuse laterally [26] and can roll across surfaces [27-29]. This mobility is well suited to reversible self-assembly, whereas covalently attached molecules cannot reorganize in this manner. Finally, their size, shape and mutual attraction energy make them a useful construction unit in the design of ordered surface architectures. This dissertation focuses on the latter two points; however all three are intertwined to some extent.

One of the most promising applications for fullerenes is as a component in organic photovoltaics (OPVs). Although various OPVs are scientifically feasible, low charge mobility and poor morphological control hinder their performance and efficiency.

For a photovoltaic device to function, a photoexcited electron-hole pair needs to separate quickly (via the anode and cathode, respectively) in order to create electrical current and avoid recombination. Efficient charge separation requires the surrounding molecules to be spatially organized so that the charges can swiftly hop from one molecule to the next. However, charge mobility is hindered by amorphous ordering and by crystalline defects. Therefore OPV efficiency requires a suitable morphology and a highly crystalline material. The fullerene derivative PCBM [30] is a commonly used electron acceptor (anode) in OPVs, and a considerable body of literature is devoted to



efforts towards controlling its morphology (in blends with other materials) and crystallinity [31]. A conductive polymer or oligomer species (typically a polyphenylene or polythiophene derivative) transports the positive charge “hole” in the opposite direction [32-35].

Another factor governing OPV efficiency is the effective contact area of the anode and cathode. When anode and cathode materials interdigitate on a length scale of 10 nm, electron-hole pairs are most likely to separate and produce electrical current instead of recombining. In practice, phase separation can occur due to fullerene aggregation, thereby hindering OPV performance. Finding robust methods to create highly crystalline nanometer scale domains remains an open problem in the field [36,37].

In general, thin film properties depend both on the constituent molecules and on the spatial organization of these molecules. In light of this, systems in which molecules assemble spontaneously to form ordered patterns on surfaces are highly desirable. Self-assembled monolayers (SAMs) have been widely studied to advance the basic understanding of self-assembly phenomena [38-48].

In a recent review of self-assembly on surfaces, Barth [49] made a point to define self-assembly and to distinguish it from other pattern formation processes. In the author’s classification, self-assembly is a spontaneous process, driven by a free energy gradient, where functional units assemble into an ordered equilibrated structure. Self-assembly occurs in closed systems. However, self-organized growth and self-organization occur in open systems or systems subject to external stimuli. These conditions can foster ordered or partially ordered arrangements with dynamic or non-equilibrium character.

SAMs form spontaneously due to a combination of molecule-surface attraction (otherwise molecules would remain in solution or in their bulk solid) and intermolecular attractive forces. Both factors determine a SAM's morphology and crystallinity. The self-assembly of gold thiolate SAMs, which utilize the covalent bonding between S atoms and a gold substrate, is well understood. [38-48]. For instance, straight chain alkanethiols position their S atoms at closely spaced lattice sites and orient their hydrocarbon tails upwards, approximately normal to the surface. Due to weak van der Waals forces, the tails tilt uniformly and relax into an ordered crystalline structure [46]. The SAM morphology and properties can therefore be varied by choosing adsorbate species with different geometries and functionalities.

SAMs are commonly prepared by ultra high vacuum (UHV) deposition or by deposition from solution. Solution based methods are fairly straightforward and are amenable to established manufacturing processes [50]. Additionally, since the choice of solvent influences the assembly process and structural stability, [38,51] this choice can be exploited to generate different structures. However, from a fundamental perspective the presence of solvent-substrate and solvent-adsorbate interactions adds to the complexity of the underlying assembly phenomena. UHV deposition is comparatively resource intensive, but it permits self-assembly to proceed free from atmospheric and solvent effects.

Scanning tunneling microscopy (STM) is one of the most useful tools for probing SAM structures. Provided that the substrate is conductive, STM works both at liquid-solid interfaces and in UHV at the vacuum-solid interface, and this allows real time observation of assembly in both environments (solution or UHV). Owing to its

availability and versatility, STM has provided detailed structural (and electronic) information on many self-assembling systems and it has advanced the fundamental understanding of self-assembly [52-58].

From these insights, strategies for tailoring SAM morphology have also matured [59]. Some established strategies aim to harness specific interactions between molecules to drive pattern formation. For example, hydrogen bonding interactions can direct patterning due to their strength and specificity [49,52,58,60-67]. Another approach is to exploit hydrocarbon chain interdigitation [54,53,68-71]. When adsorbed on surfaces, fullerenes tend to pack hexagonally [21,22,25,72,73] due to their considerable interaction strength (6.4 kcal/mol in the gas phase) and their intrinsic symmetry. Therefore it remains a challenge to design fullerene SAMs that overcome close-packing tendencies and yield ordered, low density structures.

In addition to molecule-molecule interactions, molecule-substrate interactions can promote or hinder assembly. In many of the previously cited cases, lateral assembly occurs freely because the molecules are rigid, planar species that lie flat on the substrate. However for non-planar species, including most fullerene thiolate SAMs, strong adsorbate-substrate attraction can restrict molecules to non-preferred orientations which may hinder self-assembly of the intended structures [74]. This is an important consideration for fullerene SAMs because fullerenes bind strongly to metal surfaces (with binding energies on the order of 20-60 kcal/mol) [20,21,24,25,74,75].

Robust fullerene SAMs have been produced by modifying fullerenes with appropriate functional groups and choosing a favorable substrate. Many of these results

have been described in recent reviews [76-78]. A few notable examples are described here.

One approach to creating ordered, non-hexagonal fullerene motifs is to use bulky substituent groups which also adsorb to the surface. For example, Diaconescu and coworkers [54] studied a fullerene derivative bearing two long alkoxy chains adsorbed on Ag(111) in UHV conditions. They observed an ordered 2D lattice with fullerenes forming isolated dimer pairs. The authors infer that the chains adsorb parallel to the metal surface and splay to allow interdigitation. Nakanishi et al. [79] studied similar fullerenes having three long aliphatic chains instead of two. On the HOPG (highly ordered pyrolytic graphite) substrate, the molecules laid flat and formed 1D fullerene wires separated by the molecules' aliphatic chains.

Another method for controlling fullerene packing is to first assemble an ordered molecular scaffolding so that deposited fullerenes are attracted to specific sites. Scaffolding examples include porphyrins [80] and hydrogen bonded networks [60,81]. These multistep deposition approaches are promising for creating intricate architectures, but are not considered further here.

While experimental methods such as STM and Atomic Force Microscopy can characterize and image SAMs, they only offer partial insight into the physical phenomena driving the assembly process. Model calculations are ideally suited to complement experimental studies. Because modeling studies are effort-intensive, decisions need to be made about what variables to focus on.

When adlayer geometries are experimentally identified or when structures are predicted by chemical intuition, electronic structure calculations (typically density

functional theory (DFT)) can determine single point energies, frontier orbitals, and molecule-surface bonding characteristics. For instance Wang and Cheng [20] used DFT methods to determine the energy of an individual fullerene on the Au(111) and Ag(111) surfaces. Computational expense generally limits these calculations to selected geometries of one or a few adsorbate molecules. Systematic variations of molecular geometries and calculations for larger clusters of adsorbate molecules are not feasible with this approach.

To better understand self-assembly, we need both a kinetic and thermodynamic point of view. From disordered starting conditions, self-assembly is a dynamic process that can explore a long succession of structures, sometimes including metastable or kinetic traps, en route to equilibrium. The balance between thermal energy fluctuations and attractive forces guides these structural variations. Rigorous models of self-assembly should therefore start from randomized disordered configurations, just as real molecules do, and undergo the equivalent structural fluctuations as equilibrium is established. If such a simulation approach is sufficiently accurate and thorough, then it can predict the self-assembled thermodynamic ground state.

Clearly, this calls for models that can explore many molecular configurations at a reasonable computational cost. Inherently, these modeling approaches use the most computing time calculating the system's potential energy (internal energy) [82]. With this in mind, there are two crucial requirements for such models. First, the cost of calculating the potential energy for each configuration needs to be orders of magnitude cheaper than *ab initio* methods. Second, an efficient strategy is needed to sample molecular configurations starting from disordered initial conditions and leading to the self-

assembled thermodynamic ground state. These two requirements are discussed in some detail here.

Empirical force fields are the best choice for efficient energy calculations. Their validity rests on the Born-Oppenheimer approximation, which (paraphrased for these purposes) posits that a molecule's energy is unique for a given set of nuclear coordinates [83]. As a result of only considering atomic coordinates, energy calculations are much simpler and faster. However, to ensure their accuracy, empirical force fields must be parameterized using energies and geometries from accurate *ab initio* calculations. Alternatively, they may be adjusted to reproduce reference structures or known physical properties. Widely available molecular mechanics force fields (Amber, CHARMM, OPLS, etc.) are well-suited for studies of molecules in the gas or solution phases, but are not equipped to accurately describe molecule-substrate interactions. To maximize efficiency, these force fields describe atom-atom bonding and non-bonding interactions with simple functions: Chemical bonds are approximated with stretching, bending and dihedral "springs," while non-bonding electrostatic and dispersion interactions are calculated using Coulombic and Lennard-Jones potentials, respectively.

Modeling simulations that treat all atomic degrees of freedom, though less costly than *ab initio* methods, can still be computationally demanding. Therefore all-atom simulations of self-assembly starting from randomized configurations are not common. Instead, simulations of SAMs containing many molecules are often seeded with experimentally determined adlayer structures [84,85].

Lower resolution "coarse grained" force fields aim to further reduce computing cost by using fewer degrees of freedom (coordinates) to describe the system geometry.

Generally, coarse graining maps a molecule's atomic coordinates to a smaller set of interaction sites (also called pseudoatoms or united atoms) which are then used to compute the system energy [86,87]. The gain in computing speed depends on how many atoms are assigned to each interaction site.

An example relevant to the present study is Girifalco's  $C_{60}$ - $C_{60}$  potential [88], which assigns the 60 atoms of each fullerene to one interaction site, placed at its center of mass. The  $C_{60}$ - $C_{60}$  dispersion interaction is then computed using only the distance between the interaction sites. (The complete functional form is given in the Appendix (page 127)) An all-atom approach would require 360 Cartesian coordinates for the 120 carbon atoms involved, and the energy would be computed as a sum of  $60^2$  evaluations of the Lennard-Jones potential. The Girifalco approach constrains the fullerenes to be spherical, but it greatly reduces computational costs. For most purposes, the gain in efficiency greatly outweighs the loss of atomistic detail. Accordingly, this approach is used throughout this study.

In modeling studies of surface adsorbed molecules, all atom treatments of the substrate can be costly, especially when multiple layers are considered. One common remedy is to assume that the surface atomic lattice is rigid [89], thereby avoiding the repeated calculations of substrate atom-atom energies. This rigidity effectively averages over the surface vibrations which are fast compared to the phenomena of interest (molecular diffusion, adsorbate self-assembly, etc). A more simplified approach – similar in spirit to the implicit solvent models used in simulations of biomolecules [90] – is to use an effective potential for adsorbates that accounts for the presence of the surface [27,91-93]. Instead of computing energies between an adsorbate molecule and every

nearby atom of the substrate, the interaction is determined using the distance between the adsorbed atom (or interaction site) and the substrate plane. With this approach it is also possible to include corrugation terms that would better reproduce substrate atoms and their periodicity. In this study we elect to represent the Au(111) surface using an effective potential including corrugation terms [94].

Even with the efficiency gains afforded by a coarse grained force field, a systematic survey of molecular configurations would be an impractical way to simulate self-assembly. Therefore an efficient sampling strategy is the second important requirement for exploring configuration space and simulating self-assembly.

Beginning from a random, non-equilibrium configuration, the sampling method should tend towards equilibrium and it should locate the thermodynamic ground state. In addition, it should occupy metastable states with a probability given by relative free energies. That is, in the limit of a very long simulation different states should be sampled with a frequency proportional to their thermodynamic stability.

The two most established sampling methods for atomistic/coarse grained systems are the Metropolis Monte Carlo (MC) approach and molecular dynamics (MD) [82,83]. MD uses the gradient of the system's potential energy to guide the natural dynamics of the system with Newton's equations of motion. In the absence of external forces, Newton's Second Law gives

$$\mathbf{m} \frac{\partial^2 \mathbf{R}}{\partial t^2} = -\frac{\partial(U(\mathbf{R}))}{\partial \mathbf{R}}, \quad (\text{I.1})$$

where  $U(\mathbf{R})$  is the system's potential energy,  $t$  is time, vector  $\mathbf{R}$  contains Cartesian coordinates defining the system, and  $\mathbf{m}$  is a diagonal matrix of the particles' masses.



Noting that momentum  $\mathbf{p}$ , equals  $\mathbf{m} \frac{\partial \mathbf{R}}{\partial t}$ , the expression (I.1) can be recast as a pair of coupled first order differential equations:

$$\begin{aligned} \frac{\partial \mathbf{R}}{\partial t} &= \mathbf{m}^{-1} \mathbf{p} \\ \frac{\partial \mathbf{p}}{\partial t} &= - \frac{\partial(U(\mathbf{R}))}{\partial \mathbf{R}} \end{aligned} \tag{I.2}$$

These equations can then be integrated numerically to advance a trajectory through configuration space.

The MC approach samples configuration space by proposing random molecular displacements that are subject to a Boltzmann acceptance criterion. This Boltzmann criterion compares a proposed move's energetic cost with the thermal energy,  $k_B T$  at a chosen temperature  $T$  ( $k_B$  is the Boltzmann constant). Energy is not conserved, so the system can explore configurations that would be allowed by thermal fluctuations at the assigned temperature  $T$ . Both approaches can accumulate averages and statistical distributions of energetics and structure parameters. More importantly, both methods can efficiently sample the regions of configuration space relevant in self-assembly: namely the thermodynamic ground state, metastable states, and the barriers separating them.

## **B. The Present Work**

The following chapters present three self-contained studies of functionalized fullerene self-assembly on surfaces. Additional introductory context is provided in the chapter introductions. Brief descriptions are given here.

Chapter II describes MC simulations of the self-assembly of rigid fullerene thiolate molecules on the Au(111) substrate. This modeling reflects the established gold-

thiolate SAM strategy described earlier in the sense that the adsorbate-substrate linkage is intended to form through sulfur-gold bonding and the subsequent patterning should be dominated by intermolecular forces. The simulations complement the Tour group's experimental studies of fullerene thiolates on gold [74] which highlight the limitations of the gold-thiolate SAM strategy for fullerene bearing molecules. In our approach, each molecule is treated as three pseudoatoms: a  $C_{60}$  moiety, a phenyl spacer, and the thiol group. Multiple simulations are carried out to explore how different temperatures and different surface coverage densities influence pattern formation and self-assembly.

Chapter III describes MC simulations of a family of fullerenes with linear polyphenylene substituents and carboxylic acid groups. Their self-assembly is investigated on the Au(111) substrate. From the results of Chapter II, it was evident that fullerenes competed with S atoms for surface adsorption sites to the point that patterning was hindered. Accordingly, the molecules in this chapter do not contain thiol moieties and bind to the surface primarily through the strong  $C_{60}$ -Au(111) attraction. The different substituent groups are chosen to explore how simple changes in a molecule's shape and the location of hydrogen bonding functionality (the carboxyl groups) yield different self-assembled structures. These simulations are initialized randomly at high temperature and are then slowly cooled in 50K steps. Thermal averages of energetic and structural parameters are collected to elucidate temperature dependent phase behavior. The slow cooling aims to ensure equilibration so that the low temperature structures are the true thermodynamic ground states.

Chapter IV describes simulations of a family of bis-fullerene molecules with different bridging groups. Due to poor sampling of structurally distinct low energy states,

the MC simulation protocols were modified with a replica exchange algorithm to improve low temperature sampling. To address the experimental uncertainties in the fullerene-gold interaction strength, we carried out simulations with different binding energies. We perform extensive simulations and collect statistics for the energetics and structural characteristics of these clusters. Lastly, we employ histogram reweighting methods to construct free energy landscapes and interpret their features in the context of spontaneous self-assembly.

## CHAPTER II

### **SELF-ASSEMBLY AND STRUCTURAL BEHAVIOR OF A MODEL RIGID C<sub>60</sub>-TERMINATED THIOLATE ON Au(111)**

#### **A. Introduction**

Self-assembled monolayers (SAMs) have been the subject of considerable recent research activity. [38-48] (For reviews, see references [38-40].) SAMs are ordered molecular assemblies formed spontaneously by certain adsorbate molecules on a solid substrate. In particular, thiolate SAMs, which utilize the covalent bonding between S atoms and a gold substrate have been extensively investigated in recent years. One striking feature of SAMs is the sensitivity of their structure to details of intermolecular interactions between the adsorbate molecules [38-40,42,43]. This suggests that surface patterning can be tailored by the judicious choice of adsorbate properties.

Since their discovery in 1985, fullerenes [12] have been recognized as a rich potential area for research. Thin films of fullerene derivatives have a wide range of photochemical and electrical properties [11,13-16]. Among many other technological possibilities, they have considerable potential applications in molecular electronics [13,14].

Therefore, the construction of SAMs with molecules containing C<sub>60</sub> moieties has been a topic of some interest [11,13-16,47,48,74]. The experimental strategies for producing such fullerene containing-SAMs (or FSAMs) have been reviewed [74]. Several groups have had success in first patterning the surface using a traditional SAM, then subsequently performing additional chemistry to attach the fullerenes [11,16]. However, it would be particularly useful to have a technique in which the molecule containing both the fullerene and S-containing moieties could self assemble in a single step. This is sometimes referred to [74] as the “direct” strategy for producing FSAMs.

There have been several successful attempts to do this. (For comprehensive reviews, see references [15] and [74]). To the best of our knowledge, the first was by the Mirkin group in 1994 [48]. One report of “relatively robust” formation of C<sub>60</sub>-terminated SAMs from solution has been given by Shon et al., using an unsymmetrical disulfide molecule to tether to the substrate [47]. They obtained close to monolayer coverage on the surface, but saw little evidence of ordering in the adlayer. The field is clearly less well developed than is that for traditional SAMs, and predictive models are essentially non-existent. In fact, several promising-looking candidate species have not proven successful in forming FSAMs. Shirai et al. [74] have reviewed the literature, and point out some of the difficulties. The most striking is the fact that C<sub>60</sub> interacts strongly with the Au(111) surface. In fact, the C<sub>60</sub>-Au bond strength has been reported as being in the range 25-60 kcal/mol. This clearly is comparable with the strength of the S-Au bond, (which is known to be about 40 kcal/mol) Therefore, under many conditions, the C<sub>60</sub> and the S may compete for chemisorption sites on the gold surface. Shirai et al. [74] point out several “anomalous” results from their own work, and propose that structures of FSAM may be

encountered other than those with solely the S headgroup chemisorbed to the gold substrate. In particular, they show some evidence that multilayer formation is a possibility.

To our knowledge, there have been no computational studies carried out on FSAMs. Since the area is rich in potential applications, it seems worthwhile to carry out preliminary modeling studies. Since there are several competing interactions, the structures of FSAMs may not be easily predicted by chemical intuition alone. This further justifies the global exploration of the energy landscape.

Many traditional SAMs described in the literature have a relatively flexible “backbone” or “spacer” between the thiolate headgroup and the endgroup – typically alkane chains. In FSAMs with flexible spacers, both the S atom and the terminal group can both be accommodated at chemisorption sites with little internal strain. Shirai et al. [74] have proposed using more rigid spacer groups for avoiding this in designing FSAMs. The spacer groups proposed in their work (which they refer to as “alligator clips”) utilize phenylene ethynylene. In this study, we model the behavior of a molecule with a somewhat simpler phenyl spacer. Synthetic pathways to forming such fullerene derivatives have been reviewed by Miller and coworkers [17].

In order to model the self assembly of molecules on a substrate, a potential energy function must be constructed. A fully atomistic treatment would be prohibitively resource intensive. We have therefore treated certain sites on each molecule as united-atom groups or “pseudoatoms” [42,43] (as is frequently done in simulations of liquid crystals [95]) and used a pseudoatom-pseudoatom potential energy function. Monte Carlo calculations by Grunze and coworkers [42,43] have shown that coarse grained modeling of the

potential energy can produce realistic results for SAMs, and can certainly reproduce qualitative trends. Fully treating internal degrees of freedom of the molecule would require considerable additional computer resources, with little guarantee of further insight. Accordingly the thiolates are treated as rigid species. We feel our choice of a rigid spacer group justifies this approximation. The calculation is further simplified by assuming the gold substrate is rigid.

By eliminating internal degrees of freedom, we can focus on the role played by the intermolecular potential in the system's behavior. Our intention is to look at the role of the intermolecular forces in governing the system, and to investigate the influence of the interactions on the possibility of FSAM formation. Considerable insight into the role played by the intermolecular forces in self-assembly can be obtained by investigating the phase behavior of the adsorbate in the temperature-surface coverage space [40,61]. Typically, [40] SAMs (such as decanethiol) are found in the "lying down" phase at low coverage where molecule-surface interactions dominate, but prefer the "standing up" phase at higher coverage, when the forces between the molecules become competitive with the molecule—surface interaction. Rigid SAMs have been shown to form patterned layers, particularly when the intermolecular interaction is strong [96,97]. Varying the temperature of the adsorbed layer allows the system to access different regions of the potential energy surface [89]. Qualitative changes in order parameters are used signal the existence of phase boundaries.

To investigate the behavior of the system, we use canonical (fixed temperature) Monte Carlo calculations at a variety of different temperatures and at varying adsorbate

surface coverage. To make the calculations tractable, we use periodic boundary conditions in the plane of the gold surface.

Our model potentials are discussed in Section C, along with other details of the calculation. Results and Discussion are in Section D. Conclusions are in Section E.

## **B. Calculations**

### **1. Model Rigid C<sub>60</sub>-terminated Thiolate**

As discussed in the Introduction, we have made several simplifying assumptions to render the modeling computationally feasible. The molecule has a thiolate headgroup (S), with a phenyl (Ph) tether, and a C<sub>60</sub> endgroup. We reduce this to three pseudoatoms, in a C<sub>∞v</sub> geometry. The separations are 6.75 Å between the C<sub>60</sub> and the Ph; 5.25 Å between the Ph and the S. The molecule is assumed to remain rigid. A cartoon of the molecule used in the modeling study is shown in Figure II-1(b).

### **2. Potential Energy Function**

The potential energy function is described in detail in the Appendix (page 127). The molecule-molecule interaction is a pairwise sum over all pseudoatom-pseudoatom sites. Each pseudoatom also interacts with the (assumed rigid) gold surface through a z-dependent potential modulated by a periodic (x,y) term. The z-dependent part of the potential for the C<sub>60</sub>-Au and S-Au interaction is shown in Figure II-1(a). Details of each part of the potential are described in more detail below.

#### **(a) Sulfur-Gold**

The S-Au interaction is a fit to the S-Au atom-atom potential of Mahaffy et al. [98]. Their S-Au atom potentials have been recast in a form  $U(z)$  (where we have used a Morse function for  $U(z)$ ) multiplied by a Fourier term which includes surface periodicity



in the surface (x,y) plane [94]. The advantage of this form is that it allows us to vary the z dependence of the interaction in a flexible manner (although that is not done here, variations are central focus of Chapter IV.). The S atom prefers to sit at the threefold hollow site of the Au(111) surface with a binding energy of 45 kcal/mol. The barrier to migration is about 3 kcal/mol. The potential used here is similar to one used in a recent MD study [46]. Recent DFT calculations have been carried out for alkanethiolates [99] and benzene dithiolate on gold [100]. The DFT calculations give slightly shallower well depths than the value we used, ranging from 38 to 33 kcal/mol depending on the molecule and the surface site.

(b) Fullerene-Gold

There are several experimental [21-23,26,101,102] and theoretical [20,103] results available for fullerene molecules and fullerene films on Au(111). Experimentally, there seems to be a slight preference for the fullerenes to occupy two-fold bridge sites rather than three-fold sites (although the interpretation of the experimental evidence does not point unambiguously to this conclusion). DFT calculations show a preference for an isolated C<sub>60</sub> molecule to occupy three-fold surface sites.

Experimental estimates for the binding energy of C<sub>60</sub> on Au(111) lie in the range of 25-60 kcal/mol [21-23]. DFT calculations of C<sub>60</sub> on Au(111) give a binding energy of 30 kcal/mol [20]. The computational value is on the low end of the experimental estimates for this quantity. There is also limited information on the frequency of vibration of a fullerene on a gold surface [101]. This information was used to give a potential with the same functional form as the S—Au potential.

Using our model potential, the barrier for site-to-site diffusion on the surface for an isolated  $C_{60}$  is about 3 kcal/mol. The  $C_{60}$  is preferentially attracted to the three-fold sites.

(c) Fullerene-Fullerene Potential

The fullerene-fullerene potential is given by the Girifalco potential [88]. This assumes the molecule is spherical and isotropic. The fullerene-fullerene dimer energy in this model is 6.4 kcal/mol. This potential has been shown to give realistic behavior for fullerenes in gas phase clusters and in condensed phases.

(d) Other Interactions

The Ph-Ph interaction is given by a united-atom Lennard-Jones (LJ) (12,6) potential used previously in liquid crystal simulations [95]. The S—S potential allows only for dispersion interactions; no S—S bond formation is considered. The energy is the same as that of Klein and coworkers [44].

The “mixed” site-site interactions are obtained using the Lorentz-Bertholet mixing rules [104] for parameters (the well depth for the mixed interaction is the arithmetic mean of the well depths for the individual components; the mixed vdW radius is given by geometric mean of the radii of the individual components). The parameters for the anisotropic z-dependent Ph—Au interaction were chosen to reproduce a reasonable orientation-averaged van der Waals radius.

### **3. Monte Carlo Calculations**

The temperature is maintained by using the Metropolis Monte Carlo approach [82,104,105], in which random updates in the configuration space are accepted or rejected using a Boltzmann-like weighting. Specifically, the probability of accepting an

update from configuration  $i$  to  $i'$  is given by a ratio of their individual probabilities in the canonical ensemble,

$$p(i \rightarrow i') = \min \left[ 1, \frac{p(i')}{p(i)} \right] = \min \left[ 1, \frac{\exp[-U_{i'}/k_B T]/Z(T)}{\exp[-U_i/k_B T]/Z(T)} \right], \quad (\text{II.1})$$

where  $U_i$  and  $U_{i'}$  are the associated potential energies,  $k_B$  is the Boltzmann constant and  $Z(T)$  is the partition function. Cancelling terms, (II.1) simplifies to

$$p(i \rightarrow i') = \min[1, \exp[-(U_{i'} - U_i)/k_B T]]. \quad (\text{II.2})$$

The probability (II.2) is unity for downhill moves (where the system energy decreases). However, uphill move probabilities are determined by comparing the energy change,  $(U_{i'} - U_i)$ , to the typical thermal fluctuations,  $k_B T$ .

Translational and rotational trial moves of a single molecule are equally probable. The three Cartesian components of a translational shift and the angle of a rotation about a random axis are chosen from flat distributions. Molecules are initially assigned random positions and orientations within the simulation region. The maximum trial shift and rotation magnitude are adjusted to give an approximately 50% acceptance ratio during an initial equilibration period of  $10^5$  cycles but then remain fixed during the  $10^6$  data acquisition cycles. Each cycle consists of  $N$  trial moves, where  $N$  is the number of molecules.

We have carried out the calculations using periodic boundary conditions. The primary region is a rectangle with side lengths set to be as close as possible while still matching the substrate periodicity. For all simulations, the number of molecules,  $N = 40$ , is fixed. Therefore to set the desired surface coverage  $\theta$ , the area of the primary region is

adjusted. Additionally, at a height of 50Å above the surface a harmonic repulsion is employed to ensure that molecules do not “evaporate”.

The phase behavior of the adlayer is monitored by recording the ensemble average of the tilt angle (see Figure II-1) as a function of surface coverage,  $\theta$ , for temperatures between 500 and 1500 K. The potential energy landscape is sufficiently rugged that for temperatures significantly less than 500 K, the adsorbed layers are essentially frozen. In addition, at each coverage an attempt was made to find feasible candidates for the global energy minimum structure using simulated annealing [106].

### **C. Results and Discussion**

The geometry for a single rigid C<sub>60</sub>-terminated thiolate molecule chemisorbed on Au(111) is sketched in Figure II-1(b). As can be seen, both the S atom and the C<sub>60</sub> moiety are bonded to the surface in a “lying down” configuration. To quantify this orientation, the tilt angle,  $\theta$ , is defined between the substrate normal and the molecule’s symmetry axis. For the potential used here, the equilibrium value of this angle is about 72 degrees. The S atom preferentially sits over a three-fold hollow site, as does the C<sub>60</sub>.

Test calculations (described in Chapter III) using the potential proposed here [94] reproduce the  $(2\sqrt{3} \times 2\sqrt{3})R30^\circ$  adlayer predominantly observed for “neat” fullerenes on Au(111) under most experimental conditions [21,22]. The calculations also reproduce the experimental values for the mean fullerene-fullerene distance on gold, which is 9.98 Å (this corresponds to a surface coverage of  $\theta = 11.59$  molecules/ $10^3 \text{Å}^2$ ). This length is somewhat compressed from the 10.06 Å separation which the Girifalco potential gives as the dimer separation in the gas phase. The number of C<sub>60</sub> nearest-neighbor (NN) contacts per molecule in this geometry is NN=6.

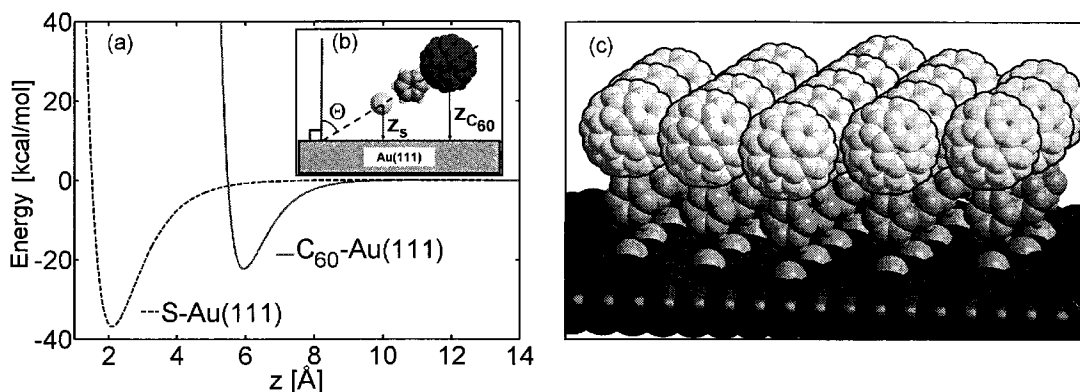


Figure II-1. (a) The interaction potential of the S atom and the C<sub>60</sub> terminal group with the Au(111) substrate. (b) A cartoon of the model rigid C<sub>60</sub>-terminated thiolate molecule used in this study. The tilt angle  $\Theta$  is shown defined relative to the surface normal. (c) A cartoon of the molecule forming a ‘normal,’ upright SAM creating a close-packed fullerene layer. The Au substrate atoms are also shown.

Shown in Figure II-1(c) is a schematic of the “normal” SAM geometry that would be expected if the fullerene thiolate were able to utilize optimal packing of the C<sub>60</sub> moiety in the close-packed single fullerene adlayer. The tilt angle for such a geometry would be zero. Note that this spacing would allow the S atoms to chemisorb at the favored threefold sites.

In Figure II-2, we plot the ensemble average of several of the system variables as a function of surface coverage for two different temperatures. We find that surface density controls the structure of the adlayers much more strongly than does temperature.

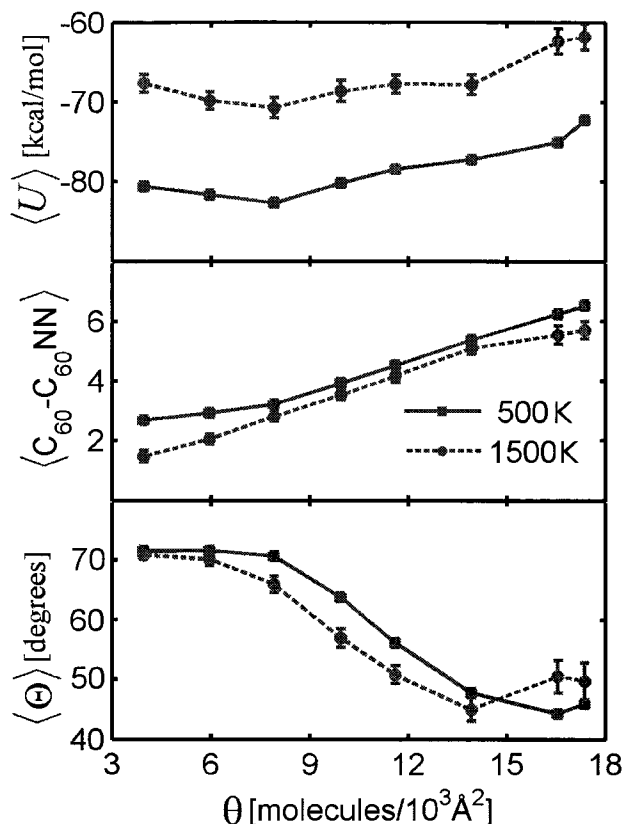


Figure II-2. Ensemble averages as a function of surface coverage for  $T = 500$  and  $1500\text{K}$ . Lower panel, tilt angle; middle panel,  $C_{60}$ - $C_{60}$  nearest-neighbor (NN) contacts (defined as contacts closer than  $12\text{\AA}$ ); upper panel, total potential energy (kcal/mol) per adsorbate molecule. Error bars are one standard deviation. We note that  $\Theta$  distributions are bimodal due to lying-down ( $\Theta \sim 70^\circ$ ) and standing-up ( $\Theta \sim 0^\circ$ ) molecules. The average tilt angle,  $\langle \Theta \rangle$  accounts for the relative proportions of the two orientations and its distribution is unimodal. Thus, the standard deviation of  $\langle \Theta \rangle$  is reported instead of the standard deviation of  $\Theta$ .

In the bottom panel we show the average tilt angle  $\langle \Theta \rangle$ ; in the middle, the mean value of NN contacts per molecule; in the upper panel, the mean potential energy per molecule. (Note that all energies will be given in unites of kcal/mol per adsorbate molecule hereafter.) From a qualitative examination of these plots, we distinguish three different regions of behavior with  $\theta$ , which we label I ( $1 \leq \theta \leq 8$ ), II ( $8 < \theta \leq 16$ ), and III ( $\theta > 16$ ). The boundaries between the regions are most clearly distinguishable at the lower

temperature, 500K. We note that there is no sign of a qualitative change in behavior at the  $\theta$  value ( $\theta = 11-12$  molecules/ $10^3 \text{ \AA}^2$ ) that would correspond to the close-packed single adlayer shown in Figure II-1(c).

Region I has the following characteristics. The mean tilt angle  $\langle \Theta \rangle$  is constant at 72 degrees. The mean potential energy is relatively flat with a value of about -80 kcal/mol. The number of intermolecular  $C_{60}$  NN interactions is low (and at 500K is essentially constant at a value of about 3.)

Region II is characterized by a steady decrease in the mean tilt angle with  $\theta$ , an increase in the number of  $C_{60}$  interactions, and a positive slope of  $d\langle U \rangle/d\theta$ .

Region III shows a reversal in the trend of the tilt angle, which now increases with  $\theta$ . The number of  $C_{60}$  interactions is constant, and the potential energy per molecule increases somewhat more steeply than in region II.

In order to determine the adsorbate structure in each of these regions, we have carried out a series of simulated annealing runs at each surface coverage to search for low-energy minima [106]. The potential energy landscape is extremely rugged with a large number of competing minima. Accordingly, we make no claim that the structures found are the global minimum energy geometries. Figure II-3, Figure II-4, and Figure II-5 show representative low potential energy structures from regions I, II, and III respectively.

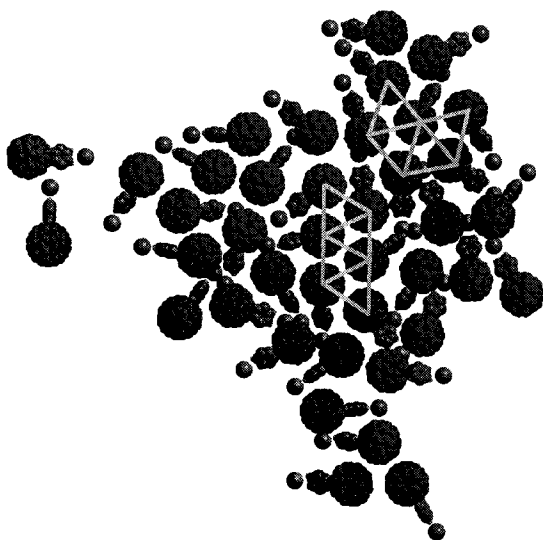


Figure II-3. Typical annealed geometry of the adlayer for low coverage (region I). Here  $\theta = 4.09$  molecules/ $10^3 \text{ \AA}^2$ . The solid lines here show local close-packed ordering in the fullerene moieties. For clarity, the Au(111) substrate is not shown.

In the region I structure shown in Figure II-3, the molecules are clearly lying flat on the surface, chemisorbed at both the S and the  $C_{60}$  molecular site. The total energy due to chemisorption at both S and  $C_{60}$  is -65 kcal/mol. The remaining energy (about -15 kcal/mol in region I) is derived from the fullerene-fullerene attraction. The mean number of  $C_{60}$  NN interactions in region I is lower than the NN=6 of a close-packed neat fullerene layer. This is due to steric frustration of adlayer close packing caused by the Ph-S part of the molecule.

We turn our attention next to the intermediate region II. In this region,  $\langle \theta \rangle$  decreases from the “lying flat” value of 72 degrees. In Figure II-4, we show a typical annealed structure. From visual examination, we note there are now two distinct values of the tilt angle; those with  $\theta = 72$  degrees; and those upright molecules with a lower value (about 30 degrees). Those with a lower value of  $\theta$  are chemically bonded to the surface solely at the S atom.



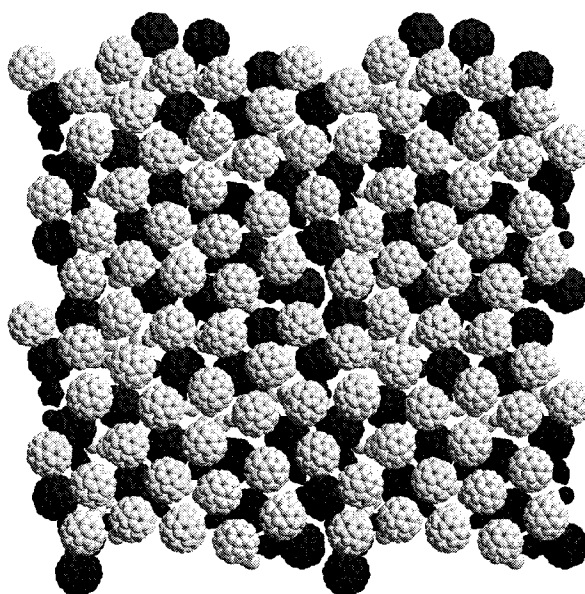


Figure II-4. Typical annealed geometry of the adlayer for intermediate coverage (region II). Here  $\theta = 15.46$  molecules/ $10^3 \text{ \AA}^2$ . Four adjacent primary cells are shown. Lying-down molecules are dark blue; standing-up molecules are white. For clarity, the Au(111) substrate is not shown.

A study by Paci et al. [89] considered the interplay between atom-surface interactions and atom-atom interactions. They note that single adlayers will dominate in the limit that atom-surface attraction is much stronger than atom-atom attraction. Our system is more complicated, in that both chemical and physical interactions, as well as molecular anisotropy, play a role. At low coverage (region I), we find the molecule-surface interactions can be fully satisfied. The lying-down molecules gain 65 kcal/mol from binding to the surface. However, they have relatively poor intermolecular attraction. The S-only chemisorbed molecules (observed in regions II and III) get -40 kcal/mol from molecule-substrate attraction; in addition, they can gain stability from intermolecular attractions. This is evidenced by the increase in NN interactions in region II. However, as we have noted before, with the combination of potential parameters used here, we do not

obtain a complete conversion to an S-only type of surface bonding (as would be required for a “normal” FSAM). The maximum coverage possible for chemisorbed species is about  $\theta = 16$  molecules/ $10^3 \text{ \AA}^2$ . At this coverage, all the chemisorption sites are occupied.

Region III shows that at greater coverage than this, additional thiolate molecules can no longer chemisorb to the Au, and are physisorbed on the chemisorbed layer, with the incremental potential energy coming chiefly from the  $C_{60}$  NN attractions. The tilt angle for the physisorbed species is no longer the appropriate term; the angles between the molecular axis and the surface normal are typically greater than 90 degrees for the physisorbed species. The ensemble average of these angles thus increases again in region III.

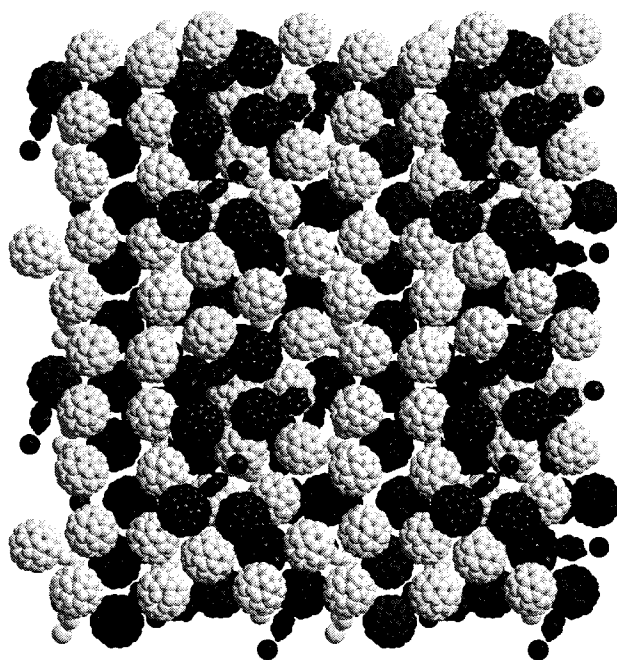


Figure II-5. Typical annealed geometry of the adlayer for high coverage (region III). Here  $\theta = 17.39$  molecules/ $10^3 \text{ \AA}^2$ . Four adjacent primary cells are shown. Lying-down molecules are dark blue; standing-up molecules are white; physisorbed molecules are green. For clarity, the Au(111) substrate is not shown.

As discussed by Shirai et al. [74], the interaction of the  $C_{60}$  with the substrate is critical in determining the geometry of the self-assembled layers. The nature of the  $C_{60}$ -Au bonding is still not well understood, and further calculations are probably in order. With the parameters adopted here, it appears unlikely that an ordered monolayer will be easily formed using a simple thiolate headgroup. Other ways of tethering the fullerenes to the substrate have been proposed [74], and we are investigating some of these possibilities.

#### **D. Conclusions**

We have carried out a simulation of an ensemble of model rigid fullerene-containing thiolate molecules on Au(111). Both the  $C_{60}$  and the S are capable of bonding to the substrate, and the fullerene-fullerene van der Waals interaction is explicitly included. At low surface coverage, the molecules form a lying-down adlayer with all the chemisorption bonds being used; that is both the S and  $C_{60}$  are strongly bonded. At higher coverage, there is competition for the substrate chemisorption sites. The molecules appear in both a lying-down form and a standing-up form (which is chemisorbed solely by the thiolate bond.) Molecules pack to optimize local  $C_{60}$ - $C_{60}$  interactions. However, for the parameters used here, there is no sign of the layer forming a “normal” FSAM monolayer with all molecules standing up. At both low and high coverage, there is little evidence of ordered pattern formation, although structural trends are detected. It is expected that the structure of the adsorbate layers will depend quite sensitively on the details of the potential energy.

## CHAPTER III

### **SELF-ASSEMBLY OF VARIOUS HYDROGEN-BONDING FULLERENE DERIVATIVES ON Au(111)**

#### **A. Introduction**

Fullerenes have been widely investigated since their discovery in 1985 [12]. Their unusual properties give them great potential for use in electronic devices. In light of this, there has been considerable interest in investigating the possibility of patterning thin films of fullerenes or fullerene derivatives on various substrates [11,74]. Most work in this area [48] has used the traditional self-assembled monolayer (SAM) strategy [39] for chemisorption using thiolate linkages. However, this approach has not been particularly fruitful for fullerenes. The reason for this is that fullerenes can bind strongly to metal surfaces, and compete with the S functionality for reactive sites [74,107].

With the availability of STM as a surface probe, a growing body of information on thin films exists. There is considerable experimental [21-23,102,26,108,56,109,110] and theoretical [103,111,112] evidence showing neat fullerenes adsorb strongly on metals, forming close-packed monolayers. An alternative approach to the production of patterned fullerene thin films then, is to utilize this ability of fullerenes to adsorb directly onto metal substrates.

This approach has been used by several groups recently, who have investigated the behavior – in particular the possibility of spontaneous pattern formation – of various fullerene derivatives on a variety of (mostly metal) substrates. Fullerenes are particularly

good species for investigation by STM, which was used in all the studies discussed here. [54,62,72,79,111,113,114] The field has been relatively recently reviewed. [76] We briefly summarize the most relevant findings here.

Matsumoto et al. [72] investigated  $C_{60}$  malonic acid on Au(111). They observed a close-packed fullerene monolayer. However, the close-packed fullerene adlayer geometry has a structure significantly different than that of the bare fullerene. They ascribe this to the hydrogen bonding. Further, they note additional orientational ordering imposed by the two hydrogen-bonding carboxylic acid groups which are bonded to an  $sp^3$  carbon, and are therefore tetrahedrally disposed.

Ecija et al. [113] looked at monolayers of phenyl- $C_{61}$ -butyric acid methyl ester (PCBM) on Au(111). This molecule has an ester-terminated side chain attached to the fullerene. The authors found two competing morphologies. At low coverage, the fullerenes were present predominantly as monomers, and their pattern was templated by the underlying metal surface reconstruction. At higher coverages, they observed rows of hydrogen-bonded PCBM dimers and tetramers.

Diaconescu et al. [54] looked at a fullerene derivative with two long aliphatic chains adsorbed on Ag(111). They found the molecules to self-assemble into rows of dimers. The authors infer that the chains adsorb parallel to the metal surface, and are interdigitated.

Nakanishi et al. [79] studied fullerenes similar to those of Diaconescu et al. but having three long aliphatic chains instead of two. On the HOPG substrate, the molecules laid flat and formed 1D fullerene wires separated by the molecules' aliphatic chains.

Chen et al. [114] examined four metallofullerenes with functional groups of varying size and different intermolecular interaction types on Au(111). They found that the smaller functional groups caused the molecules to form only the  $(2\sqrt{3} \times 2\sqrt{3})R30^\circ$  adlayer structure and not the (38 x 38) structure also reported for bare fullerenes on the same substrate [21]. However, the close-packed adlayer structure they observed also differed from that seen for hydrogen bonded C<sub>60</sub> malonic acid [72]. Chen et al. also found that bulkier functional groups inhibited close-packing. Thus, although substituents are generally difficult to image using STM (as compared to fullerenes), it seems clear that the substituents' influence on adlayer patterning can be inferred from observation of the C<sub>60</sub> close-packing and the type of fullerene-surface registry.

One particularly successful approach to the self-assembly of non-fullerene organic molecules on metal substrates has been to use strong intermolecular interactions (such as hydrogen bonding) to drive the formation of patterned physisorbed adlayers. [52,49,77] Recently several groups have demonstrated experimentally that molecules containing hydrogen-bonding functional groups can self-assemble to form extended one-dimensional [58] or two-dimensional adsorbate arrays on Au(111). [52,60,62-64,84,115,116] A limited number of model studies have also explored the formation of these 2D hydrogen bonding networks. [61,84,117] Typically, the adsorbate molecules investigated in these studies have been planar species (such as aromatic rings or fused aromatic ring systems) which lie parallel to the plane of the substrate. The hydrogen-bonding functional groups lie on the outside of the molecule and are all consequently in the plane of the adsorbate layer. Typically, the aromatic molecules are not strongly preferentially bound to any particular surface site. Therefore, they are relatively free to

migrate on the surface, driven by the intermolecular interactions. In many cases, the self-assembly is governed by the ability of the adlayer to maximize the number of hydrogen bonding interactions. In particular, we note that extended “row” or “ribbon” structures have been observed using the dicarboxylic terephthalic acid [58].

There have been a limited number of modeling studies carried out on fullerene derivatives on metal surface. In virtually all cases, these were DFT studies of (typically) the monomer on the substrate [54] or small clusters such as the dimer or tetramer on the surface [111]. However, to the best of our knowledge, there have to date been no modeling studies of fullerenes on metal substrates which attempt to identify the optimal conditions for molecular self-assembly using unbiased initial conditions, or to report coverage and temperature effects. The interest in the field of fullerene thin films together with the possibility of using hydrogen-bonding functional groups to drive patterned self-assembly provide the motivation for the current study.

Accordingly, in this chapter we consider the self-assembly of a series of functionalized fullerenes on Au(111). The molecules generally contain two carboxyl groups as the hydrogen bonding groups. This is suggested by previous work on terephthalic acid, which has been one of the most studied molecules to date in this field. We generate a realistic potential energy function to account for all intermolecular interactions and molecule-metal interactions for this system. Using this, we predict the likelihood of patterned self-assembly through extensive sampling of configuration space. Since we have limited information on the interactions, there is some degree of model parameter variation in this study. In many ways, this study is reminiscent of one carried

out by Paci et al. [89] These authors looked at monolayer and multilayer formation of atoms on surfaces as the parameters are varied within a given functional form.

Modeling a system of this nature requires several simplifying assumptions. First, the molecules we investigate contain a large number of atoms. Therefore, a typical molecular mechanics calculation, accounting for all atom-atom interactions would be prohibitively time-consuming. Accordingly, we use a coarse-grained force field in which the fullerenes and other functional groups are treated as pseudoatoms. Fortunately, the fullerene-fullerene pseudoatom potential energy is well established [88]. Second, the interaction of fullerenes with the Au(111) surface is likely to be relatively strong, and to be strongly influenced by the surface binding site; however, the interaction even of bare fullerenes with Au(111) is not yet completely understood. Including the thermal motion of the metal atoms of the substrate would also be prohibitively resource intensive. We therefore elect to use a rigid gold surface. Third, modeling all internal degrees of freedom of the molecule would require considerable additional computer resources, with little guarantee of further insight. Therefore, we constrain each molecule to be rigid and justify this approximation by only considering molecules that are highly conjugated and conformationally rigid to begin with.

The approximations listed above are similar to constraints used by Akimov and coworkers in a recent molecular dynamics study [27] of fullerene “nanocars” on Au(111). One such approximation made by these authors was to partition each molecule into connected rigid fragments akin to the “chassis” and (fullerene) “wheels.” This is justified by the inherent rigidity of these fused polycyclic components. Importantly, these constraints preserved the most important internal molecular motion – rotation of the



fullerene wheels – while eliminating unnecessary vibrational degrees of freedom. The authors also used a rigid Au(111) surface represented as an effective potential with an atomic corrugation term.

With the set of simplifying assumptions listed above, we set out to study the features of the potential energy landscape which contribute to the formation and structure of adlayers of fullerenes and fullerene derivatives on Au(111). We are most interested in the structures formed at experimental temperatures (typically 300-400K). One approach to determining these structures in an unbiased manner would be to carry out “simulated annealing” [106] starting a Monte Carlo simulation at high temperature, and then systematically reducing the temperature until the putative ground state is obtained. However, this procedure discards information obtained at high and intermediate temperatures which could provide insight into the role played by features of the potential energy in adlayer formation. Therefore, we allow the system to fully equilibrate at all temperatures, and monitor the properties at each temperature, paying particular attention to phase transitions. Since we have neglected a large number of degrees of freedom in our simulation, we point out that temperatures at which we observe phase transitions will not correspond closely to those that would be obtained in experiment on comparable systems.

The remainder of this chapter is organized as follows. In Section B, we discuss our choice of candidate functionalized fullerenes, and outline a scheme for their synthesis. In Section C, we outline the model potential energy functions we use to simulate the intermolecular interactions between molecules, and with the substrate. In Section D, we describe our Monte Carlo search strategy for identifying the most stable adlayer. Results are presented and discussed in Section E, with conclusions in Section F.

## B. Molecules studied

A coarse-grained representation is used to describe a family of fullerene derivatives with carboxylic acid terminated phenyl, biphenyl, and (linear) polyphenylene substituents. Molecules are represented as rigid assemblies of three united atom (UA) groups – the fullerene ( $C_{60}$ ), phenyl linker (Ph), and carboxylic acid (CA). Figure III-1 shows the molecules in cartoon representations where  $C_{60}$  and Ph groups are drawn as blue and grey spheres, respectively, scaled to their van der Waals radii. CA groups are drawn as carbon and oxygen atoms but the acidic hydrogens are not shown. Above each molecule, the chemical structure of its substituent “arm” is shown.

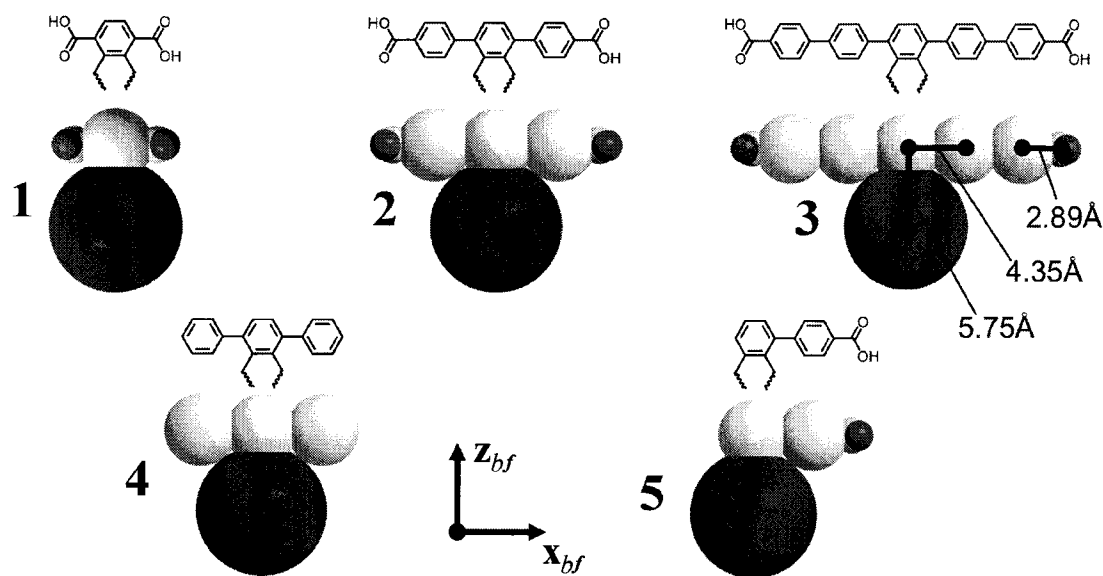


Figure III-1. Cartoon chemical structures of the derivatized fullerenes studied here. Molecules 1, 2, and 3 have  $C_{2v}$  symmetry and their carboxyl groups are separated by 1, 3, and 5 phenyl moieties, respectively. Molecule 4 is equivalent to 2, but with both carboxyl groups removed. Molecule 5 has reduced symmetry and only one carboxyl group. The relevant molecular dimensions are shown on 3. The local coordinate system for the molecules is also included.

Although the specific molecules we study here have not yet, to our knowledge, been created they are based on a well-established synthesis [18] in which a substituted

1,2-bis(bromomethyl)benzene is attached to  $C_{60}$  by a [4+2] cycloaddition. As a result of this addition, two methylene carbons bridge the Ph and  $C_{60}$  as is illustrated in Figure III-1 where wavy lines denote the  $C_{60}$ -CH<sub>2</sub> bonds. In this work we approximate this linkage as being rigid. The three distances between the UA groups in all of the molecular geometries are: CA-Ph, 2.89Å; Ph-Ph, 4.35Å; and Ph- $C_{60}$ , 5.75Å. The  $C_{60}$  is used as the origin for each molecule's body-fixed coordinate system (indicated with *bf* subscripts). The substituent arms lie in the  $x_{bf}$ - $z_{bf}$  plane and are parallel to the  $x_{bf}$  axis.

These specific molecules are chosen to systematically explore how their differences in geometry, symmetry, and hydrogen bonding functionality affect adlayer structures. The substituent of **1** is terephthalic acid, a molecule for which the structural behavior on surfaces is well understood. In many experiments, terephthalic acid forms parallel 1D rows driven by intermolecular hydrogen bonding [58]. Molecules **2** and **3** have the same symmetry as **1**, but with CAs further separated by additional Ph groups. To explore how dispersion interactions alone can dictate pattern formation, no hydrogen bonding groups are present on **4**. Finally, due to its asymmetry, it is anticipated that **5** will not be able to form connected 1D rows. However, the CA groups are expected to be able to dimerize.

### **C. Potential Energy Functions**

Pairwise-additive potential functions are defined for all binary UA combinations as well as between UAs and the rigid Au(111) surface. Where possible, such as for UA  $C_{60}$ - $C_{60}$  and Ph-Ph interactions, existing potential functions are used. In most other cases, we use simple functional forms that reproduce DFT or force field data. The key aspects

of this force field – the functional forms, distances, and interaction energies – are summarized in Table III-I. What follows is a thorough description of the functions used.

	C <sub>60</sub>	Ph	CA
C <sub>60</sub>	(G, 10.06, 6.4)		
Ph	(LJ, 8.2, 2.19)	(LJ, 6.4, 0.75)	
CA	(LJ, 6.9, 1.0)	(LJ, 5.1, 1.0)	(M+A, 3.79, 17.33)
Au(111)	(M+C, 5.7, 29.2)	(LJ, 4.6, 0.5)	SRR

Table III-I. A summary of the potential energy functions and parameters used for UA-UA and UA-substrate interactions. The notation used lists, in order from first to last, the functional form, the preferred separation in Å, and the minimum energy in kcal/mol. Functional form abbreviations are as follows: G, Girifalco’s pseudoatomic potential (reference [39]); LJ, Lennard-Jones potential; M+A, Morse potential with anisotropy; M+C, Morse potential with corrugation; SRR, Short range repulsion.

### 1. UA-UA interactions

As was mentioned earlier, the molecules we consider are constructed from C<sub>60</sub>, Ph, and CA groups. First, we describe the homogeneous interactions between UA groups. Girifalco’s pseudoatomic potential [88] is used for the C<sub>60</sub>-C<sub>60</sub> interactions. (the full functional form is given in the Appendix (page 127)) This potential is derived by integrating a Lennard-Jones (LJ) function over the surface of two spheres, assuming uniform carbon atom density. The resulting C<sub>60</sub>-C<sub>60</sub> attractive energy, 6.4 kcal/mol, is considerable and helps explain the C<sub>60</sub>s’ tendency to aggregate. For Ph-Ph interactions, we use a potential from a coarse grained model [95] of liquid crystals. In this model, each Ph group is rotationally averaged and reduced to a single LJ interaction site. Similarly, for the molecules considered here the phenyl groups can rotate around one axis, with some hindrance.

We have developed our own CA-CA potential aimed at minimizing computational expense while reproducing the interaction anisotropy. Similar potentials have been used to efficiently model anisotropic interactions at a range of size scales.

Examples include the hydrogen bonding of 2D water [118], DNA base pair interactions [119], assembly of patchy colloidal particles [120], and virus capsid assembly [121]. Our functional form consists of a Morse potential between UA interaction sites, an orientational multiplier to favor dimer alignment, and an isotropic repulsion term.

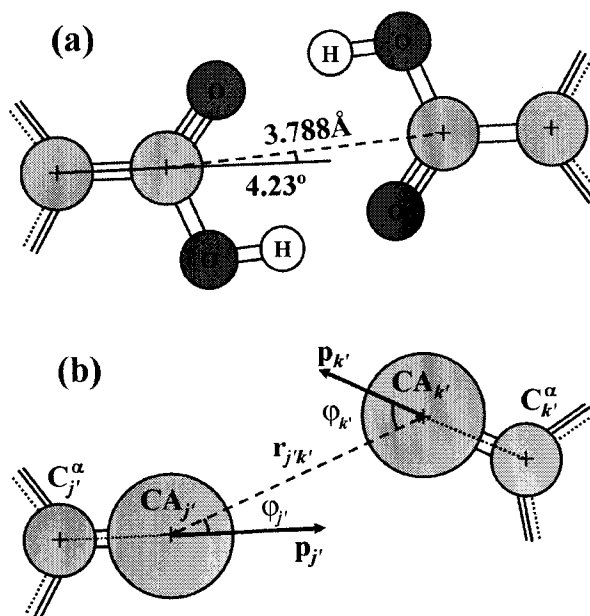


Figure III-2. The geometries and variables used to describe CA-CA hydrogen bonding interactions. (a) The benzoic acid dimer minimized using the Merck Molecular Force Field (MMFF). (b) The UA representation where CA pseudoatoms are centered at the carboxyl carbon atoms. To mimic the dimer configuration of (a), the CA-CA potential includes an anisotropy term which favors alignment of the p vectors shown in (b).

The potential is designed to reproduce the Merck Molecular Force Field [122] (MMFF94) minimized benzoic acid dimer shown in Figure III-2(a). Each carboxyl group is reduced to a CA pseudoatom placed at the respective carboxyl carbon. This is illustrated in Figure III-2(b). CA groups interact via a Morse potential

$$U_{M,CA}(r_{j'k'}) = E_{CA} \left( \left( 1 - e^{-\rho(r_{j'k'} - r_e)} \right)^2 - 1 \right), \quad (\text{III.1})$$

where the equilibrium energy,  $E_{CA} = 17.33$  kcal/mol, and separation,  $r_e = 3.788$  Å, match those of the MMFF dimer. Here,  $r_{j'k'}$  is the length of the interparticle vector,  $\mathbf{r}_{j'k'}$ . Using  $\rho = 1.45 \text{Å}^{-1}$  for the range parameter reproduces MMFF values within 1% for distances of 3.40 to 4.20 Å along the linear separation coordinate.

Although the benzoic acid dimer is bent 4.23°, we set the dimer to prefer collinear CA-C $^\alpha$  bonds (the  $\alpha$  superscript denotes the atom/group bonded to the carboxyl carbon). To specify this optimal bonding direction, a vector,  $\mathbf{p}$ , is defined in the direction of the C $^\alpha$ -CA bond. In Figure III-2(b), the example of an arbitrary geometry for two CAs, shows vectors  $\mathbf{p}_{j'}$  and  $\mathbf{p}_{k'}$  forming angles  $\varphi_{j'}$  and  $\varphi_{k'}$ , respectively, with the interparticle vector  $\mathbf{r}_{j'k'}$ . Using these angles, the multiplicative term

$$U_{ang}(\varphi_{j'}, \varphi_{k'}) = e^{-\varphi_{j'}^2/2\sigma^2} e^{-\varphi_{k'}^2/2\sigma^2}, \quad (\text{III.2})$$

scales  $U_{M,CA}$  for non-ideal orientations. The parameter  $\sigma$  determines how sharply the attractive energy decreases for bent geometries. Preliminary simulations of terephthalic acid have shown that  $\sigma = 0.4$  radians is large enough to allow bending, but small enough to energetically favor dimer configurations over trimers and disordered aggregates.

It is possible for some orientations that  $U_{ang}$  could be near zero, allowing non-physical overlap between CA groups. To counter this, a steep harmonic repulsion,  $U_{rep}$ , is added to the previous terms. Here,

$$U_{rep}(r_{j'k'}) = \begin{cases} 0 & r_{j'k'} > r_0 \\ k_{rep}(r_{j'k'} - r_0)^2 & r_{j'k'} \leq r_0 \end{cases}, \quad (\text{III.3})$$

where  $U_{M,CA}(r_0) = 0$ , and  $k_{rep} = 150$  kcal/mol-Å. With this, the complete CA-CA potential function is written as

$$U_{CA-CA}(r_{j'k'}, \varphi_{j'}, \varphi_{k'}) = U_{M,CA}(r_{j'k'}) * U_{ang}(\varphi_{j'}, \varphi_{k'}) + U_{rep}(r_{j'k'}). \quad (\text{III.4})$$

All mixed interactions between UA groups are calculated with LJ potentials. The distance and energy parameters are obtained using the Lorentz-Bertholet combining rules [104] – the only exceptions are the energies for C<sub>60</sub>-CA and Ph-CA interactions. The discrepancy arises because the CA-CA interaction is highly anisotropic – its binding energy of 17.33 kcal/mol is only for the linear geometry – while the Ph-Ph and C<sub>60</sub>-C<sub>60</sub> interactions are isotropic. Thus to account for all possible orientations we use estimated well depths of 1.0 kcal/mol for C<sub>60</sub>-CA and Ph-CA interactions.

Finally, all of the UA pairwise potentials described above are subject to a distance cutoff of 30Å.

## **2. UA-Au(111) interactions**

Here, the interactions of each UA group with the Au(111) substrate are detailed. The C<sub>60</sub>-Au(111) potential [107] we use is designed to reproduce the energetics of Wang and Cheng's DFT study of a single C<sub>60</sub> on Au(111) [20]. Our approach uses a z-dependent Morse potential for the average attraction and an x-y corrugation function to reproduce the C<sub>60</sub>'s preference for atomic threefold sites. The corrugation also reproduces the lateral barrier to site migration over twofold (bridge) sites. For both the DFT results and our potential, the energies for C<sub>60</sub> over a threefold site (minimum) and bridge site (saddle) are -29.2 and -26.0 kcal/mol respectively. The full functional form is given in the Appendix (page 127).

In contrast, Ph-Au(111) interactions are known to be considerably weaker, on the order of 1 kcal/mol for ideal, flat-lying orientations. [123] To also account for less preferred perpendicular orientations (recall that the Ph pseudoatom is orientationally averaged) we use a z-dependent LJ potential with a well depth of 0.5 kcal/mol.

A DFT study has reported [124] that CA-Au(111) interactions are repulsive so long as the CA group does not deprotonate and the surface is flat (i.e. free of adatoms, step edges, and vacancies). Accordingly, we use a short range repulsive potential to prevent CA groups from penetrating the surface. This potential is written as

$$U_{CA-Au(111)} = E_{rep} e^{-\kappa z}, \quad (\text{III.5})$$

where  $z$  is the height of the CA group above the x-y plane,  $E_{rep} = 1 \times 10^{14}$  kcal/mol, and  $\kappa = 11.5 \text{ \AA}^{-1}$ . With these values,  $U_{CA-Au(111)} > 1$  kcal/mol for  $z < 2.8 \text{ \AA}$ .

## **D. Simulation Methods**

### **1. Monte Carlo Cooling**

NVT Metropolis Monte Carlo (MMC) cooling simulations are carried out to determine low temperature structures, phase transitions, and thermal averages of energetics and structural properties. The simulation region is a box with the Au(111) surface lying in the global x-y plane. x and y box dimensions only differ slightly to match the substrate periodicity. Beyond the x and y box dimensions and for  $z > 50 \text{ \AA}$ , a harmonic restoring potential prevents evaporation. Sub-monolayer surface coverages (0.2 to 0.4 molecules/nm<sup>2</sup>) are used so that patterns result from attractive intermolecular forces, not crowding. Preliminary results using periodic boundary conditions showed high sensitivity to the interplay of box dimensions and C<sub>60</sub> adlayer spacing and substrate periodicity.



Thus to avoid imposing a specific symmetry on the system, periodic boundary conditions are not used.

Unbiased starting configurations for clusters of  $N=50$  molecules are generated by assigning each molecule a random position within the box and a random unit-quaternion orientation. The system is cooled from high simulation temperature (typically starting around 1600K to ensure randomization) in decreasing steps of 50K. At each temperature, single-molecule translation and rotation trial moves are equally probable and acceptance is determined using the standard Metropolis scheme. The three components of translational moves are chosen from the flat interval  $[-\delta\tau, \delta\tau]$ . Each rotation angle about a randomly chosen axis (through the molecular origin) is chosen from the flat interval  $[-\delta\omega, \delta\omega]$ . During an initial equilibration period at each temperature,  $\delta\tau$  and  $\delta\omega$  are adjusted to give approximately a 50% acceptance fraction, and no statistics are recorded. During data collection,  $\delta\tau$  and  $\delta\omega$  remain fixed. A single MC cycle is defined to be  $N$  (in all cases here,  $N=50$ ) trial moves and between  $2 \cdot 10^6$  and  $5 \cdot 10^6$  data collection cycles are carried out at each  $T$ . The system configuration is preserved when the temperature is decreased.

For all molecules, initial runs with small clusters of  $N=25-30$  are qualitatively identical to the  $N=50$  runs reported here. Due to finite size effects, small quantitative differences in energetics are present. However, the low- $T$  pattern symmetries, structural order parameters, and phase phenomena are nearly indistinguishable.

One particular limitation of this modeling approach is worth noting. The surface is treated as a rigid body and internal degrees of freedom for all the molecules are neglected. Therefore, phenomena noted at a given simulation temperature will not

necessarily occur at the same experimental temperature. However, we stress that the canonical Monte Carlo approach used here is a well-established and well-understood approach to sampling the entire potential energy landscape. [83]

## **2. Energetics and Order Parameters**

To help relate the different types of physical interactions and the observed behavior, the system's total potential energy,  $U$ , is partitioned into the following components:  $U_{HB}$ , from CA-CA hydrogen bonding interactions;  $U_{vdW}$ , the remaining intermolecular interactions; and  $U_{surf}$ , the interactions with the Au(111) surface.

Averages are accumulated for each component of  $U$  and reported values are divided by  $N$ , putting them on a per-molecule basis.

Using the first and second moments of  $U$ , the heat capacity (per molecule) is calculated at each temperature,  $T$ , using

$$C_v = N \frac{\langle U^2 \rangle - \langle U \rangle^2}{k_B T^2}, \quad (\text{III.6})$$

where  $k_B$  is the Boltzmann constant. The standard deviation of five block  $C_v$  values is used as a relative measure of uncertainty.

To relate energetics and heat capacity to structural changes, we use structural order parameters to quantify hydrogen bond formation, spatial packing, and orientational order. Here we describe the specific order parameters used in this study.

Two order parameters are used to count hydrogen bonding (HB) interactions between CA groups. The first,  $HBNN$ , is the number of CA nearest neighbor (NN) interactions within a cutoff of  $5\text{\AA}$ , regardless of orientation. The second, more stringent measure,  $HB2$ , counts dimer interactions that are within the same cutoff distance but are

also aligned such that  $\varphi_j, \varphi_k \leq 10^\circ$  (these angles are defined in Section III.C.1 and Figure III-2). Both HB parameters are scaled to give the number of HB interactions per molecule.

The order parameter  $\chi_6^2$  is used to measure 2D hexagonal close-packing [125] of fullerenes in the first monolayer. We define the first monolayer to be all molecules with  $C_{60}$  centers no more than  $6.1\text{\AA}$  above the x-y plane (the uppermost Au(111) layer). Within the monolayer, all  $C_{60}$  NN bonds,  $\mathbf{r}_{jk'}$ , shorter than  $13\text{\AA}$  are used to calculate

$$\chi_6^2 = \left\langle \left| e^{i6\Phi_{jk'}} \right| \right\rangle^2, \quad (\text{III.7})$$

where  $\Phi_{jk'}$  is the angle between the global x-axis and the projection of  $\mathbf{r}_{jk'}$  on the x-y plane (any fixed direction in the surface plane would give equivalent results) and  $i$ , here, is the imaginary unit (otherwise, 'i' is a configuration index).  $\chi_6^2$  is zero for structures such as disordered solids or 2D gases and it approaches unity as hexagonal ordering sets in. Similar to this, the order parameter  $\chi_4^2$ , which measures square monolayer packing, was calculated for all simulations. However, square packing was not observed in any of the present simulations, so the results have been omitted.

To measure orientational ordering, we use two order parameters which are based on  $P_2$ , the second Legendre Polynomial.  $P_2$  can gauge parallel alignment between two vectors using their intersection angle,  $\psi$ , and it is written as

$$P_2(\psi) = \frac{3\cos^2(\psi) - 1}{2}. \quad (\text{III.8})$$

Possible  $P_2$  values range from  $-1/2$ , for perpendicular vectors, to unity, for parallel ones, and its spherical (isotropic) average is zero. The  $P_2$  formalism is flexible and it can be used to compare a molecule's orientation to a stationary reference or to compare a pair of neighboring molecules' orientations.

First, we define the order parameter  $P_{2t}$  to measure "tilting" of a molecule's body fixed z-axis,  $\mathbf{z}_{bf,j}$ , (this axis passes through the bonded  $C_{60}$  and Ph groups. See Figure III-1 for molecule axis definitions) relative to the surface normal,  $\mathbf{z}$ , using the expression

$$P_{2t}(\mathbf{z}_{bf,j}) = \frac{3(\mathbf{z}_{bf,j} \cdot \mathbf{z})^2 - 1}{2}, \quad (\text{III.9})$$

where the subscript  $j$  indicates a specific molecule and the (unit) vector dot product replaces the cosine term of (IV.6). Reported values of  $P_{2t}$  are configuration averages over all molecules  $j$ .

The second orientational order parameter  $P_{2x}(\mathbf{x}_{bf,j}, \mathbf{x}_{bf,k})$  measures alignment between the body fixed x-axes of neighboring molecules  $j$  and  $k$ . It is expressed as

$$P_{2x}(\mathbf{x}_{bf,j}, \mathbf{x}_{bf,k}) = \frac{3(\mathbf{x}_{bf,j} \cdot \mathbf{x}_{bf,k})^2 - 1}{2}, \quad (\text{III.10})$$

where the axis vectors are of unit length. Reported values of  $P_{2x}$  are configuration averages over all molecule pairs with centers within  $20\text{\AA}$ .

## **E. Results and Discussion**

### **1. Neat $C_{60}$**

Prior to discussing our results for functionalized fullerenes, we first report simulation results of bare  $C_{60}$  on the Au(111) surface. This serves to demonstrate the

behavior of our  $C_{60}$ -Au(111) potential and to introduce the adlayers observed in the later sections.

(a) Hexagonal Monolayers

Experimentally, several close-packed  $C_{60}$  adlayers have been identified on the Au(111) substrate. In our simulations, two of these structures have been observed. These have unit cells  $(2\sqrt{3} \times 2\sqrt{3})R30^\circ$  [21] and  $(\sqrt{13} \times \sqrt{13})R14^\circ$ , [25,73] respectively. For these two adlayer structures, the spacings of the equivalent three-fold sites occupied by the fullerenes are  $9.98\text{\AA}$  ( $R30^\circ$ ) and  $10.39\text{\AA}$  ( $R14^\circ$ ). We note that these bracket the preferred  $C_{60}$  dimer spacing of  $10.06\text{\AA}$  [88]. Thus, for both adlayers, registry with the threefold sites causes a small amount of molecule-molecule interaction strain. The  $R30^\circ$  adlayer is slightly lower in energy using our potential and is generally recognized to be the energetic ground state in experimental studies [21]. Hence our parameterization describes the essential experimental results for neat fullerene on Au(111) semi-quantitatively.

(b) Temperature Dependent Structural Behavior

In Figure III-3 we show results from simulation of neat  $C_{60}$  on Au(111) as a function of temperature. The panels show: (a) the heat capacity,  $C_v$ ; (b) the order parameter  $\chi_6^2$ , (c) the several potential energies  $U$ ,  $U_{vdW}$ , and  $U_{surf}$  – all as a function of  $T$ . In Figure III-4, we show configurations snapshots at different temperatures. We consider first the data in Figure III-3. The heat capacity curve shows a clear local maximum at  $T = 1100\text{ K}$ . Such maxima in cluster calculations indicate a transition between one type of adlayer phase behavior and another. [89] In Figure III-3(b), the

hexagonal order parameter,  $\chi_6^2$ , shows an abrupt change at this same temperature,  $T=1100\text{K}$ , dropping from unity at lower temperatures to zero at higher temperatures. This indicates a high degree of 2D hexagonal packing at lower temperatures, and very little at higher temperatures. In fact, at temperatures above  $1100\text{K}$ , (see for instance, Figure III-4 panel (d)), the fullerenes do not cluster, and diffuse as a 2D gas. Below  $1100\text{K}$ , the fullerene surface cluster is close-packed (Figure III-4 panels (a)-(b)). Examination of the potential energy (Figure III-3 panel (c)) also shows a change at  $T=1100\text{K}$ . It is clear from the data in panel (c) that the phase transition is derived from the conspicuous change in the intermolecular contribution to the potential energy ( $U_{vdw}$ ) rather than to any change in molecule-surface interaction ( $U_{surf}$ ). Thus, we can assign the  $C_v$  peak to a transition from ordered close-packed adlayer to disordered 2D gas.

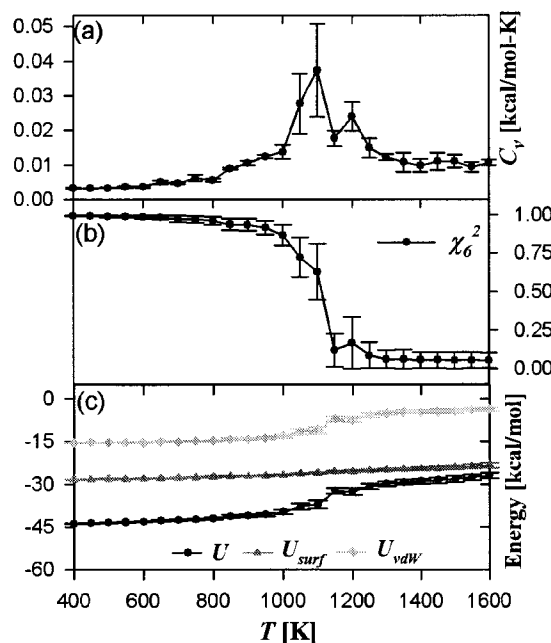


Figure III-3. (a) Heat capacity,  $C_v$ , (b) hexagonal order parameter,  $\chi_6^2$ , and (c) intermolecular potential energy as a function of temperature for neat  $C_{60}$ .

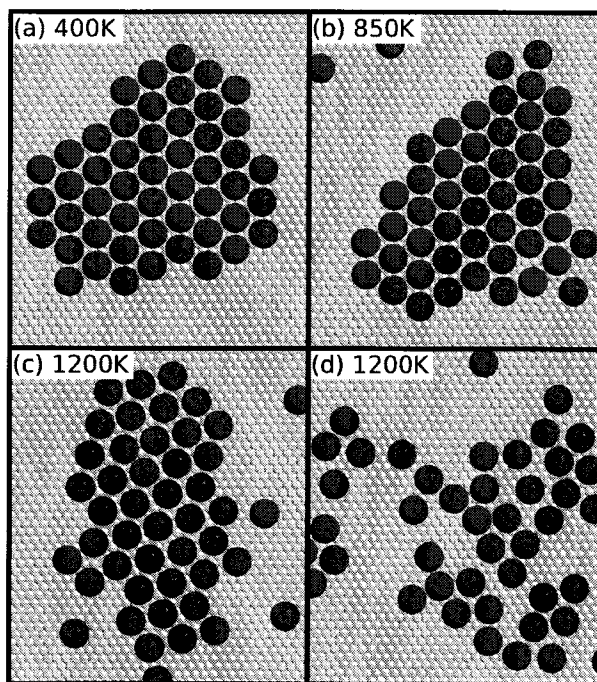


Figure III-4. Configuration snapshots at selected temperatures taken from the simulation of neat  $C_{60}$ .

As noted above, at temperatures below the phase transition (1100K), the adlayer is close-packed, as evidenced by the  $\chi_6^2$  parameter. However,  $\chi_6^2$  cannot distinguish between the  $R30^\circ$  and  $R14^\circ$  hexagonal adlayers. At the lowest temperatures, we observe mostly the  $R30^\circ$  structure in snapshots such as Figure III-4 (a)-(b). Closer to the phase transition, we see more of the metastable  $R14^\circ$  adlayer as is shown in Figure III-4(c) at 1200K. There is not sufficient detail for us to distinguish a phase transition between these two adlayers.

## 2. Molecule 1

In Figure III-5 we show results from the simulation of molecule 1. In addition to the variables shown in Figure III-3, the orientational order parameters  $P_{2x}$  and  $P_{2t}$  are included in panel (b) and hydrogen bond parameters  $HBNN$  and  $HB2$  are added to panel

(c). In this case there appear to be two peaks in the heat capacity, indicating two phase transitions. The higher- $T$  peak occurs at about 1200K; the lower- $T$  peak occurs at about 850K. It can be seen that the higher  $T$  transition corresponds to the transition already commented on above for neat fullerenes. That is, at this temperature, the system goes from a disordered (2D “gas”) phase to the spatially ordered, close-packed 2D solid phase. This is confirmed by monitoring the  $\chi_6^2$  parameter and  $U_{vdW}$ , both of which behave similarly to the previous case of bare  $C_{60}$ . Representative configuration snapshots at 1000K and 1400K in Figure III-6 (panels (c) and (d)) provide support for this assertion. We further note that the fullerene moieties form the  $R30^\circ$  adlayer described earlier. This  $R30^\circ$  adlayer structure has also been observed in experiments with functionalized fullerenes on Au(111), [114] where it is found that small functional groups do not disrupt the fullerene close-packing and surface registry.



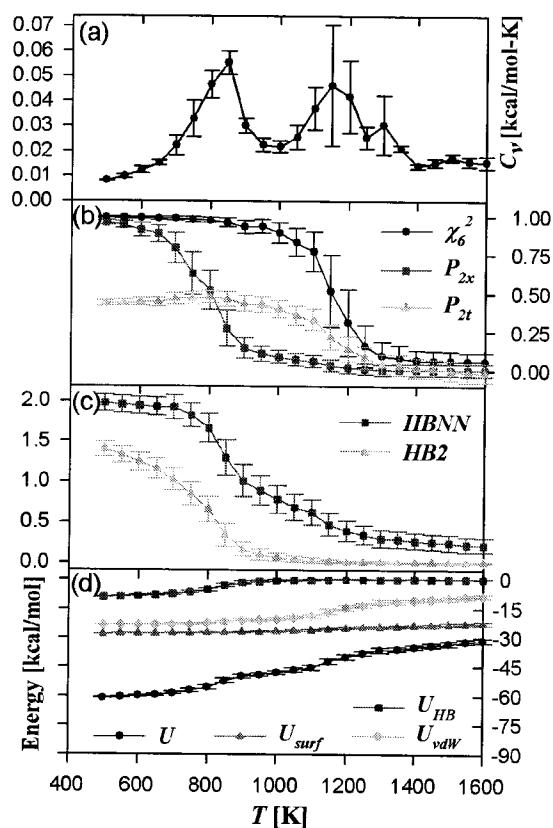


Figure III-5. (a) Heat capacity,  $C_v$ , (b) hexagonal order parameter,  $\chi_6^2$ , and orientational order parameters  $P_{2x}$  and  $P_{2t}$ , (c) hydrogen bonding order parameters  $HBNN$  and  $HB2$ , and (d) intermolecular potential energy as a function of temperature for Molecule 1.

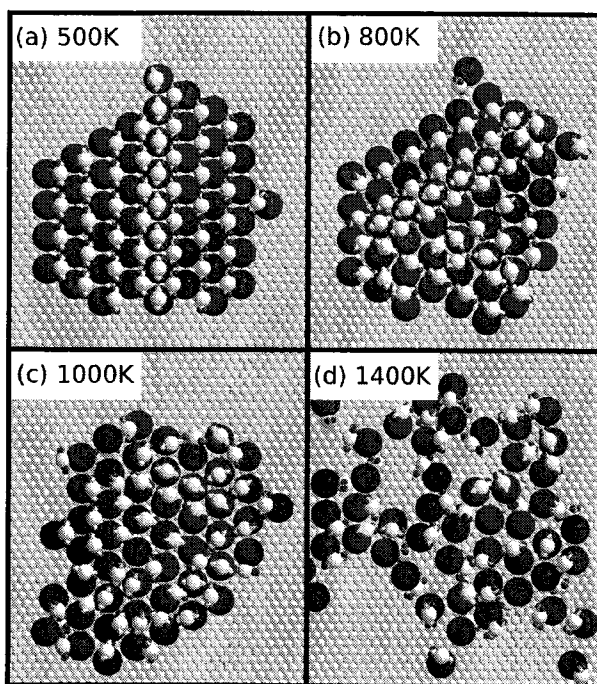


Figure III-6. Configuration snapshots at selected temperatures taken from the simulation of Molecule 1.

In the temperature region between 1200 and 850 K, we observe a new phenomenon. The adlayers show hexagonal close-packing of the fullerenes (as evidenced by the  $\chi_6^2$  parameter) but are disordered with respect to the hydrogen bonding. This is illustrated by  $P_{2t}$  and the nearest-neighbor hydrogen bonding count ( $HBNN$ ). The order parameter  $P_{2t}$  (Figure III-6(c)) shows that the mean polar tilt angle (between a molecule's  $\mathbf{z}_{bf}$  axis and the global z-axis normal to the substrate plane) is limited and all molecules are nearly upright.  $P_{2x}$ , however, indicates that rotations about the molecules'  $\mathbf{z}_{bf}$  axes are nearly unrestricted and  $HB2$  and  $HBNN$  show that each molecule has, on average, less than 1 hydrogen bond. The substituent arms are sufficiently short, relative to the molecular spacing, that repulsive barriers do not hinder rotation.

When cooled below 850K, the system undergoes a different phase transition to an orientationally ordered hydrogen-bonded structure, as can be seen from Figure III-6, panels (a) and (b). Here, hydrogen bonds link NN molecules' substituent arms and restrict their rotation resulting in extended linear hydrogen-bonded rows. Due to the hexagonal adlayer symmetry, degenerate rows can form in multiple directions as is seen in Figure III-6(b). The sudden increases in  $P_{2t}$  and  $HB2$  and the decrease in  $U_{HB}$  also confirm this structural change.

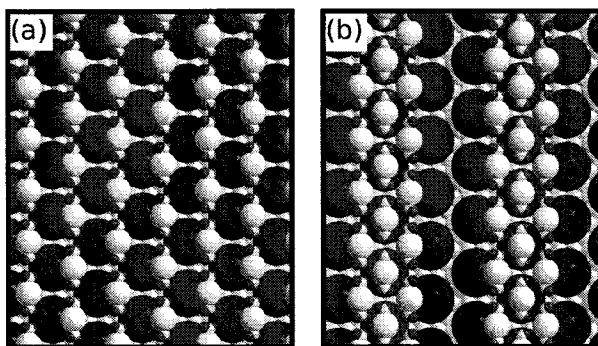


Figure III-7. Idealized structures of molecule 1 having a periodicity of one row (a) and three rows (b). Due to the gain in intermolecular dispersion interactions, (b) is energetically preferred.

Closer examination of snapshots of the low- $T$  results (Figure III-6(a),(b)) reveals that there are, in fact, two competing adlayer structures. In both structures, substituents form 1D rows due to hydrogen bonding between nearest neighbor molecules. (This is reminiscent of the extended hydrogen-bonded rows formed by terephthalic acid on the same substrate [58]). However, the two structures differ in the way the molecular rows tilt and the row periodicity. Defect-free, energy minimized versions of these structures are shown in Figure III-7. One (Figure III-7(a)) has a structure where all molecules have equivalent orientation and each row is a shifted copy of its neighboring rows. Here the rows lean to the same side and gain a small amount of vdW attraction energy by

contacting the underlying  $C_{60}$  lattice. In the other pattern (Figure III-7(b)), groups of three rows tilt together with the center row held upright by a row leaning in from each side.

There is an increased intermolecular dispersion interaction for the molecules in the center of each row. An all-atom treatment of Ph groups with internal degrees of freedom could perhaps provide further insight into these structures. However, for the potential parameters used here they are essentially degenerate. The details of which type of adlayer is preferred will also likely be a sensitive function of the potential parameters. We do not pursue either of these possibilities further in the present work.

### **3. Molecule 2**

We turn now to a discussion of the simulation results for molecule **2** (see Figure III-1). The substituent arms of **2** have two more Ph groups than does molecule **1**, separating its CA groups by  $14.5\text{\AA}$  (approximately 1.5 times the lattice constant of the  $C_{60}$  close-packed adlayer). Simulation results are shown in Figure III-8 with representative snapshots in Figure III-9. The contrast of the heat capacity,  $C_v$ , with that of molecule **1** is striking: there is a single peak in this case occurring at 1100K. All the other order parameters show abrupt changes at the same temperature (Figure III-8 (b),(c)) as do the intermolecular interactions  $U_{HB}$  and  $U_{vdW}$  (Figure III-8 (d)). Therefore, for this molecule, the orientational ordering transition due to hydrogen bonding occurs at the same temperature as the transition due to the  $C_{60}$  close-packing.

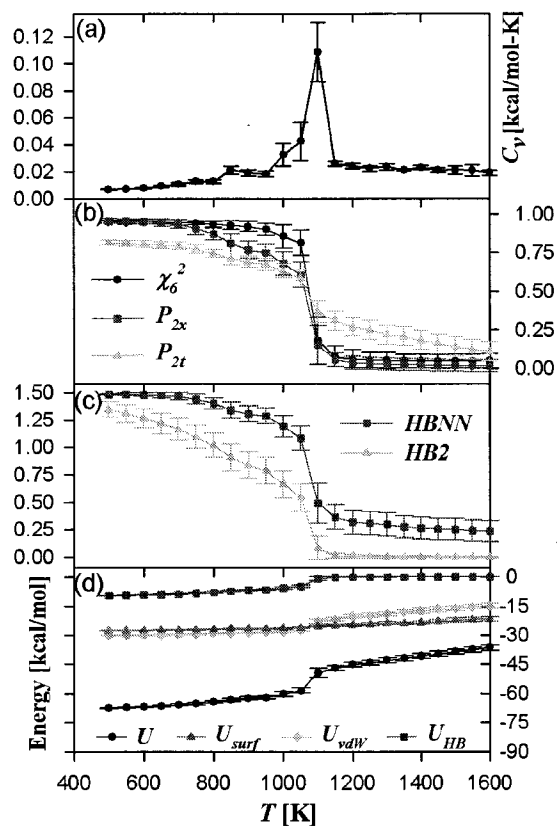


Figure III-8. (a) Heat capacity,  $C_v$ , (b) hexagonal order parameter,  $\chi_6^2$ , and orientational order parameters  $P_{2x}$  and  $P_{2t}$ , (c) hydrogen bonding order parameters  $HBNN$  and  $HB2$ , and (d) intermolecular potential energy as a function of temperature for Molecule 2.

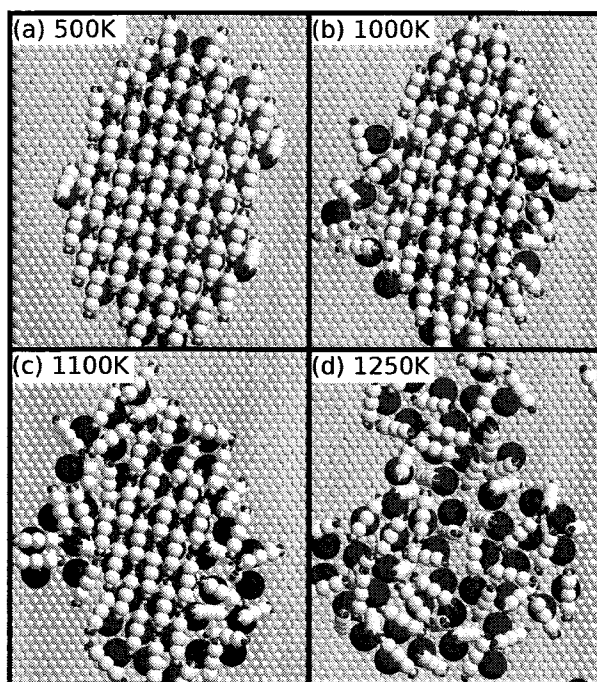


Figure III-9. Configuration snapshots at selected temperatures taken from the simulation of Molecule 2.

Examination of the snapshots in Figure III-9 yields some insight into this. Near the transition temperature, at 1000K and 1100K (panels (b) and (c)), intermediate structures from the melting transition show disordered edge molecules surrounding an ordered nucleus. Within the ordered nucleus, molecules are sterically constrained by the close-packing so that free rotation of the substituent arms is no longer possible. Due to their length, the arms interdigitate to avoid steric repulsion. Consequently, the CA groups of second NN molecules can dimerize. We note that the  $C_{60}$  moieties form the lower density  $R14^\circ$  adlayer to relieve compression strain in the hydrogen bonding interactions. Although it would relax the  $C_{60}$ - $C_{60}$  interactions, the more compact  $R30^\circ$  adlayer would further strain the hydrogen bonds and could force the substituents to buckle. We remarked earlier that the  $R14^\circ$  adlayer is metastable for bare  $C_{60}$ . Here, however, it appears to be the preferred ground state due to the substituents' geometry. Duplicate runs

with different random seeds also reached the  $R14^\circ$  structure when cooled, showing the minimum to be formed robustly.

The fullerene packing structure can be detected by STM studies. [109] However, STM is often unable to resolve the structure of the functional groups. The fact that this functionalization causes a change in the underlying  $C_{60}$  close-packing suggests the effects of functionalization may be indirectly investigated experimentally by STM. Indeed, this has been commented on by Chen and coworkers [114] who detect solely the  $R30^\circ$  fullerene phase with derivatized fullerenes, rather than the mixture of fullerene phases observed with bare fullerenes. [21,22]

#### **4. Molecule 3**

We continue the trend of making the substituent arms longer by using five phenyl moieties to separate the COOH groups. This results in molecule **3** (Figure III-1). Simulation results are shown in Figure III-10 and Figure III-11. In this case neither set of the energetics and order parameters (Figure III-10) nor the configuration snapshots (Figure III-11) show any evidence of distinct phase transitions or ordered structure formation. The system gradually freezes into a “glassy” state, with little global order. This result can be understood by considering the preferred ordering of the  $C_{60}$  moieties and substituent arms separately.

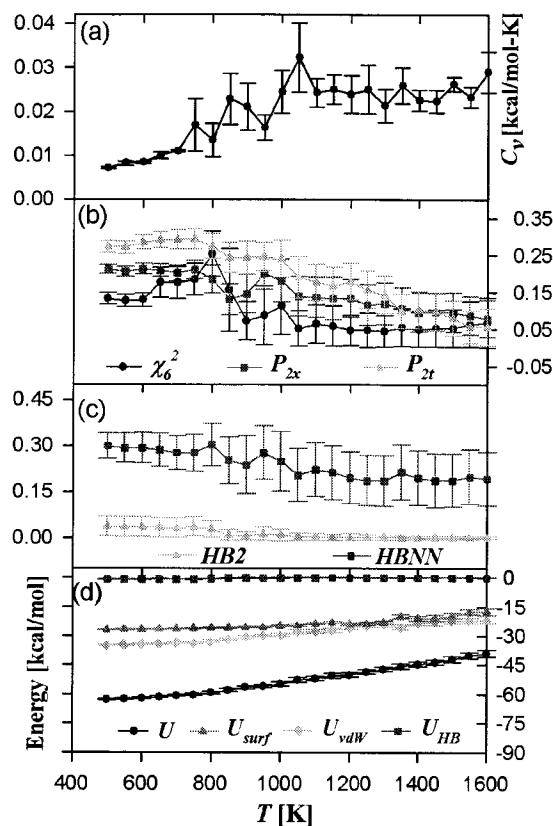


Figure III-10. (a) Heat capacity,  $C_p$ , (b) hexagonal order parameter,  $\chi_6^2$ , and orientational order parameters  $P_{2x}$  and  $P_{2t}$ , (c) hydrogen bonding order parameters  $HBNN$  and  $HB2$ , and (d) intermolecular potential energy as a function of temperature for Molecule 3. Note that the ordinate scale does not run to 1 in panels (b) and (c).



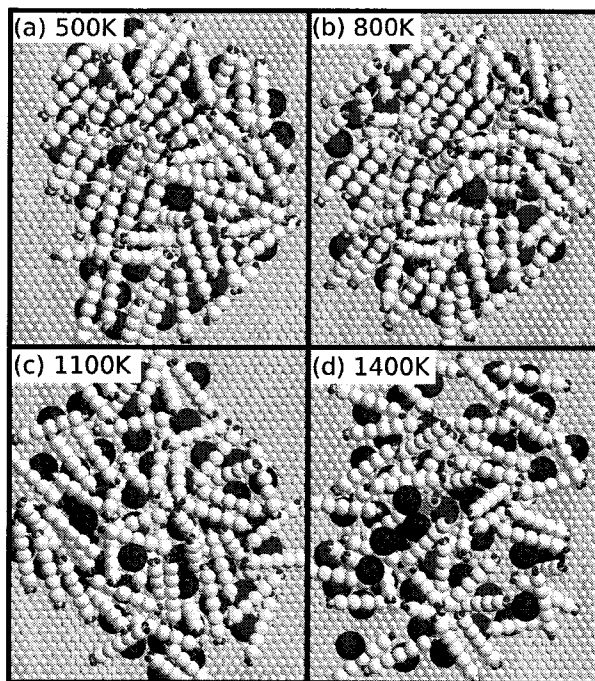


Figure III-11. Configuration snapshots at selected temperatures taken from the simulation of Molecule 3.

The previous results – neat  $C_{60}$  in particular – have established that  $C_{60}$  moieties prefer to form close-packed monolayers at low temperatures. Here, however, the snapshots as well as the unchanging  $\chi_6^2$  order parameter show that  $C_{60}$  moieties of **3** cannot close-pack. This result is due to steric hindrance caused by the large substituent groups. Alternatively the cylindrical CA-Ph<sub>5</sub>-CA substituents alone should prefer an aligned, nematic or smectic type structure due to their large aspect ratio. However, the attached  $C_{60}$  moieties' size and tendency to aggregate prevent extended orientational ordering. In fact, inspection of the  $P_{2x}$  parameter shows no evidence of substituent arm alignment at any temperature.

The result of these competing interests is mutual frustration and neither spatial nor orientational ordering.  $C_{60}$  close-packing is frustrated by the large substituent arms and

the substituents' preferred alignment is hindered by the  $C_{60}$ s' size and attraction. As a consequence of this, hydrogen bonding is not readily feasible. We find, indeed, that at all temperatures,  $U_{HB}$  is negligible and the order parameters  $HBNN$  and  $HB2$  show no evidence of hydrogen bonding interactions occurring.

#### **5. Molecule 4**

We have continued investigating systematic trends. One such is to reconsider **2** and remove the hydrogen bonding CA groups. This results in molecule **4**. Thermal averages for simulations of this molecule are shown in Figure III-12 and typical geometries in Figure III-13. In this case  $C_v$  and  $\chi_6^2$  signal a phase transition at about 1000 K. This is due to the transition from 2D gas to a close-packed monolayer with fullerenes in the  $R14^o$  configuration. As the temperature is further reduced, the substituent arms show some tendency to self-organize, but there is no sharp  $C_v$  transition to an orientationally ordered phase. Rather, the onset appears more gradual and, at low  $T$ , there is visual evidence of herringbone pattern formation (Figure III-13(a)).

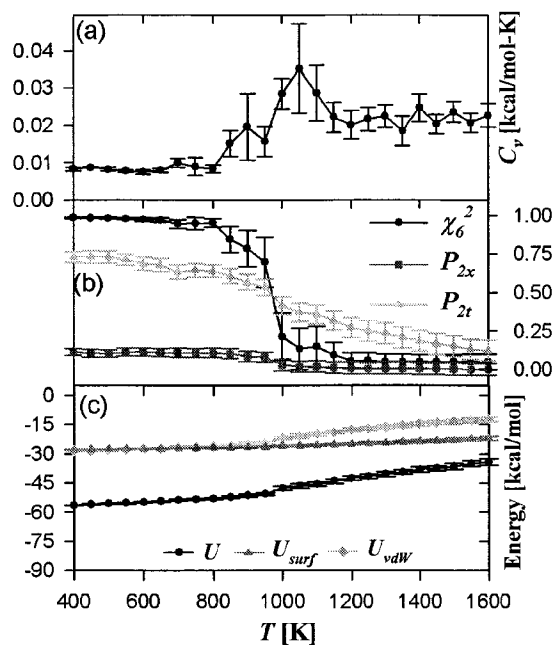


Figure III-12. (a) Heat capacity,  $C_v$ , (b) hexagonal order parameter,  $\chi_6^2$ , and orientational order parameters  $P_{2x}$  and  $P_{2t}$ , and (c) intermolecular potential energy as a function of temperature for Molecule 4.

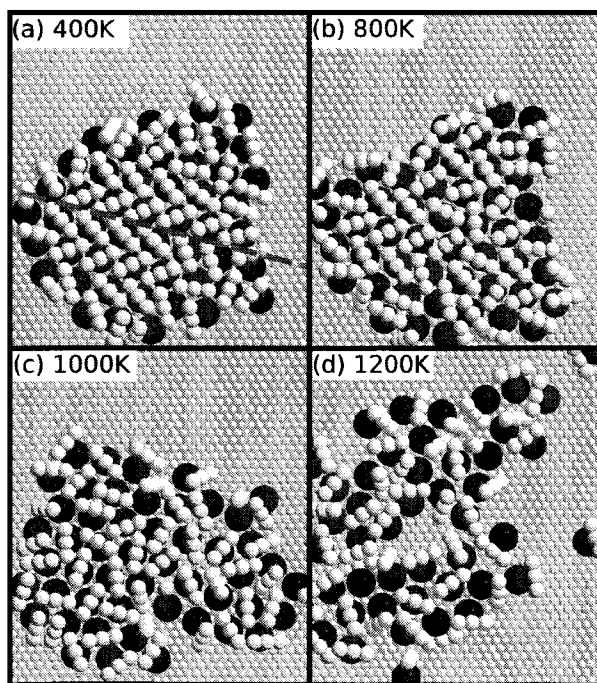


Figure III-13. Configuration snapshots at selected temperatures taken from the simulation of Molecule 4. The orange dashed line in panel (a) indicates a local glide symmetry axis.

Loosely defined, a herringbone pattern [126] consists of alternating 1D rows where constituents within a row are parallel but neighboring rows are divided by a reflection or glide symmetry axis. (The glide symmetry operation consists of a reflection across an axis and a translation parallel to it.) In the “ideal” herringbone structure, molecules from adjacent rows are perpendicular to each other and are twisted  $\pm 45^\circ$  relative to the symmetry axis between rows.

Similar herringbone patterns are commonly observed in model and experimental studies of linear molecules on surfaces. Examples include  $N_2$  [127] and hexane [126,128] on graphite, and model repulsive dimers on a hexagonal lattice. [129] “Ideal” herringbone ordering is easy to quantify for molecules constrained to a lattice (as is the case for most of the systems cited above) because the possible symmetry axes are predetermined. For the present study, however, a simple herringbone metric for the substituent arms is less obvious because, in general, the underlying  $C_{60}$  lattice can vary or have defects (at higher  $T$ ). Our main orientational order parameter,  $P_{2x}$ , is zero for both the isotropic limit and the ideal herringbone configuration. Thus no quantitative information on herringbone patterning is available from this parameter.

As  $T$  is reduced below the phase transition,  $P_{2x}$  increases slightly (Figure III-12(b)) since the substituent arms adopt a herringbone pattern but are not exactly perpendicular; rather they are twisted approximately  $\pm 37^\circ$  on average. Nevertheless, the herringbone patterning is clear upon visual inspection. In Figure III-13(a), one glide axis separating the herringbone rows is shown. We also point out that this patterning is chiefly in the cluster interior and that edge molecules remain disordered. Here, no hydrogen

bonds are present to orientationally lock the substituents. Instead, the neighboring molecules are less influential. It is the collective weak interactions with all six nearest neighbors that determine the herringbone ordering. Thus the edge molecules, with sufficient thermal energy and fewer than six NN, maintain some orientational disorder.

## **6. Molecule 5**

We now consider molecule **5**. This asymmetrical molecule is equivalent to molecule **2**, but with one of the Ph-CA groups removed. The energetics and structural data in Figure III-14 show that two phase transitions occur as the system is cooled. One is centered at 1200 K, corresponding to the fullerene close-packing. The other occurs at about 600 K, where the hydrogen bonding sets in. Figure III-15 shows representative configuration snapshots at several temperatures. Similar to what was observed for **2**, the substituent arm length allows the carboxyl groups of second-nearest-neighbor molecules to dimerize. However, the ground state structure is not merely that of **2** with substituent groups altered. Instead, the substituents' smaller size and single carboxyl functionality allow more diverse orientational arrangements. Here these are described further.

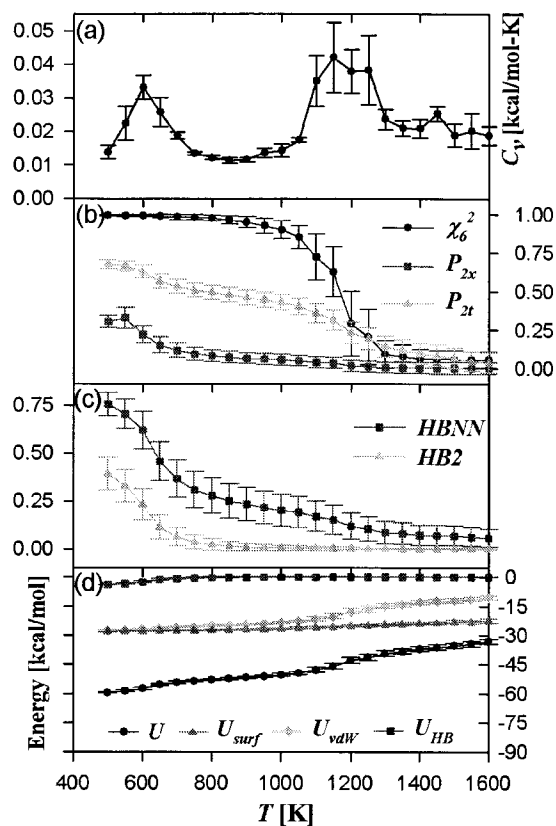


Figure III-14. (a) Heat capacity,  $C_v$ , (b) hexagonal order parameter,  $\chi_6^2$ , and orientational order parameters  $P_{2x}$  and  $P_{2t}$ , (c) hydrogen bonding order parameters  $HBNN$  and  $HB2$ , and (d) intermolecular potential energy as a function of temperature for Molecule 5.

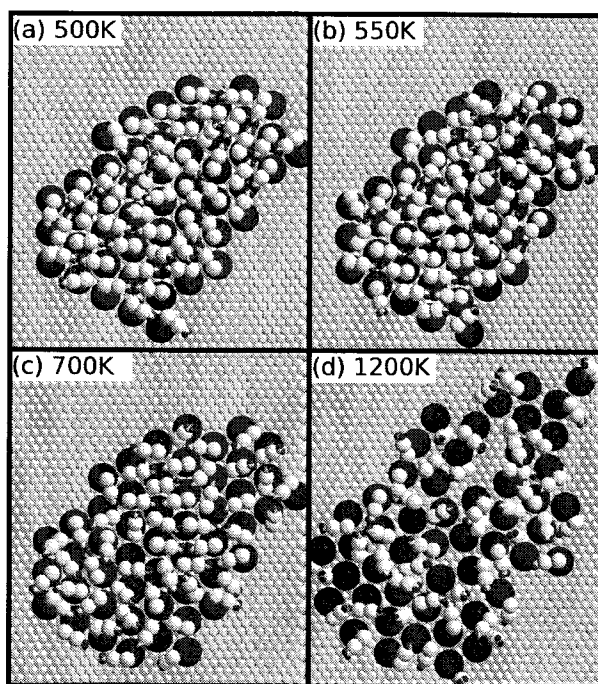


Figure III-15. Configuration snapshots at selected temperatures taken from the simulation of Molecule 5. The green lines in (a) highlight dimerized substituents.

At temperatures below 1200K the  $C_{60}$  close-packed hexagonal lattice is stable. Therefore, each CA group has six potential partners (second NN) with which to form a hydrogen bond. In contrast to the results for molecule 2, where the large substituents aligned to avoid steric repulsion, the smaller substituents of 5 are less restricted by their neighbors and can form non-parallel local motifs. Although most carboxyl substituents dimerize at low T, no global ground state structure is apparent from visual inspection of the low temperature snapshots. However, a local herringbone pattern of dimers is prominent in a few regions (see Figure III-15) and the increase of  $P_{2x}$  signals partial alignment below 600K. The lack of robust, long-range ordering lies in the strength and nature of the intermolecular interactions (as parameterized here). Energy differences in dimer arrangements result from the weak dispersion interactions and are small compared

with the hydrogen bonding energies. Thus, as was just noted, many configurations with similar energies can result from different pairings of substituents. However, interconversions are complex and require multiple hydrogen bonds to break and reform. Therefore the system is slow to relax and it is susceptible to kinetic trapping, making it less promising for robust self-assembly than was the case for molecules **1** and **2**.

## **F. Conclusions**

We have carried out classical NVT Monte Carlo simulations on a series of model fullerene derivatives adsorbed on Au(111). We focused particular attention on the effect of intermolecular hydrogen bonding in the self-assembly of the adlayers. Fullerenes functionalized with zero, one and two carboxylic acid groups were modeled. Intermolecular potentials were obtained by using a variety of sources, including recent DFT data for fullerenes on Au(111). [20] The simulations were run at a series of simulation temperatures from 400K to 1600K. The behavior of the adlayers as a function of simulation temperature was monitored using an array of order parameters as well as the heat capacity. A hexagonal order parameter shows the temperature at which the fullerene close-packing phase transition occurs. A  $P_2$  order parameter indicates the temperature at which orientational order-disorder transitions occur.

Unfunctionalized (bare) fullerenes form a hexagonal close-packed monolayer. Our model gives two slightly different possible close-packed morphologies. Similar results have been observed in experiment.

Fullerenes with  $C_{2v}$  geometry functionalized with two carboxylic acid groups in a linear configuration can form extended hydrogen bonded rows. Similar results for species such as terephthalic acid have been observed in experiment. We note that the nonplanar



structure of fullerene derivatives allows for the formation of two different adlayers with extended linear hydrogen-bonded rows. However, if the spacing between the carboxyl groups is too large because the arms become too long, simultaneous fullerene close-packing and hydrogen bonding is sterically frustrated and disordered adlayers result.

Molecules **1** and **2** show both orientational and close-packing order at low temperature. For molecule **1** orientational disorder sets in at a lower temperature than does disorder in the close-packing. Furthermore, molecule **1** is capable of forming extended one-dimensional hydrogen-bonded rows in two distinct adlayer geometries. For molecule **2**, the transitions occur at the same temperature. This is explained by the cooperative nature of the adlayer patterning: The close-packing geometry established by the fullerenes is well-suited for nearest neighbor intermolecular hydrogen bonding.

We have also investigated the self-assembly of a  $C_{2v}$  species, molecule **4**, which contains no hydrogen-bonding functional groups. Without the hydrogen-bonding interactions, molecules optimize dispersion interactions resulting in herringbone patterns.

Finally, we note a trend in this study between the size of the substituent arm and the close-packing behavior of the fullerene moieties. The smallest substituents (molecules **1** and **5**) allow the fullerenes to form the compact  $R30^\circ$  close-packed adlayer. Molecules **2** and **4**, bearing slightly larger substituents, adopt the lower density  $R14^\circ$  adlayer, presumably to minimize steric repulsion. Finally, molecule **3** is unable to close-pack due to prohibitive steric repulsion of its large substituents. This trend is in qualitative agreement with Chen and coworkers [114] who observe the compact  $R30^\circ$  structure for small substituents and disordered structures for large substituents. However, they did not report observing the  $R14^\circ$  adlayer, perhaps because the molecules they studied were

either too big or too small. Given that STM is a robust tool for discerning the different close-packed structures of fullerene derivatives, further systematic study, both experimental and theoretical, could be fruitful.

## CHAPTER IV

# FREE ENERGY LANDSCAPES OF BIS-FULLERENE CLUSTERS ON MODEL SURFACES

### A. Introduction

The previous two chapters have shown that fullerene-substrate and fullerene-fullerene attraction strongly influence patterning in self-assembled monolayers. For the fullerene-thiolate molecules studied in Chapter II, robust patterning was hindered by the competition for surface adsorption sites between  $C_{60}$  and S groups. One possible strategy to remedy this is to remove the thiol groups and let the  $C_{60}$  serve as the surface tether. This approach was investigated in Chapter III, and molecules formed ordered assemblies with hexagonal monolayer  $C_{60}$  packing [130]. An alternative strategy is to replace the thiol groups with another fullerene, thereby symmetrizing the molecules' structures and their substrate affinity. These bis-fullerene molecules and their self-assembly on surfaces are the subject of this chapter.

Currently, a number of methods are known for synthesizing bis-fullerenes, but there have been few studies of their structural behavior on surfaces. Many reported bis-fullerene compounds are covalently "bridged" by only several atoms, and numerous variations exist regarding the exact bridging atoms and the attachment points on the

fullerene cages [110,131-145]. A limited number of studies have used larger “bridging groups” to separate fullerene moieties [28,29,32,146-149].

In some cases, these molecules bearing multiple fullerenes have been studied on surfaces [28,29,110,131,132,146]. For those with very small bridging groups, the intermolecular C<sub>60</sub> spacing is very close to their preferred vdW distance ( $\approx 10.0\text{\AA}$  center to center), and the molecules form somewhat distorted hexagonal monolayers [110,131,132]. In contrast, a bis-fullerene with a 5 unit oligophenylenevinylene bridging group was found to form ordered rows on HOPG in 1,2,4-trichlorobenzene solution [146]. Also, the well known “nanocars” from the Tour group [28,29] have mainly been studied for their single molecule diffusion properties on surfaces.

To our knowledge, the only modeling studies of such molecules on surfaces have been MD simulations [27,93] of individual “nanocars.” Therefore, given the lack of systematic studies of bis-fullerene self-assembly on surfaces, preliminary modeling efforts seem worthwhile. In this chapter, we choose to study clusters of three different bis-fullerene molecules, each with a different “bridging group” built from connected phenyl (Ph) moieties. (Complete structural details are given in the Methods section)

An important consideration for this study is the strength of the attractive interaction between each fullerene and the substrate. For the fullerene thiolate studied in Chapter II, fullerenes adsorbed due to this strong attraction, and “ideal” SAM patterning was hindered (ideal meaning S atoms bound to gold, and fullerenes not bound to gold). In Chapter III, this attraction energy was less important, since all other molecule-substrate interactions were much weaker. Since bis-fullerenes have two fullerenes at opposite ends,

their attraction to the substrate should play a large part in determining whether molecules stand up (only one fullerene adsorbed) or lie down (both fullerenes adsorbed).

Large uncertainties exist for the strength of the C<sub>60</sub>-Au(111) interaction. Theoretical and experimental efforts have reported values ranging from 20-60 kcal/mol [20,21,25,74,75,150]. Because of the large uncertainty in this energy and because of its expected influence on adsorbate patterning, we treat the surface more generally in this chapter. Specifically, we remove the atomistic corrugation term (the functional form is detailed in the Appendix (page 127)) and we carry out simulations using different values of the fullerene-surface energy, denoted  $E_{FG}$ . Without corrugation specific to the Au(111) surface, the surface's attractive strength is its defining attribute. A surface defined this generally can therefore, in principle, represent a number of metal or semiconductor surfaces.

Regarding the “standing-up” and “lying-down” orientations described above, we expect that bis-fullerene SAMs may have multiple structurally distinct morphologies. In situations where such structures are separated by large energy barriers (much larger than the available thermal energy,  $k_B T$ ), linear cooling simulations tend to become trapped in one low-lying region or the other.

To ensure that disparate structure regions are thoroughly sampled in the present simulations, we use temperature replica exchange [82,83,151,152] in conjunction with our Monte Carlo approach from the previous chapters. Temperature Replica Exchange Monte Carlo (T-REMC, or simply REMC) simulations are widely used to improve configuration sampling in MC and MD simulations. The method assigns system replicas to different temperatures and advances them in parallel as standard MC simulations.

Occasionally, replica pairs attempt to exchange temperatures subject to a Boltzmann acceptance criterion. Crucially, repeated exchanges enable replicas to randomly climb up and down the temperature ladder and to descend in and out of local energy minima, thereby avoiding the trapping problem of a linear cooling approach.

The competition between different structural morphologies and the implications for self-assembly are best described in the context of free energy landscapes. In the ideal self-assembly scenario, a system has only one free energy minimum (the self assembled structure) and the free energy gradient will guide any initial configuration into this minimum. This is referred to as a “single-funnel” landscape or a “structure seeking” landscape [83]. In practice, many systems have multiple local free energy minima (multiple funnels) corresponding to different structure types. Depending on the depth of the competing minima and the free energy barriers to escape them, they can trap molecules in undesirable configurations and hinder direct self-assembly. Therefore, an accurate survey of a system’s free energy landscape – specifically the free energy minima, the barriers between them, and the corresponding structures – is a powerful tool for rationalizing and predicting self-assembly phenomena.

Calculating accurate free energy landscapes is a formidable task. The specific details of our approach are given in the Methods section and a brief sketch is presented here.

In molecular simulations, the relative free energy between two distinct states is determined from their relative occupation probabilities [82]. In the simplest case, two equally probable states have equal free energies. Because free energies are determined by

probabilities, simulations must repeatedly visit the important regions of configuration space for accurate probabilities to emerge from the statistical noise.

Unfortunately, a straightforward MC or MD simulation may never (on practical simulation timescales) locate inherently improbable states such as high free energy barriers or metastable minima. Or if the simulation is trapped in a metastable state it may never reach the ground state.

With this limitation in mind, we use two methods to promote thorough configuration sampling. The first is temperature replica exchange, as described above. Second, we carry out multiple, separate simulations using different values of the fullerene-substrate energy,  $E_{FG}$ . These range from 25-35 kcal/mol depending on the molecule. “Biasing” this energy over a range of values ensures that both standing-up and lying-down structures are thoroughly sampled.

The raw statistical data (to be used for free energy calculations) collected at different temperatures and different  $E_{FG}$  values is not directly compatible because of the imposed biasing. However, if these datasets have sufficient overlap in configuration space [82,153,154], they can be merged using statistical reweighting methods. Specifically, we use the weighted histogram analysis method (WHAM) [155] and temperature-WHAM (T-WHAM) [156] methods which iteratively rescale histogram data by minimizing differences in the overlapping regions.

With this combined sampling data, global free energy landscapes can be calculated and used to predict the self-assembly (or lack thereof) for clusters of bis-fullerenes.

The rest of this chapter is organized as follows. Section B describes the bis-fullerene molecules we study and details the simulation protocols. Section C presents and discusses simulation results. Concluding remarks are in Section D.

## **B. Methods**

### **1. Molecules Studied**

This study considers three bis-fullerene molecules, each with a different “bridging group” connecting its two fullerene moieties. Cartoon representations of the molecules – **6**, **7** and **8** – are shown in Figure IV-1. The  $C_{60}$  and Ph moieties are represented by blue and grey spheres, scaled to their respective vdW radii. The atomistic structures of the bridging groups are indicated and wavy lines denote the  $CH_2-C_{60}$  bonds. Also included in the figure are the relevant molecular dimensions and the body-fixed coordinate frame (given *bf* subscripts).

Molecules **6** and **7** are constructed using the same UA groups and dimensions as molecules **1-5** (see section III.B). The bridging group of molecule **8**, however, is a single anthracene moiety, not a polyphenylene species. For simplicity, we elect to use one Ph UA to represent each six-membered ring of the anthracene. The center to center spacing of Ph groups ( $2.45\text{\AA}$ ) matches that between anthracene’s ring centers.

For all three molecules, the  $C_{60}$  groups define the  $z_{bf}$  axis. The line connecting the Ph moieties of **6** and **7** defines their respective  $x_{bf}$  axes. The coarse grained representation of **8** has  $C_{\infty v}$  symmetry, therefore the  $x_{bf}$  and  $y_{bf}$  axes are degenerate.



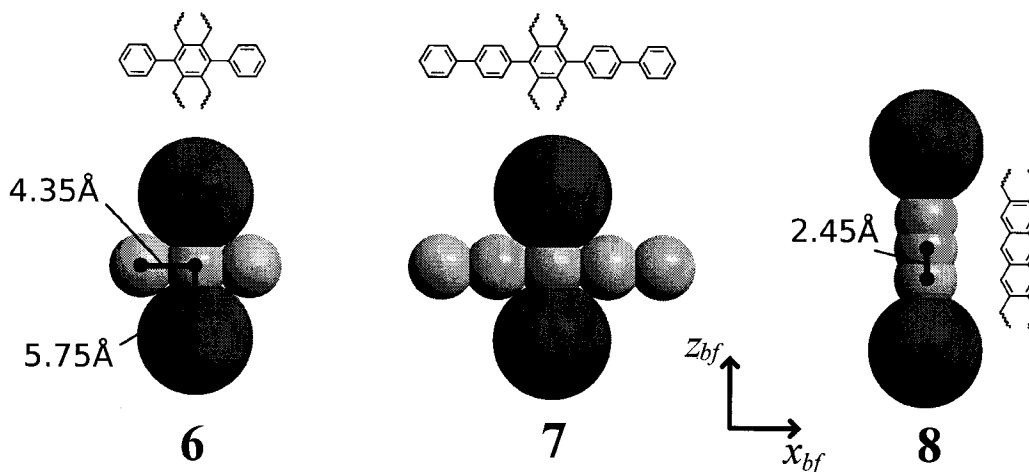


Figure IV-1. Cartoon drawings of the bis-fullerene molecules studied in this chapter. Molecules **6** and **7** have  $D_{2h}$  symmetry (in our simplified representation) and their bridging groups contain 3 and 5 phenyl (Ph) moieties, respectively. Molecule **8** has  $C_{3v}$  symmetry and its bridging group is an anthracene derivative represented with three Ph groups. The relevant molecular dimensions for all molecules are shown on **6** and **8**. The body-fixed coordinate system for the molecules is also included.

These specific molecules are chosen to explore how their simple differences in geometry affect self-assembled adlayer structures. The different length (Ph<sub>3</sub> and Ph<sub>5</sub>) bridging groups of molecules **6** and **7** are intended to test whether such protruding features will facilitate or frustrate self-assembly. The bridging group of **8** separates the two fullerene centers by 16.4Å, well beyond their preferred (center to center) vdW distance of 10.06Å. Forcing fullerenes this far apart is expected to disrupt hexagonal C<sub>60</sub> packing for lying-down configurations, but the resulting adlayer morphology for **8** is still not intuitively obvious.

We note that, to the best of our knowledge, these molecules have not been created. However, their synthesis is feasible using established fullerene synthetic

techniques [18]. Therefore our investigations of these molecules are purely predictive, and they yield a number of experimentally testable hypotheses.

## **2. The Coarse Grained Force Field**

The force field that defines the interactions between UA groups is largely unchanged from that used in the previous chapter. Two minor changes have been made in an effort to increase computational efficiency.

First, the surface atomic corrugation was switched off for  $C_{60}$ -Au(111) interactions after preliminary simulations showed it had little or no influence on adlayer patterning yet considerably increased computing time. As discussed in the previous chapter, the corrugation's only structural effect is to register solid adlayers in certain orientations relative to the surface because fullerenes strongly prefer 3-fold atomic sites. However, this strong preference hinders lateral diffusion because the corrugation peak to valley height (12.4 kcal/mol) forces fullerenes to pass over twofold sites (which still impose a barrier of 3.1 kcal/mol).

In contrast, lateral diffusion on the smooth surface is only restricted by the ruggedness of the intermolecular potential. With this simplification, 2D MC trial moves – x-y translations and rotations about the surface normal – become particularly efficient. This allows larger step sizes which result in more efficient exploration of configuration space.

An important implication of removing the corrugation is that the surface becomes a featureless attractive slab. Because there is no corrugation specific to one metal and one crystalline plane, the surface's attractive strength is its defining attribute. A surface defined this simply can therefore, in principle, represent a number of metal or

semiconductor surfaces. For the remainder of this study, the parameter  $E_{FG}$  gives the fullerene-surface attraction energy and we focus on values within range of possible  $C_{60}$ -Au(111) energies (20-60 kcal/mol). However, we stress that our results can also be interpreted for multiple surfaces with similar fullerene binding affinities.

The second change to the force field is to replace the Girifalco potential [88] for  $C_{60}$ - $C_{60}$  dispersion with a Morse potential. Both potentials are pairwise-additive and have identical well depths and equilibrium separations (6.4 kcal/mol and 10.06Å, respectively). The subtle difference lies in the stiffness of the potential energy function – a parameter equivalent to a spring constant near the minimum energy.

Fullerenes have a stiff interaction potential. They therefore aggregate like billiard balls and their clusters are unyielding to small conformational distortions. While the Girifalco pair potential reflects this stiffness, it likely overestimates its exact value. The Girifalco potential was parameterized to reproduce bulk  $C_{60}$  properties; However, there is experimental [157] and theoretical [158] evidence suggesting that fullerenes have a slightly softer interaction. Based on *ab initio* calculations, the PPR potential [159] was parameterized with a different functional form resulting in a slightly softer interaction. The PPR potential resolves some discrepancies between experiment and theory. Still, some remaining discrepancies suggests that the PPR potential may slightly overestimate the interaction stiffness [158,160,161].

Some more subtle points regarding fullerene interactions are also worth noting. The first is that at 269  $cm^{-1}$  (equivalently, 388K) and above, pristine and functionalized  $C_{60}$  have active breathing modes [162] which would likely soften the interaction further. Second, partial charge transfer takes place when a fullerene adsorbs to the Au(111) (and

other metals) substrate [112,25,163] and these partial charges on fullerenes should add a softening Coulombic term to their effective interaction potential. These subtle effects are beyond the scope of our studies and they cannot realistically be reproduced by our coarse grained representation. However, taking these considerations into account, we opt to replace Girifalco's potential with a Morse potential

$$U_M(r) = D\left(\left(1 - e^{-\rho(r-r_e)}\right)^2 - 1\right) \quad (\text{IV.1})$$

with a stiffness parameter of  $\rho=0.90\text{\AA}^{-1}$  (other parameters are defined in Chapter III). As a point of reference, the repulsive wall of the PPR potential [159] is that of a Morse potential with a stiffness of  $0.97\text{\AA}^{-1}$ .

Changing the  $C_{60}$ - $C_{60}$  potential in this manner affords a small increase in sampling efficiency because the fullerene moieties largely define the size and shape of the molecules. If they are softer and more deformable, they will squeeze through tight spaces more easily than if their interaction was more rigid. "Softening" this interaction allows molecules to reorganize more easily and improves computational efficiency. Since the interaction distance and energy parameters remain the same as the Girifalco potential, it should not change the resulting structures. (We note that for isolated clusters of spherical particles, including fullerenes, cluster morphologies are extremely sensitive to cluster size and interaction potential stiffness [164]. In this study, however, the molecule-molecule interaction anisotropy and the molecule-substrate interactions largely determine the resulting structure symmetries.)

### **3. T-REMC Simulation Approach**

With the force field established, Temperature Replica Exchange Monte Carlo (T-REMC, or simply REMC) simulations [151,152] are carried out to exhaustively study the

structural behavior of small,  $N=20$  molecule clusters. The goals are to thoroughly sample configuration space and in doing so to determine thermodynamically stable ordered (or disordered) solid structures. These REMC simulations are also used to probe temperature dependent phase behavior and the underlying free energy landscapes that drive spontaneous structure formation.

In the REMC method used here, each system replica advances through configuration space as a canonical NVT Metropolis Monte Carlo simulation with the standard trial moves (translations, rotations, etc.) as described in Section II.B.3. A bijective mapping assigns replicas to the fixed set of temperatures  $\{T_i, i=1, NR\}$  (sometimes called an ensemble or schedule), where  $NR$  is the number of replicas, and periodic exchange moves swap replicas between temperatures. Accordingly, we refer to this particular flavor of replica exchange as T-REMC.

For each replica, the simulation region is the square prism  $50 \text{ \AA}$  above a square surface slab in the x-y plane. The surface slab is made large enough to ensure uncrowded, sub-monolayer surface coverage for a cluster of  $N=20$  molecules. A harmonic restoring potential keeps the molecules within this region. Each replica is advanced using single-molecule trial moves of four possible types: 3D translation; rotation about a random axis passing through the molecule's center; 2D translation in the x-y plane; and rotation about the surface normal (passing through the molecule's center). The latter two move types can help sampling efficiency because molecules do not "bump into" the surface. During preliminary runs, step sizes for all move types and temperatures are adjusted to give approximately a 40% acceptance fraction. The step sizes are then fixed during equilibration and data collection. Defined as  $N$  trial moves, each MC cycle

attempts one move, on average, per molecule. Replicas are advanced 25 MC cycles and are then paused while exchanges are carried out. The probability of exchanging configurations between two replicas  $i$  and  $i'$  is calculated with the expression

$$\begin{aligned}
 p(i \rightarrow i', i' \rightarrow i) &= \min \left[ 1, \frac{p(U_i, \beta_{i'}) p(U_{i'}, \beta_i)}{p(U_i, \beta_i) p(U_{i'}, \beta_{i'})} \right] \\
 &= \min [1, \exp(-(\beta_i - \beta_{i'})(U_{i'} - U_i))]
 \end{aligned}
 \tag{IV.2}$$

where  $U_i$  is the total potential energy of replica  $i$ ,  $\beta \equiv (k_B T)^{-1}$ , and  $p(U_i, \beta)$  is the canonical probability of configuration  $i$  occurring at  $\beta$ . During exchange periods,  $2*NR$  exchanges are performed using Calvo's all-exchanges approach [165]. All simulations reported here use  $NR=32$  replicas.

The efficiency gains afforded by replica exchange depend upon how quickly replicas complete round trips between the temperature extremes. This is especially true of the cluster systems considered here, where thorough sampling of the low- $T$  configuration space requires repeated transitions from ordered to disordered states. In practice, bottlenecks that hinder replica migration are both common and difficult to predict *a priori*. Strategies to mitigate such bottlenecks are an area of much current research activity [165-168].

To identify the temperatures where bottlenecks occur, we carry out initial simulations using a naïve geometric temperature spacing (i.e.  $T_{i+1}=(a \text{ constant}) * T_i$ ). The most problematic temperature regions are usually signaled by a sharp decrease in the exchange acceptance fraction for adjacent replicas. To remedy this, exchanges are encouraged by locally decreasing temperature spacing. In accordance with (IV.2), closer spacing increases the overlap of the associated energy distributions and increases the

exchange probability. This  $U$  distribution overlap is illustrated in Figure IV-2 for an ensemble of 32 replicas.

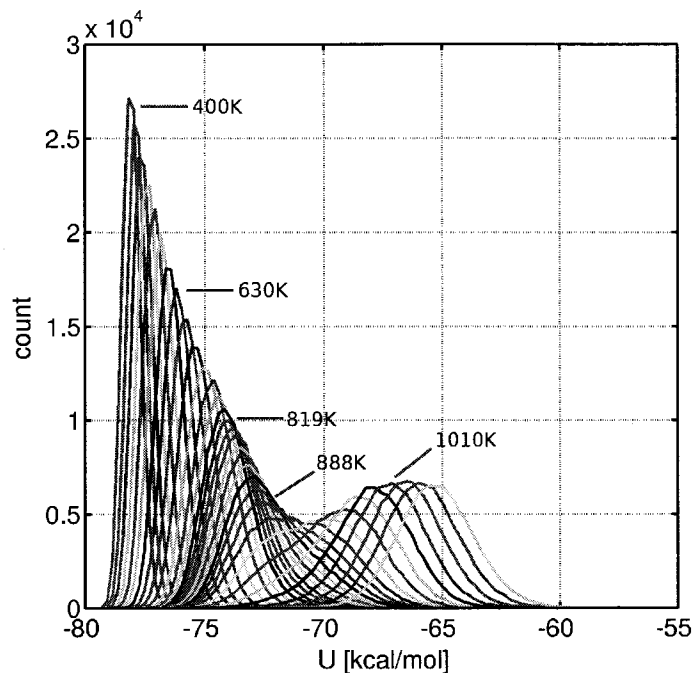


Figure IV-2. Distributions of  $U$  for each temperature in an equilibrated T-REMC system. Beginning at 400K, every eighth temperature is labeled.

This simulation/adjustment process is usually iterated a few times. As adjustments are made, the minimum temperature,  $T_{\min}$ , (i.e.  $T_l$ ) remains fixed at 400K. We chose the minimum temperature of 400K assuming that a self-assembled monolayer intended for electronic or photovoltaic applications should be thermodynamically stable in the solid state at this temperature (and at lower temperatures). However, the maximum,  $T_{\max}$ , ( $T_{NR}$ ) is adjusted to just above the cluster melting temperature. This keeps the temperature range as small as possible (for efficiency) while ensuring randomization and ergodic sampling at high temperatures. Following all of these adjustments, the temperature ensemble is then fixed throughout data collection runs.

With the established temperature ensemble and the associated set of (partially equilibrated) configurations, additional equilibration is performed until each replica has made at least one round trip between  $T_{\min}$  and  $T_{\max}$ . Data collection is then carried out until each replica has made, on average, two successive  $T_{\min}$  to  $T_{\max}$  round trips.

Throughout the data collection period, the total system energy  $U$  is computed as the sum of the following components:  $U_{HB}$ , the hydrogen bonding interactions between CA groups;  $U_{vdW}$ , all other pairwise intermolecular interactions; and  $U_{surf}$ , the UA-Au(111) surface energies. For biasing purposes, we also track  $U_{FG}$ , the total C<sub>60</sub>-Au(111) energy although it is a part of both  $U$  and  $U_{surf}$ . For all of these energies, ensemble averages are accumulated and divided by  $N$ , so they are on a per-molecule basis. Additionally, the heat capacity (per molecule) is calculated with the standard expression

$$C_v = N \frac{\langle U^2 \rangle - \langle U \rangle^2}{k_B T^2}, \quad (\text{IV.3})$$

where  $k_B$  is the Boltzmann constant and angular brackets denote ensemble averages.

#### **4. Order Parameters (reduced coordinates)**

During data collection, structural order parameters are calculated at regular intervals. Each order parameter is tasked with measuring some type of patterning. Additionally, each order parameter can serve as a “progress coordinate” for a structural transition between two stable states. (The general terms “progress coordinate” and “reduced coordinate” are used here because reaction coordinate implies chemical bond forming/breaking processes.) Probability statistics along a progress coordinate can then be used to plot a free energy profile or potential of mean force (PMF). The next section



(IV.B.5) details this procedure. Most of the following order parameters have been introduced previously in section III.D.2 (page 44) so they are briefly sketched here.

The order parameter  $C60ML$  is a count of fullerene moieties in the first monolayer, i.e. with centers no more than 6.1 Å above the substrate. The count is divided by  $N$ , thus for the bis-fullerenes considered here the upper limit  $C60ML=2$  implies that all molecules are lying flat.  $C60ML<2$  could result from multiple phenomena including completely desorbed molecules or molecules with both fullerenes in the second monolayer. These occurrences are rarely observed in the present study, though, and molecules typically have at least one  $C_{60}$  touching the substrate (i.e.  $C60ML>1$ ). Therefore  $C60ML$  is an indirect measure of lying-down molecules.

The parameter  $PhNN$  counts NN interactions between Ph groups using a cutoff distance of 7 Å and it is reported as the average per molecule. Large values of  $PhNN$  indicate that bridging groups interdigitate and are close together while low values occur when bridging groups are spaced apart.

The order parameters  $\chi_6^2$  and  $\chi_4^2$  are used to measure 2D hexagonal and square packing [125] of fullerenes in the first monolayer (as defined above). Within this monolayer, all  $C_{60}$  NN bonds,  $\mathbf{r}_{jk'}$ , shorter than 13 Å are used to calculate

$$\chi_4^2 = \left\langle \left| e^{i4\Phi_{jk'}} \right| \right\rangle^2 \quad (\text{IV.4})$$

and

$$\chi_6^2 = \left\langle \left| e^{i6\Phi_{jk'}} \right| \right\rangle^2 \quad (\text{IV.5})$$

where  $\Phi_{jk}$  is the angle between the global x-axis and the projection of  $\mathbf{r}_{jk}$  on the x-y (surface) plane and  $i$  is the imaginary unit (otherwise, ‘ $i$ ’ is a configuration index). These parameters take values between zero, for disordered structures, and unity, for crystalline hexagonal or square packed structures, respectively.

To measure orientational ordering, we use three order parameters which are based on  $P_2$ , the second Legendre Polynomial.  $P_2$  can gauge parallel alignment between two vectors using their intersection angle,  $\psi$ , and it is written as

$$P_2(\psi) = \frac{3 \cos^2(\psi) - 1}{2}. \quad (\text{IV.6})$$

Possible  $P_2$  values range from -1/2, for perpendicular vectors, to unity, for parallel vectors, and its spherical (isotropic) average is zero. The  $P_2$  formalism is flexible and it can be used to compare a molecule’s orientation to a stationary reference or to compare a pair of neighboring molecules’ orientations.

First, we define the order parameter  $P_{2i}$  to measure “tilting” of a molecule’s body fixed z-axis,  $\mathbf{z}_{bf,j}$ , (recall that this axis passes through both fullerenes) relative to the surface normal,  $\mathbf{z}$ , using the expression

$$P_{2i}(\mathbf{z}_{bf,j}) = \frac{3(\mathbf{z}_{bf,j} \cdot \mathbf{z})^2 - 1}{2}, \quad (\text{IV.7})$$

where the subscript  $j$  indicates a specific molecule and the (unit) vector dot product replaces the cosine term of (IV.6). Reported values of  $P_{2i}$  are configuration averages over all molecules  $j$ .

The second orientational order parameter  $P_{2z}(\mathbf{z}_{bf,j}, \mathbf{z}_{bf,k})$  measures alignment between the body fixed z-axes of neighboring molecules  $j$  and  $k$ . It is expressed as

$$P_{2z}(\mathbf{z}_{bf,j}, \mathbf{z}_{bf,k}) = \frac{3(\mathbf{z}_{bf,j} \cdot \mathbf{z}_{bf,k})^2 - 1}{2}, \quad (\text{IV.8})$$

where the  $\mathbf{z}$  vectors are of unit length. Reported values of  $P_{2z}$  are configuration averages over all molecule pairs with centers within 20Å. Finally, the third orientational order parameter  $P_{2x}$  is functionally identical to  $P_{2z}$ , but with body fixed x-axes as arguments.

It is worth noting that the parameters *C60ML*,  $P_{2t}$ , and  $P_{2z}$  can measure similar behavior in limiting cases, but, in general, they are not redundant. For example, a configuration of perfectly upright molecules with  $P_{2t} = 1$  requires that  $P_{2z} = 1$ , but the converse is not generally true.

## **5. Histogram Reweighting, Sampling Strategies, and Free Energy Surfaces**

The main purpose of these simulations is to characterize each system's free energy landscape: the free energy minima, the transition paths between minima, and the corresponding structures for each. To accomplish this, extensive T-REMC calculations are carried out to explore configuration space and to collect statistical distributions of the order parameters outlined above. This section describes how the collected statistics are used to compute features of the free energy landscape. Also described are the histogram reweighting methods for combining multiple biased datasets.

### **(a) Potentials of Mean Force (PMFs)**

The simplest characterization of a free energy landscape is a 1D profile along a reduced coordinate  $\xi$ . With sufficient sampling, a probability density function (PDF)  $p(\xi)$

can be constructed. From this, the potential of mean force (PMF) is determined by the relation

$$A(\xi) = A_0 - k_B T \ln(p(\xi)). \quad (\text{IV.9})$$

Here the Helmholtz energy,  $A$ , is used due to the constant volume simulation conditions. The additive constant  $A_0$  relates calculated values to a reference state. Here, however, its value is inconsequential because we only consider relative values of  $A$ . As a result,  $p(\xi)$  need not be normalized and we freely choose  $A_0$  so the minimum of  $A(\xi)$  is zero. The procedure just described and equation (IV.9) are easily extended to multiple dimensions, each with a corresponding reduced coordinate. A two-coordinate approach yields a topographic PMF. (Two notes on semantics: First, a PMF is also sometimes called the Landau Free Energy [83]. Second, we use PMF to refer to a computed potential of mean force which is a one or two dimensional representation of the actual many-dimensional free energy surface)

For a PMF to be visualized as a topographic surface, it is limited to two reduced coordinates. To ensure the best accuracy, however, these two reduced coordinates should be carefully chosen. Here some of the typical considerations are discussed. Consider a bistable free energy landscape. A good order parameter should clearly distinguish the two free energy funnels so that intermediate values correspond to transitional structures. It is precisely these improbable structures (and the corresponding local minimum in the PDF) that determine the free energy barrier height. However, distant regions of configuration space necessarily become superimposed when using two reduced coordinates. Thus there is no guarantee that a chosen order parameter will sharply distinguish separate funnel regions. A poorly chosen order parameter will partially superimpose the two regions,

suggesting an incorrectly small free energy barrier. These pitfalls are exacerbated in systems with more complex free energy landscapes.

In practice, this means that some preliminary knowledge of the free energy landscape is necessary to choose suitable order parameters. Therefore it is beneficial to track a number of candidate order parameters during a simulation (or to store the entire simulation trajectory) for subsequent analysis.

(b) Enhanced Sampling and Histogram Reweighting

In addition to the importance of choosing good order parameters, thorough sampling of configuration space is equally important to ensure accurate PMFs. Up to this point in the discussion of PMF calculations, the tacit assumption has been that the underlying statistical sampling was robust. In fact, to get the best sampling for our computational expenditure, we use two techniques, temperature replica exchange (introduced in Section 3 of this Chapter) and force field biasing.

Temperature replica exchange is a widely applicable method for enhancing sampling in atomistic simulations. For the clusters of bis-fullerenes studied here, the low temperature structures (low being 400-600K) are frozen solids that are restricted to their immediate surroundings in configuration space. Were a replica fixed at 400K, its configuration would be effectively stuck and crystalline defects could be preserved for the entire simulation. Furthermore, barriers to regions with equal free energy, but dissimilar structures, would never be crossed on practical simulation timescales. The resulting 400K PMFs would be incomplete and inaccurate. Such a brute force approach is impractical.

By giving such solid structures the ability to gain and lose thermal energy, temperature replica exchange can more efficiently sample the low energy configurations. Furthermore, in addition to improving the low-T sampling, data from higher temperatures can be adjusted and incorporated into the PMF for a temperature of interest,  $T^o$ , by using the temperature weighted histogram analysis method (T-WHAM) [156]. The underlying premise of WHAM (T-WHAM's generalizable parent method, a workhorse of modern statistical mechanics) is that multiple histograms can be combined by using an iterative rescaling process to minimize the differences between overlapping regions [155]. This method is sketched here.

Consider a set of histograms  $\{n_{i,a}\}$  where  $n$  is the count in bin  $a$  of histogram  $i$ . Here a single bin index,  $a$ , is used to keep our notation compact, but in practice the histograms have two or more dimensions. When normalized, these histograms become (discretized) probability density functions (PDFs)  $\{p_{i,a}\}$ . The WHAM approach presupposes that the desired (or so called, reference) PDF  $\{p_a^o\}$  differs from each input PDF  $p_{i,a}$  by two multipliers. Specifically,

$$p_{i,a} = f_i c_{i,a} p_a^o \quad (\text{IV.10})$$

where  $f_i$  is an unknown scaling factor. The constant  $c_{i,a}$  terms are bin dependent and account for biasing. Therefore  $p_{i,a}$  and  $c_{i,a}$  are known and the other two terms are to be solved for. In T-WHAM, the potential energy  $U$  is the biasing coordinate and temperature (or inverse temperature  $\beta \equiv (k_B T)^{-1}$ ) is effectively the biasing strength. The scaling coefficients to account for the biasing effect are

$$c_{i,a} = \exp[-(\beta_i - \beta^o)U_a] \quad (\text{IV.11})$$

where  $\beta_i$  and  $\beta^o$  are the inverse temperatures of the  $i^{\text{th}}$  and reference histograms, respectively, and  $U_a$  is the potential energy of bin  $a$ .

After performing an iterative procedure to determine all  $\{p_a^o\}$  and  $\{f_i\}$ , the new PDF  $\{p_a^o\}$  incorporates, to some extent, data from all of the input histograms. Typically this resulting PDF is summed along the  $U$  dimension since  $U$  is of little interest as a reduced coordinate for PMFs. With  $\{p_a^o\}$  summed to the desired two dimensions, PMFs are then calculated as was previously described using (IV.9).

After initial simulations for the present study were analyzed, it became evident that some important regions of configuration space were being under-sampled, or missed entirely during the course of T-REMC runs. In particular, coexistence and interconversion between standing up and lying down structures was not observed. To address this, the second way we improve sampling is by using force field biasing to target specific structure types. Specifically, we scale the  $C_{60}$ -substrate energy,  $E_{FG}$ .

This scaling (biasing) alters the stability of standing up versus lying down configurations, thereby allowing us to target both structure types. An important feature of this approach is that not all  $E_{FG}$  values need to be simulated. As long as the individual simulations characterize all of the relevant structure regions, their statistics can be combined and rescaled to any (reasonable)  $E_{FG}$  value. That is, if separate simulations with  $E_{FG}$  values of 25, 30 and 35 kcal/mol were performed, the data could be combined and reweighted to any  $E_{FG}$  value in the range of 25-35 kcal/mol.

Data from separate biased runs is readily incorporated into the previously described T-WHAM framework. The resulting statistics reflect the sampling advantages of using multiple temperatures and multiple Hamiltonians (although the Hamiltonian is

fixed here for each T-REMC simulation, combined Hamiltonian and temperature exchange could be a promising extension of this work). To account for the  $E_{FG}$  biasing, the WHAM histograms require an extra dimension for the biasing coordinate  $U_{FG}$  (the total fullerene-substrate potential energy) and the modified weighting coefficients

$$c_{i,(a,b)} = \exp[-(\beta_i - \beta^o)U_a] \exp[-\beta_i w_i(U_{FG,b})] \quad (0.12)$$

are necessary. Here the subscript  $b$  denotes the bin index along the biasing coordinate  $U_{FG}$ . The weighting function  $w_i(U_{FG})$  can have any form but here it is simply a scalar multiple of the energy (coordinate)  $U_{FG}$ . This can be envisioned as a constant force “pulling” configurations towards lower values of  $U_{FG}$ .

## **C. Results**

### **1. Molecule 6**

#### **(a) Individual T-REMC simulations of Molecule 6**

T-REMC simulations of **6** were carried out for  $E_{FG}$  values of 25.5, 26.6, and 28.9 kcal/mol. These simulations identified one standing-up structure and two distinct lying-down motifs. Here the results of the individual T-REMC simulations are discussed and the structures are introduced.

##### **(a).i. $E_{FG} = 25.5$ and $26.6$ kcal/mol: Standing-Up Structures**

For both  $E_{FG}$  values 25.5 kcal/mol and 26.6 kcal/mol, a broad first order melting transition occurs at approximately 900-950K. (For both  $E_{FG}$  values, the results were qualitatively identical and only differed in the exact location of the transition) This transition is evidenced by a clear feature in the heat capacity shown in Figure IV-3. At



the transition temperature, the order parameter averages also shift, signaling the order to disorder transition.

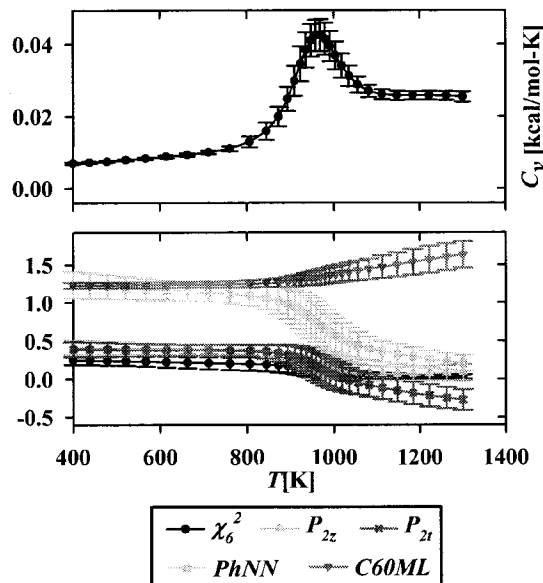


Figure IV-3. The heat capacity (upper panel) and ensemble averaged order parameters (lower panel) for molecule **6** all as a function of  $T$ . Here  $E_{FG}=25.5$  kcal/mol and  $PhNN$  is scaled by  $1/4$ .

The low temperature ordered structures are characterized by a standing-up “core” of molecules (standing perpendicular to the surface) that is surrounded by flat-lying and tilted molecules. (See Figure IV-4) In the core region, a planar layer of  $(Ph)_3$  bridging groups separates two parallel close packed  $C_{60}$  layers. To achieve this compact structure and to avoid steric repulsion, the  $(Ph)_3$  bridging groups adopt a herringbone pattern. This herringbone pattern is clearly visible when the upper layer of  $C_{60}$  moieties and the disordered perimeter molecules are removed in Figure IV-4(b).

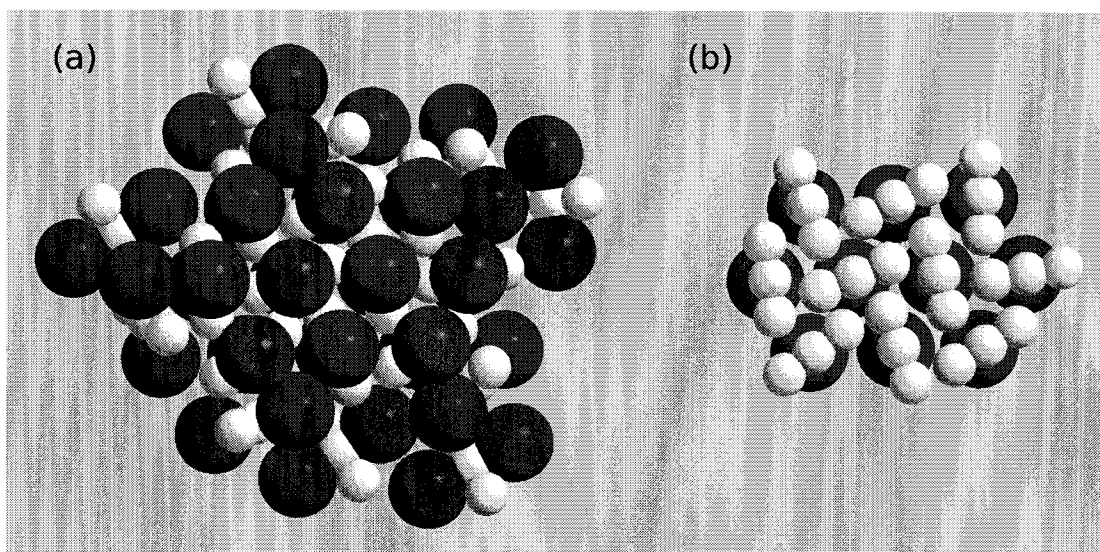


Figure IV-4. A configuration snapshot for molecule **6** taken at 400K with  $E_{FG}=25.5$  kcal/mol. In panel (a), the complete configuration is shown and molecules in the standing up 'core' have fullerenes colored red. In panel (b), perimeter molecules are not shown and the upper fullerenes are removed to illustrate the herringbone ordering of  $(Ph)_3$  bridging groups.

The patterning seen in Figure IV-4 is reflected by the 400K ensemble averaged order parameters in Figure IV-3. The  $\chi_6^2$  order parameter signals the hexagonal  $C_{60}$  monolayer packing; however its average is near 0.25, not unity, due to the inclusion of disordered edge molecules in the average. Similarly, the order parameters  $P_{2t}$  and  $P_{2z}$  average approximately 0.4 because the contributions from vertical core molecules are averaged with those from the unaligned perimeter molecules. The standing-up core is also evidenced by the  $C60ML$  parameter averages of 1.1-1.2 which indicate that most molecules only have a single  $C_{60}$  adsorbed to the surface. Lastly, the large value of  $PhNN$  (approximately 5.0, in Figure IV-3  $PhNN$  is scaled by  $1/4$ ) occurs because of the dense herringbone packing of  $(Ph)_3$  bridging groups belonging to upright molecules.

The disordered perimeter molecules contribute substantially to configuration averages because the system only contain  $N=20$  molecules. These edge effects can be

rationalized, informally, by noting that the perimeter molecules adopt intermediate tilt angles that give the cluster a granular “curvature” at the edges as is seen for macroscopic surface wetting. A larger cluster could support a higher fraction of ordered, standing-up molecules and the disordered perimeter molecules would contribute less to the configuration averaged order parameters.

(a).ii.  $E_{FG} = 28.9$  kcal/mol: Lying-down structures.

In T-REMC simulations of molecule **6** with  $E_{FG}$  increased to 28.9 kcal/mol, a standing-up phase is not observed because the strong  $C_{60}$ -surface attraction keeps fullerenes adsorbed on the substrate. With all molecules held to the surface, lateral  $C_{60}$  aggregation is the dominant ordering force. However, the protruding Ph groups prevent complete hexagonal  $C_{60}$  coordination. Two distinct lying-down structure motifs, pictured in Figure IV-5, are observed. Next, these two structures are described, and then the system’s temperature dependent behavior (Figure IV-6) is discussed.

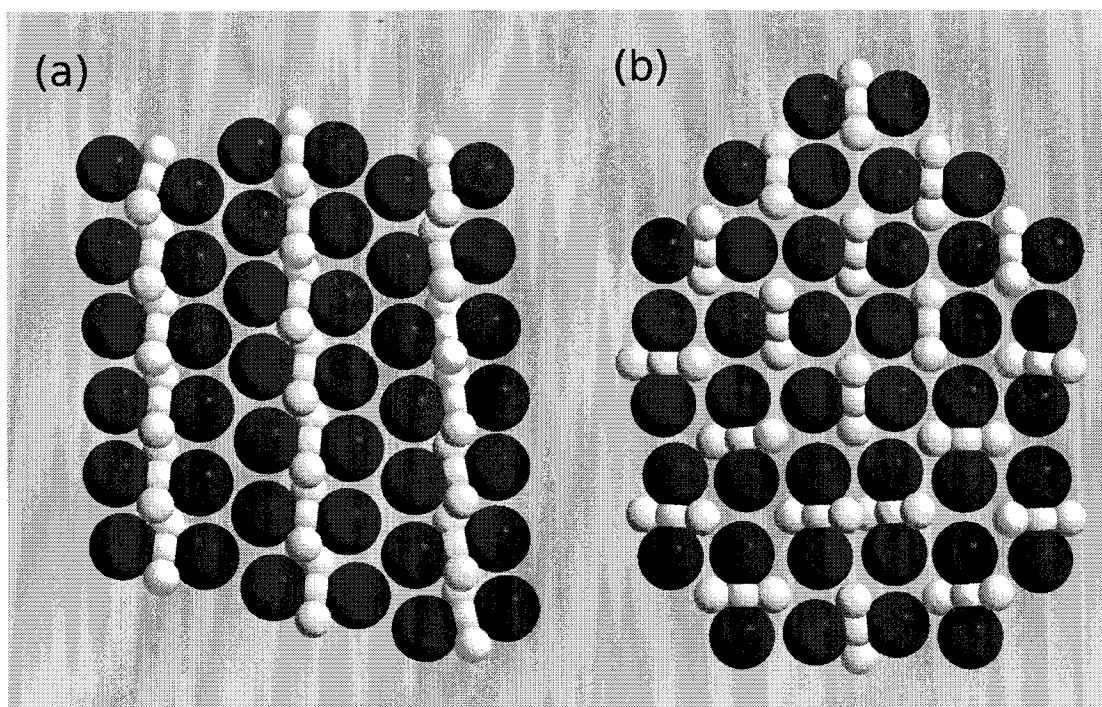


Figure IV-5. Configuration snapshots of molecule **6** when  $E_{FG}=28.9$  kcal/mol. The 'compact' motif (a) was observed at 400K and the square configuration (b) was seen at 567K.

In the first of the two observed lying-down structures, (shown in Figure IV-5(a)) molecules achieve a dense packing (we refer to it as the “compact” lying-down phase). This compact structure is possible because each molecule tilts like a see-saw to raise and lower its opposite Ph groups thereby creating space for a neighbor molecule’s Ph group. By allowing the Ph groups to stack in this manner, two neighboring molecules can achieve two  $C_{60}$  NN contacts. This pattern readily extends to form 1D rows in which all molecules have identical orientations. Two of these rows can then zip together via zigzag  $C_{60}$  contacts. Crucially, in this motif each fully coordinated  $C_{60}$  has four  $C_{60}$  NN, while in the alternative square motif (Figure IV-5(b)) each  $C_{60}$  only has three  $C_{60}$  NN. Because all molecules in the compact motif have nearly identical orientations, the order parameters

$P_{2z}$  and  $P_{2x}$  take values near unity. However,  $\chi_6^2$  and  $\chi_4^2$  are both near zero because the  $C_{60}$ s have neither hexagonal nor square ordering.

In the second flat-lying motif (see Figure IV-5(b)) the  $C_{60}$ s form a less compact square network whose interstitial spaces accommodate the protruding Ph moieties. This ordering results in an extended, square  $C_{60}$  superlattice which is well characterized by  $\chi_4^2$ . Neighboring molecules' z-axes generally parallel each other. However, perpendicular orientations are frequently observed and only introduce a small localized distortion to the square  $C_{60}$  superlattice. The competition between the parallel and perpendicular motifs appears to be subtle since the coordination environment of each molecule is nearly identical in both cases. Factors not considered here such as substrate templating effects or the atomistic interactions of Ph and  $C_{60}$  groups could potentially favor one structure or the other.

The order parameter that best distinguishes the compact structure from the square motif is  $PhNN$  which takes values near 0.25 for the latter and 3.5 for the former.

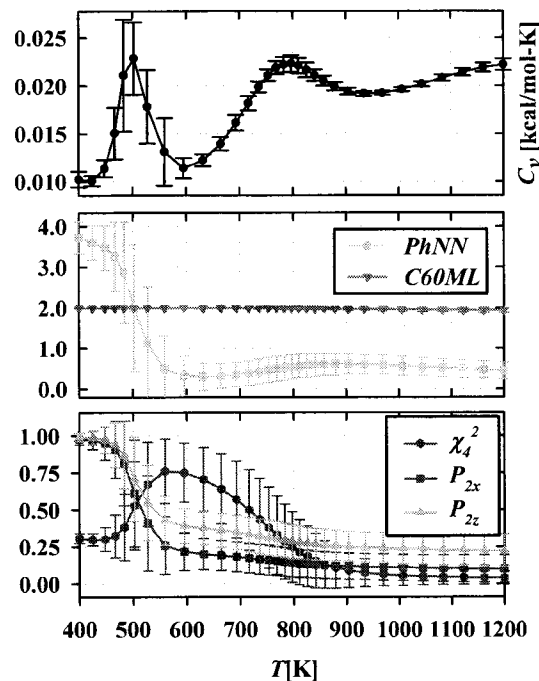


Figure IV-6. The heat capacity (upper panel) and ensemble averaged order parameters (middle and lower panel) for molecule **6** all as a function of  $T$ . Here  $E_{FG}=28.9$  kcal/mol.

Due to competition between these lying-down structures, the temperature dependent behavior of this system presents an interesting situation. Figure IV-6 shows the thermal averages of the order parameters just discussed as well as the heat capacity. At approximately 800K, a gradual phase transition occurs between the disordered liquid-like phase and the square solid phase. The heat capacity shows a broad maximum at this temperature and changes in the associated (ensemble averaged) order parameters  $\chi_4^2$  and  $PhNN$  signal the onset of square ordering.

A solid-solid phase transition occurs at 500K. This transition is evidenced by a prominent peak in the heat capacity as well as abrupt changes in the associated order parameters  $PhNN$ ,  $P_{2z}$  and  $P_{2x}$ . The structural differences are also clearly visible in configuration snapshots above and below 500K (Figure IV-5, (a) and (b)).

The compact structure's stability below 500K is a result of higher  $C_{60}$  coordination and to a lesser extent the additional Ph-Ph interactions. Above 500K, however, the square structure is most likely preferred due to a favorable entropic contribution to its free energy.

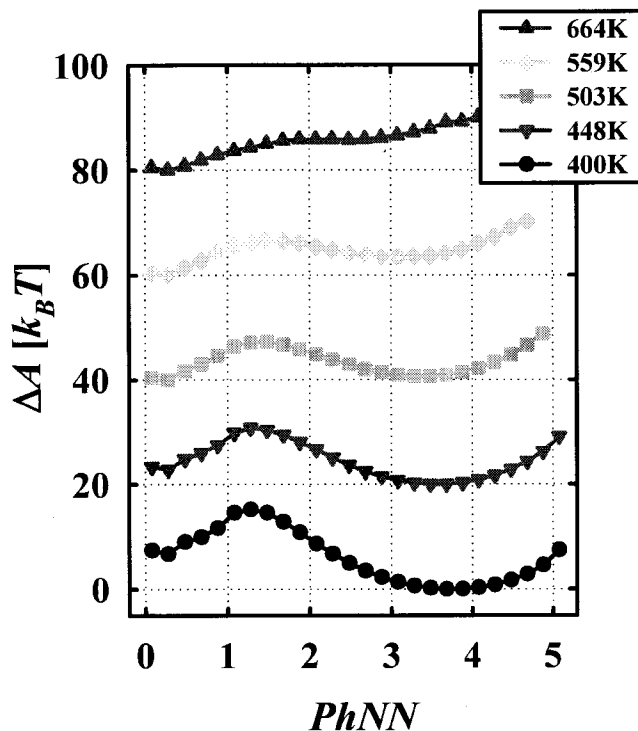


Figure IV-7. PMF profiles for molecule **6** as a function of  $PhNN$  at various  $T$ .  $E_{FG}=28.9$  kcal/mol. Low values of  $PhNN$  correspond to the square motif and large values correspond to the compact motif.

To further explore the competition between these two states we consider 1D PMFs for temperatures in the range 400K-664K. These 1D PMFs, shown in Figure IV-7, are calculated using equation (IV.9), with  $PhNN$  serving as the progress coordinate. The 664K PMF shows that the square motif (corresponding to low values of  $PhNN$ ) is the only stable structure and the free energy gradient guides the system towards it. Upon cooling to 559K, the square structure remains the ground state, however a metastable

minimum corresponding to the compact motif emerges for large PhNN. At 503K, the two states have the same free energy (recall that 500K was the solid-solid phase transition temperature), but are separated by a  $6.7 k_B T$  barrier. Below this temperature, the compact motif becomes the thermodynamic ground state and the square structure is metastable.

Figure IV-7 reveals that at all of the temperatures considered, a square structure must cross a barrier of at least  $6.7 k_B T$  to reach the compact structure region. This indicates that the square region can kinetically trap configurations and hinder formation of the compact ground state motif. Indeed, it was only after a considerable equilibration period that the compact motif was first observed in our simulations. Following additional simulation time it emerged as the thermodynamic ground state for temperatures below 500K.

#### (b) Free Energy Landscapes and Combined Results for Molecule 6

Using fixed values of  $E_{FG}$ , the individual T-REMC runs have identified distinct standing-up and lying-down structures, but give no indication of coexistence or equilibrium between them. One possible explanation is that no such equilibrium exists, and only the observed structures are thermodynamically stable. An alternative possibility is that both states are stable but are separated by a large free energy barrier that is not crossed during any individual simulation.

In principle, longer simulations would eventually explore both regions, but extending these simulations while just waiting for the barrier crossings to occur is wasteful. A much more efficient way to assess the relative stability is by combining the data from the individual simulations using histogram reweighting. This approach exploits the fact that the separate simulations explore partially overlapping regions of



configuration space and combined simulation data can provide a complete survey of both structure regions. Histogram reweighting was thoroughly discussed in section IV.B.5.

With this method, it is possible to compare all of the features that characterize the free energy landscape for given  $T$  and  $E_{FG}$ . In Figure IV-8 we present a 2D PMF for molecule **6** with  $T=400\text{K}$  and  $E_{FG}=28.9$  kcal/mol. The *C60ML* reduced coordinate is used to distinguish standing-up from lying-down structures. The second coordinate is the difference of two order parameters,  $PhNN-\chi_4^2$ . It distinguishes the lying-down compact and square structures better than either parameter does individually. The PMF shows three distinct minima: the lying-down, compact ground state ( $0 k_B T$ ); the lying-down square structure ( $4.3 k_B T$ ); and the standing-up hexagonal structure ( $7.2 k_B T$ ). The free energy barriers separating these regions are also indicated.

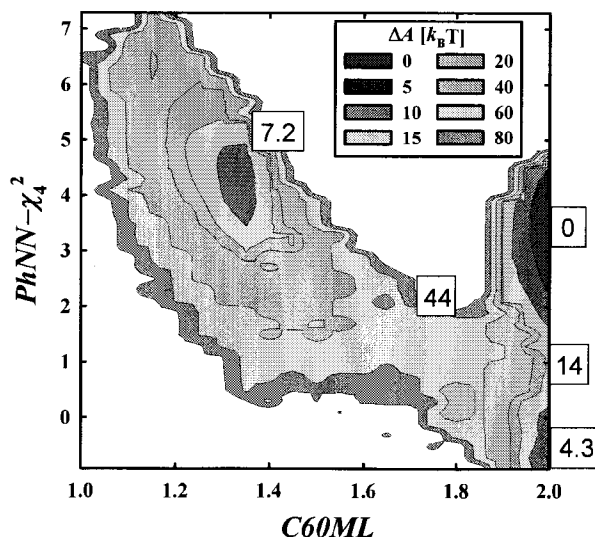


Figure IV-8. A 2D PMF for Molecule **6** at 400K with  $E_{FG}=28.9$  kcal/mol.  $\Delta A$  values are given for the minima and for the barriers separating them.

In the next two subsections we consider how different  $E_{FG}$  values and different temperatures alter the free energy landscape of the system.

(b).i.  $E_{FG}$  Dependence of the Free Energy Landscape

With temperature held constant at 400K, increasing  $E_{FG}$  has the expected effect of stabilizing lying-down structures and destabilizing standing-up configurations. For simplicity, we consider their relative stability using only the  $C60ML$  order parameter, which does a good job distinguishing standing-up and lying-down regions, but it clearly cannot tell the two lying-down motifs apart.

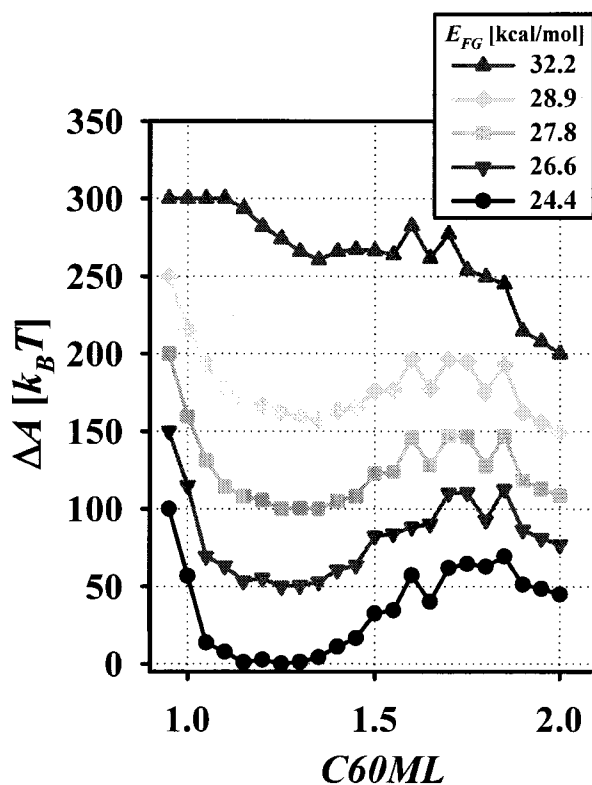


Figure IV-9. PMFs along the  $C60ML$  coordinate for molecule 6.  $T=400K$  is fixed and  $E_{FG}$  is varied between 24.4 and 32.1 kcal/mol.

In Figure IV-9, 1D PMFs along the coordinate  $C60ML$  show that large free energy barriers of  $\sim 40 k_B T$  or more separate the ground state from the metastable minimum. A critical value of  $E_{FG}$  exists between 27.8 and 28.9 kcal/mol, where both solid structures have the same free energy. Above or below this critical value, one structure is the ground state and the other is metastable.

Perhaps surprisingly, these deep metastable wells did not kinetically trap configurations during the T-REMC simulations. This suggests that at temperatures near phase transitions, the free energy gradients steer configurations towards the correct crystalline structure. Accordingly, we consider the temperature dependent behavior next.

(b).ii. Temperature Dependence of the Free Energy Landscape

To study the effects of temperature, we focus on three  $E_{FG}$  values: 25.5, 27.8, and 32.2 kcal/mol. For each value, PMFs along the *C60ML* coordinate are plotted for temperatures 400-800K in Figure IV-10. The low and high  $E_{FG}$  values strongly favor standing-up and lying-down structures, respectively, and the middle value is close to the critical value where they are equally stable. At 400K, a prominent barrier separates the two structure regions for all three  $E_{FG}$  values. The profile is quite jagged for intermediate structures, suggesting that our simulations did not exhaustively sample all of the relevant transition paths.

In Figure IV-10 panels (a) and (c), corresponding to the low and high  $E_{FG}$  values respectively, the temperature dependent behavior of the PMF profile is qualitatively the same, but with different ground states. In both cases, as temperature increases from 400K, the barrier between the two stable regions becomes smaller and less jagged until, at about 700K, a steady downhill slope leads to the ground state structure. Equivalently, upon cooling from high  $T$  the free energy gradients guide the systems to the correct structure and metastable states only emerge at low- $T$  when the correct structure has already been formed.

The intermediate  $E_{FG}$  value, 27.8 kcal/mol, does not strongly favor one structure or the other. This can be seen in Figure IV-10(b). At 800K, the lying-flat structure (with

$C60ML=2$ ) is the ground state. Relative to this, the transition barrier is at  $5.2 k_B T$ , and the metastable standing-up structure is at  $1.8 k_B T$ . Cooled to 700K, the trend is reversed and the standing-up phase ( $C60ML \sim 1.3$ ) becomes the ground state. Upon cooling to 400K, the double well profile deepens. We note that our actual T-REMC simulations (at 26.6 and 28.9 kcal/mol) fell to either side of this critical  $E_{FG}$  value. Supplementary T-REMC simulations with  $E_{FG}=27.8$  kcal/mol could potentially improve sampling of transitional structures.

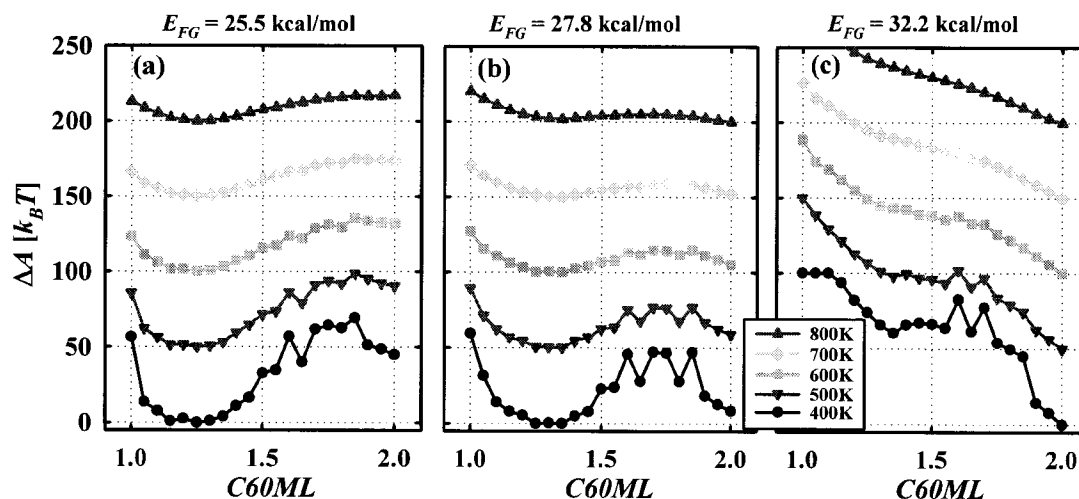


Figure IV-10. PMF profiles for molecule 6 at 400K - 800K for  $E_{FG}$  values of 25.5 kcal/mol (a), 27.8 kcal/mol (b), and 32.2 kcal/mol (c). The ordinate axis ( $\Delta A$ ) scale indicated on the far left applies to all three panels.

### (c) Summary and Implications for Self-Assembly

Self-assembling motifs with standing-up and lying-down morphologies were found to depend primarily on the fullerene-substrate attraction energy,  $E_{FG}$ . We identified two distinct lying-down morphologies whose relative stability depends on temperature. For weak and strong  $E_{FG}$ , the free energy landscapes effectively guided systems to the ground state structures as temperature was lowered. At low temperature (400-500K)

metastable states emerged, but they did not impose kinetic traps. At intermediate  $E_{FG}$ , the system's free energy landscape is bistable, and the large barrier between the two ordered states could prevent spontaneous self-assembly to a single target structure.

## **2. Molecule 7**

### **(a) Individual T-REMC simulations of Molecule 7**

T-REMC simulations of molecule 7 were carried out for  $E_{FG}$  values of 26.6, 28.9, and 33.3 kcal/mol. Solid structures identified in these simulations included amorphous aggregates and an ordered, lying-down structure.

#### **(a).i. $E_{FG}=26.6$ and $28.9$ kcal/mol: Amorphous Aggregates**

For the two lowest  $E_{FG}$  values, 26.6 and 28.9 kcal/mol, the results of T-REMC simulations were qualitatively the same. The only notable difference was the temperature range of the melting transition. We discuss only the  $E_{FG} = 26.6$  kcal/mol results in detail here.

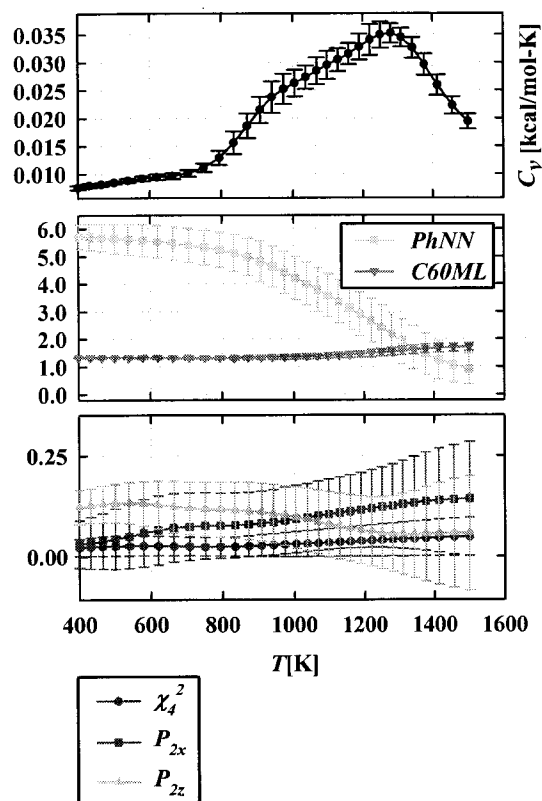


Figure IV-11. Heat capacity,  $C_v$ , and order parameter averages for Molecule 7 with  $E_{FG}=26.6$  kcal/mol. Note that the ordinate scale in the lower panel is shortened relative to previous figures

Thermal averages and the heat capacity for this system (shown in Figure IV-11) indicate that a gradual freezing transition forms a solid structure with little orientational or spatial ordering. (An example structure is shown in Figure IV-12) At 400K, the  $C60ML$  value of 1.4 and the  $P_{2z}$  average just above zero suggest that structures have some standing-up character and the  $PhNN$  average near 6 reflects the interdigitation of  $(Ph)_5$  bridging groups. While increasing  $T$  through the broad melting transition from 900-1500K, (visible in the heat capacity) the decreases in  $PhNN$  and  $P_{2z}$  indicate, respectively, that molecules spread apart and tilt to parallel the surface. Consistent with this structural change,  $C60ML$  increases towards limiting value of 2.0 at high  $T$ .

A typical 400K solid configuration is shown in Figure IV-12. The structure does not show any localized or extended patterning. Localized  $C_{60}$  aggregation is evident but the large  $(Ph)_5$  bridging groups obstruct extended hexagonal ordering. Although most of the molecules have one  $C_{60}$  free from the surface, they tilt and twist randomly to accommodate their protruding  $(Ph)_5$  bridging groups.

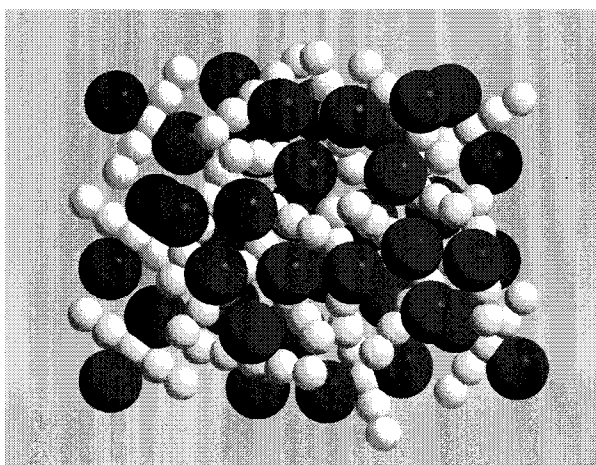


Figure IV-12. A configuration snapshot at  $T=400K$  for molecule 7.  $E_{FG}=26.6$  kcal/mol. Fullerenes not touching the substrate are colored red.

This situation is reminiscent of the glassy, disordered aggregates seen in Chapter III for simulations of molecule 3. In both cases, the bulky  $(Ph)_5$  substituents prevent extended hexagonal  $C_{60}$  packing. But the dominant intermolecular interaction,  $C_{60}$ - $C_{60}$  attraction, drives the formation of disordered aggregates. In these disordered structures, it is also likely that favorable entropic contributions to the free energy result from  $(Ph)_5$  arms randomly filling the available interstitial spaces.

(a).ii.  $E_{FG}=33.3$  kcal/mol: Lying-Down Structures

At larger values of  $E_{FG}$ , it is energetically favorable for both fullerenes to adsorb, allowing formation of ordered structures. The T-REMC simulation results for  $E_{FG}=33.3$  kcal/mol are discussed next.

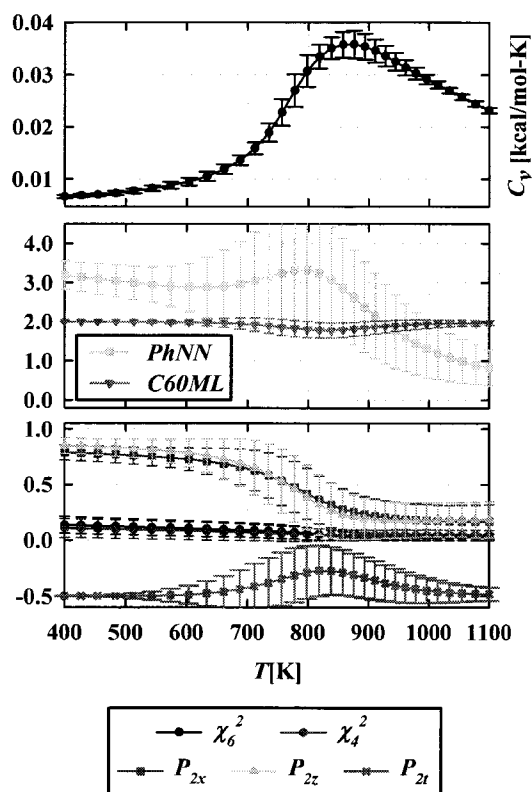


Figure IV-13. Thermal averages of the heat capacity and order parameters for molecule 7. Upper panel: heat capacity,  $C_v$ . Middle panel:  $PhNN$  and  $C60ML$ . Lower panel:  $\chi_4^2$ ,  $\chi_6^2$ ,  $P_{2x}$ ,  $P_{2z}$ , and  $P_{2t}$ ,

Figure IV-13 shows the thermal averages for heat capacity and the structural order parameters. Between 800 and 900K, the system undergoes a broad melting transition that is signaled by the maximum in the heat capacity and changes in many of the order parameters. In Figure IV-14, two snapshots, taken at 513K and 543K, show the characteristic patterning of the solid phase structures. During the freezing transition, there are simultaneous increases in the order parameters  $PhNN$ ,  $P_{2z}$ , and  $P_{2x}$ . These changes



suggest, respectively, that  $(\text{Ph})_5$  bridging groups form contacts and that molecules adopt similar orientations.

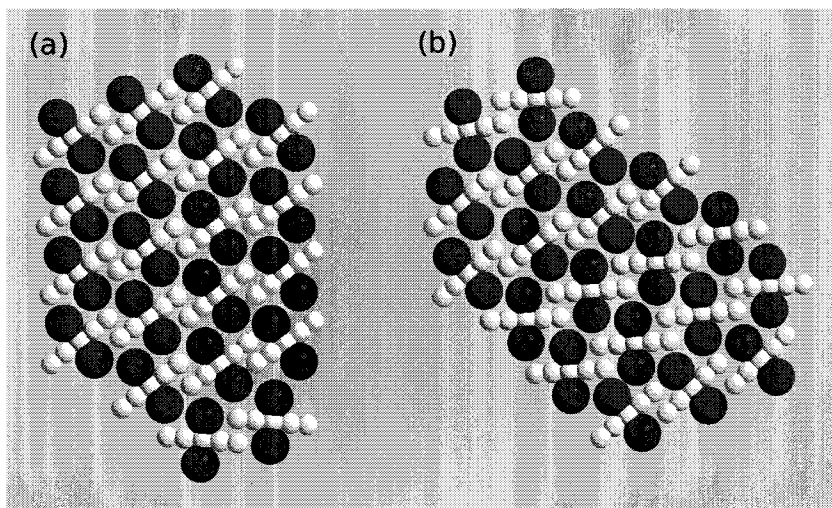


Figure IV-14. Configuration snapshots of molecule 7 at 513K (a) and 543K (b).  $E_{FG}=33.3$  kcal/mol.

This patterning is evident in the configuration snapshots of Figure IV-14. In the first, almost defect-free, structure (Figure IV-14(a)) molecules in the ordered domain all have the same orientation. However, the pattern is chiral because none of the molecular symmetry axes coincide with the lattice vectors. Molecules in the second snapshot, Figure IV-14(b), have the same local ordering as those in Figure IV-14(a), but the cluster has several domain boundaries separating regions of opposite chirality. The orientations of molecules in opposite domains differ by approximately  $40^\circ$ . The  $P_{2z}$  and  $P_{2x}$  averages from 400-600K are approximately 0.8, reflecting the multi-domain structures and the  $\sim 40^\circ$  difference in orientation between domains. Two adjacent enantiomeric domains are structurally commensurate and molecules have the same local coordination environment whether at the domain boundary or in the bulk. Since they do not incur any measurable

energetic penalty, these domain boundaries are commonly observed at equilibrium.

Consistent with these chiral, low-symmetry structures, the  $C_{60}$  order parameters  $\chi_4^2$  and  $\chi_6^2$  average near zero at all temperatures considered.

Finally, we note that in the melting region near 850K, slight changes in  $C_{60ML}$  and  $P_{2l}$  indicate that the transitional structures possess a small amount of upright character, while high and low- $T$  structures lie flat on the substrate. This could be due to coexistence between standing-up and lying-down structures. It is also possible that all configurations pass through an upright intermediate upon melting. These two possibilities are explored later by considering the temperature dependence of the free energy landscapes.

#### (b) Free Energy Landscapes and Combined Results for Molecule 7

The T-REMC simulations with  $E_{FG}$  values of 26.6, 28.9, and 33.3 kcal/mol have shown that weak fullerene-substrate attraction allows disordered aggregates to form and that increasing this attraction stabilizes ordered lying-down structures. However, the individual simulations only give partial insight into the competition between ordered and disordered structures. By combining simulation data and calculating PMFs, we can determine the relative stability of these structures and we can identify the free energy barriers between them. In the next two subsections, we address how these important features of the free energy landscape vary due to changes in  $E_{FG}$  and  $T$ .

##### (b).i. $E_{FG}$ Dependence of the Free Energy Landscape

Here we consider 1D PMFs along the  $C_{60ML}$  order parameter, which does a good job distinguishing the standing-up and lying-down regions. As a reminder to the reader,  $C_{60ML}=2$  corresponds to a lying-down structure and  $C_{60ML}\approx 1.5$  corresponds to the

disordered aggregates with partial upright character. In Figure IV-15, 1D PMF profiles are plotted along this coordinate for values of  $E_{FG}$  between 28.9 and 35.5 kcal/mol. Increasing  $E_{FG}$  has the expected effect of stabilizing lying-down structures and destabilizing standing-up configurations. At  $E_{FG}=32.2$ , the free energy minima differ by  $k_B T$  and are divided by a barrier of  $11 k_B T$ . Above or below this critical value of  $E_{FG}$ , only shallow metastable minima with escape barriers of  $10 k_B T$  or less are observed. For  $E_{FG}=28.9$ , the jaggedness of the PMF near  $C60ML=2$  is most likely due to incomplete sampling. Because of this roughness, it is not clear if the lying-down phase is metastable or not, but the disordered upright structures are clearly the global free energy minimum. In contrast, a strongly attractive surface, such as for  $E_{FG}=35.5$  kcal/mol, shows no evidence of metastable states, and should easily direct molecules into lying-down patterns.

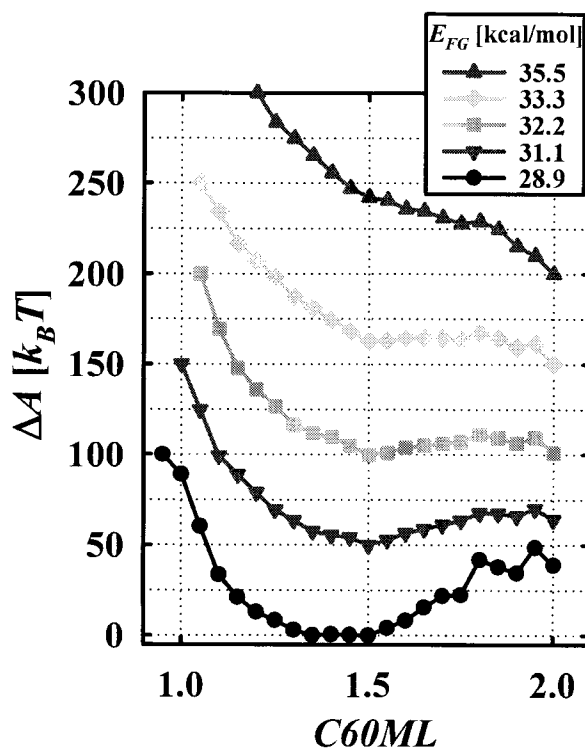


Figure IV-15. PMF profiles along the  $C60ML$  coordinate for molecule 7.  $T=400K$  is fixed and  $E_{FG}$  is varied between 28.9 and 35.5 kcal/mol.

These results suggest that a fullerene-substrate attraction of approximately 33 kcal/mol or greater should guide molecules into lying-down configurations free from kinetic trapping in amorphous aggregate structures. Next we examine how these features of the free energy landscape change for higher temperatures.

(b).ii. Temperature Dependence of The Free Energy Landscape

The temperature dependence of the free energy landscape is considered for  $E_{FG}$  values of 27.8, 32.2 and 35.5 kcal/mol. Shown in Figure IV-16 are 1D PMF profiles as a function of  $C60ML$ . At first glance, there are no abrupt changes in the PMF features when  $T$  is increased. When fullerenes are weakly attracted to the surface ( $E_{FG}=27.8$  kcal/mol), only the amorphous structures are stable from 400K to 800K. With  $E_{FG}$  increased to 32.2 kcal/mol, the two structure regions have approximately equal stability;

however, the transition barrier decreases as the temperature increases from 400K to 800K. Coexistence between these regions best explains the partial upright character in the thermal averaged order parameters in Figure IV-13. With sufficiently strong fullerene-substrate attraction ( $E_{FG}=35.5$  kcal/mol and higher), only lying-down structures are thermodynamically stable, for all temperatures considered.

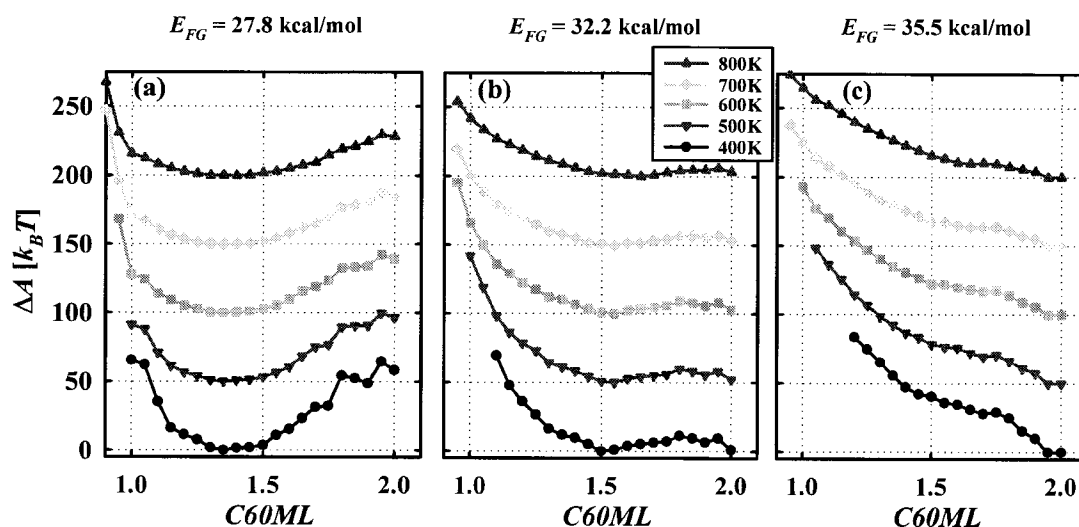


Figure IV-16. 1D PMF profiles for molecule 7 at 400K - 800K for  $E_{FG}$  values of 27.8 kcal/mol (a), 32.2 kcal/mol (b), and 35.5 kcal/mol (c). The ordinate axis ( $\Delta A$ ) indicated on the far left applies to all three panels.

### (c) Summary and Implications for Self-Assembly

For molecule 7, the long  $(Ph)_5$  bridging groups have a clear influence on the observed structural behavior. When  $E_{FG}$  is below about 32 kcal/mol, the bridging groups prevent ordered upright packing. Instead, they stabilize disordered, glassy aggregates where molecules have no discernible orientational or spatial ordering.

When  $E_{FG}$  is above 35 kcal/mol, molecules prefer to lie flat with both fullerenes adsorbed to the surface. The protruding Ph groups prevent  $C_{60}$  close packing, as occurs for molecule 6, but patterning is still possible. What forms is a chiral crystalline pattern

that accommodates the bulky (Ph)<sub>5</sub> groups by limiting the number of C<sub>60</sub>-C<sub>60</sub> NN interactions. This chiral motif is structurally commensurate with its enantiomer, and alternating homochiral domains are commonly observed.

For intermediate  $E_{FG}$  between approximately 32 and 35 kcal/mol, the ordered lying-down and amorphous upright structures are in equilibrium. Thus, for direct self-assembly to the ordered lying-down phase to occur (while avoiding disordered aggregate structures),  $E_{FG}$  should be greater than or equal to 35 kcal/mol.

### **3. Molecule 8**

#### **(a) Individual T-REMC Simulations of Molecule 8**

Compared to the previously considered molecules, the C<sub>60</sub> moieties of **8** are spaced further apart by the long anthracene bridging group. T-REMC simulations for **8** were carried out for  $E_{FG}$  values of 25.5, 26.6, and 28.9 kcal/mol.

##### **(a).i. $E_{FG} = 25.5$ and $26.6$ kcal/mol: Standing-Up Structures**

The two lower  $E_{FG}$  values of 25.5 and 26.6 kcal/mol give very similar results, so here we focus on  $E_{FG}=25.5$  only. In Figure IV-17 we show the thermal averages of heat capacity and the relevant structural order parameters. Over the large temperature range considered, order parameters and the heat capacity shift gradually without any abrupt changes. Two snapshots, Figure IV-18 and Figure IV-19, show structures observed at 439K and 790K, respectively.

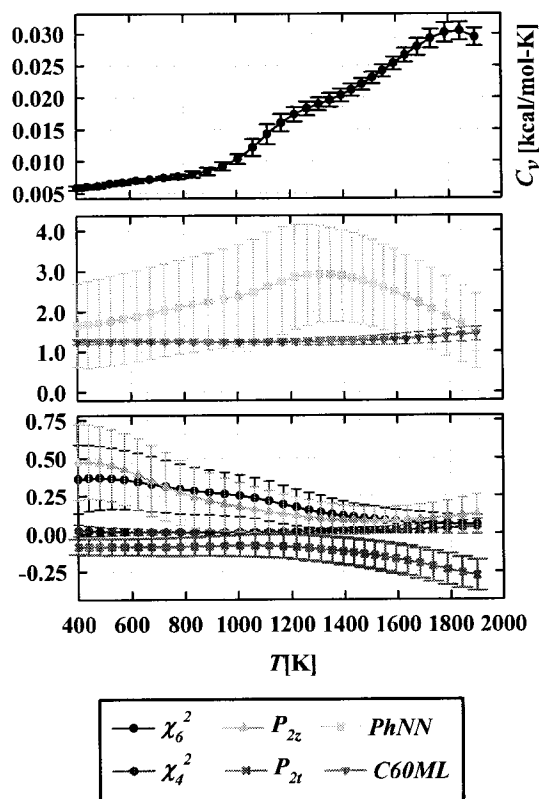


Figure IV-17. The heat capacity (upper panel) and ensemble averaged order parameters (middle and lower panel) for molecule **8** all as a function of  $T$ . Here  $E_{FG}=25.5$  kcal/mol.

Both figures show standing-up configurations with molecules tilting considerably relative to the surface normal. In Figure IV-17, the low- $T$  averages of  $C60ML$  are approximately 1.25, indicating that most molecules have just one  $C_{60}$  adsorbed to the surface. Also at low- $T$ ,  $P_{2t}$  averages -0.1 because molecules tilt about  $59^\circ$  from the surface normal. (note that  $P_{2t} = 0$  is degenerate; the isotropic average and a structure with uniform tilting of  $55^\circ$  would both give this value) Shown in Figure IV-18, the hexagonal packing of molecules creates two hexagonal  $C_{60}$  monolayers separated by the molecules' bridging groups. The upper layer is an elevated and shifted copy of the lower layer

because of the cooperative tilting. This  $z_{bf}$ -axis alignment and hexagonal packing are well characterized by the order parameters  $P_{2z}$  and  $\chi_6^2$ , respectively, in Figure IV-17.

The flat-lying perimeter molecules in Figure IV-18 support the tilted molecules but are otherwise disordered. Because of the small, ( $N=20$ ) cluster size, these disordered edge molecules can heavily skew order parameter averages. In this specific case four of twenty molecules (20%) are disordered to support the 80% that stand upright. For larger clusters, these edge effects would have less impact on structural averages.

We note that at 400K the error bars for the order parameters  $PhNN$ ,  $P_{2z}$  and  $\chi_6^2$  are rather large, indicating that a range of structures are possible. However, the variations in  $C60ML$  are quite small. This indicates that the clusters experience a fair amount of structural variation while keeping constant the number of  $C_{60}$ s adsorbed to the surface.

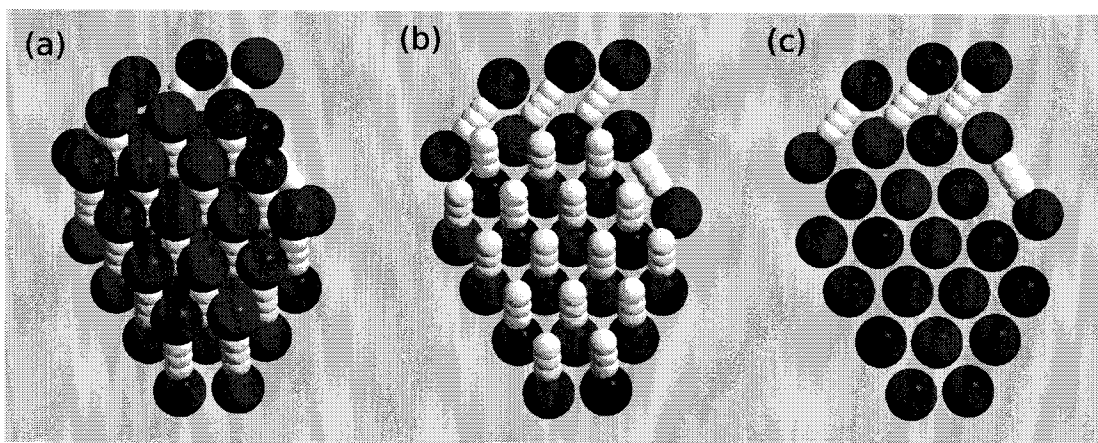


Figure IV-18. A configuration snapshot of Molecule **8** at 439K with  $E_{FG}=25.5$  kcal/mol. The configuration is shown with non-adsorbed  $C_{60}$ s colored red (a), with red  $C_{60}$ s removed (b), and with red  $C_{60}$ s and their bridging groups removed (c).

With increasing temperature, the clusters undergo a very gradual melting transition that can be seen in the heat capacity of Figure IV-17 (upper panel). In this temperature region above 900K there are also gradual changes in the order parameters  $P_{2z}$



and  $\chi_6^2$  (lower panel) and *PhNN* (middle panel). A typical configuration snapshot taken at 790K is shown in Figure IV-19. In this transitional structure, the cluster's upright character and compact geometry are evident. However, the disorder is evident in the distortion of the  $C_{60}$  packing and in how the molecules tilt in many different directions. Despite their obvious differences, both structures (Figure IV-18 and Figure IV-19) have identical values of *C60ML* (1.2).

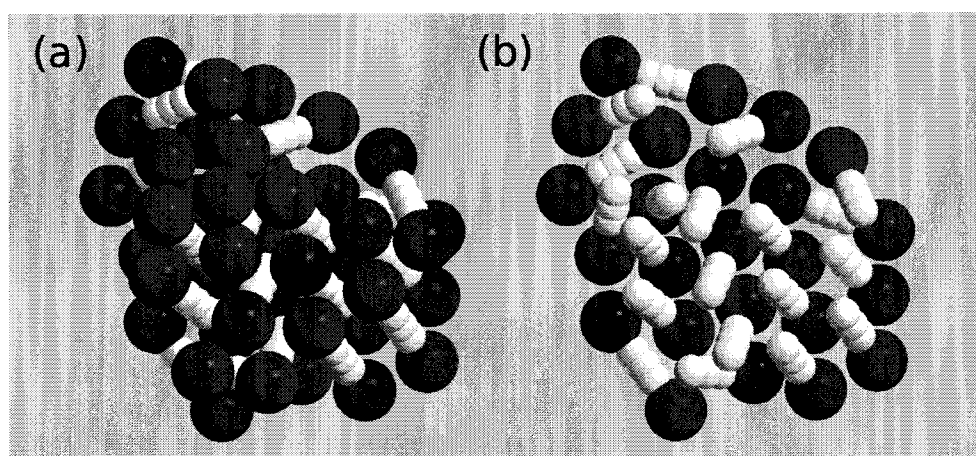


Figure IV-19. A configuration snapshot of Molecule 8 at 790K with  $E_{FG}=25.5$  kcal/mol. The configuration is shown with upper  $C_{60}$ s colored red (a) and with upper  $C_{60}$ s removed (b).

(a).ii.  $E_{FG} = 28.9$  kcal/mol: Lying-Down Structures

Increasing the  $C_{60}$ -Au(111) interaction strength makes it energetically favorable for all  $C_{60}$  moieties to adsorb to the surface. This occurs in simulations of molecule 8 with  $E_{FG}=28.9$  kcal/mol and ordered lying-down domains result.

The cluster's temperature dependent behavior is shown in Figure IV-20. Near 950K, the heat capacity peak and the simultaneous shifts in structural order parameters indicate a phase transition. At temperatures below this transition, the  $P_{2l}$  and *C60ML* parameters indicate that all molecules are lying-down. This can also be seen in the 400K configuration snapshot, Figure IV-21, which shows aligned lying-down 1D rows.

Neighboring rows are joined by zigzag  $C_{60}$ - $C_{60}$  bonds. Within a single row, all molecules are parallel but they are twisted relative to the row direction. Signaling this parallel molecular alignment, the  $P_{2z}$  order parameter is near unity at low temperature (see Figure IV-20).

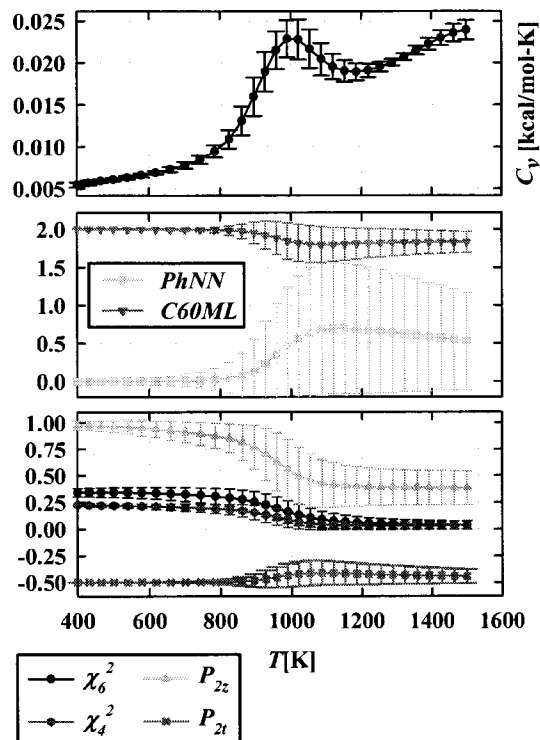


Figure IV-20. The heat capacity and structural order parameter averages as a function of  $T$  for Molecule **8**.  $E_{FG}=28.9$  kcal/mol.

The snapshot Figure IV-21 shows that adjacent rows can be translational copies of each other (for example, the left two rows in Figure IV-21) or they can be (shifted) mirror images of each other (for example, the right two rows in Figure IV-21). The latter (shifted) motif resembles the herringbone patterns seen for molecules **4**, **5**, and **6**. Also, both domain types observed here are structurally commensurate, similar to the commensurate flat-lying domains of molecule **7**. For molecule **8**, the zigzag  $C_{60}$ - $C_{60}$  bonds holding rows together are insensitive to the molecules' orientations. Therefore,

since alternating domains do not incur an energetic penalty they are commonly observed at low- $T$ . Furthermore, because these domains are so structurally similar, none of the order parameters we use can distinguish them or directly measure the fraction of herringbone patterning.

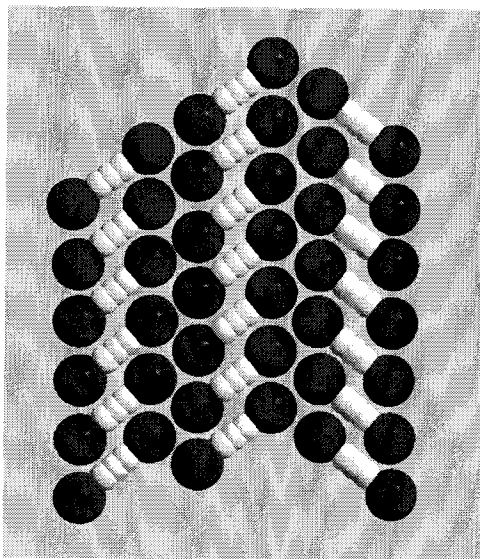


Figure IV-21. A configuration snapshot of Molecule **8** at 400K with  $E_{FG}=28.9$  kcal/mol.

At higher temperature, Figure IV-20 shows a structural transition occurring near 950K. Here the peak in the heat capacity coincides with a drop in  $P_{2z}$ , signaling less  $z_{bf}$  alignment between molecules. In the same temperature region, the changes in  $C60ML$  and  $P_{2l}$  suggest that a fraction of the molecules stand upright, and the increase of  $PhNN$  is due to contacts forming between bridging Ph moieties.

#### (b) Free Energy Landscapes and Combined Results for Molecule **8**

The T-REMC simulations with  $E_{FG}$  values of 25.5, 26.6, and 28.9 kcal/mol have shown that weak fullerene-substrate attraction favors standing-up structures with hexagonal packing and that strong fullerene-substrate attraction stabilizes ordered lying-

down structures. By combining this simulation data and calculating PMFs, we aim to determine the relative stability of these structures and to identify the free energy barriers between them. In the next two subsections, we address how these important features of the free energy landscape vary due to changes in  $E_{FG}$  and  $T$ .

(b).i.  $E_{FG}$  Dependence of The Free Energy Landscape

To illustrate how different values of  $E_{FG}$  influence the free energy landscape, we have calculated 1D PMFs along the  $C60ML$  coordinate, shown in Figure IV-22.

Temperature is fixed at 400K. As a reminder to the reader,  $C60ML=2$  corresponds to a lying-down structure and  $C60ML\approx 1.3$  corresponds to standing-up structures. These PMFs show that a prominent free energy barrier separates the standing-up and lying-down structure regions. For  $E_{FG}=27.2$  kcal/mol, the free energy of the two regions' minima differ by only  $5 k_B T$ . Relative to the minimum ( $0 k_B T$ ), a considerable  $42 k_B T$  barrier separates the regions. For  $E_{FG}$  greater than 27.2 kcal/mol, the lying-down region is the ground state, however the standing-up structures remain metastable. To reach the ground state, systems trapped in these metastable states would have to climb escape barriers of  $25 k_B T$  and  $22 k_B T$  when  $E_{FG}$  is 28.9 and 31.1 kcal/mol, respectively.

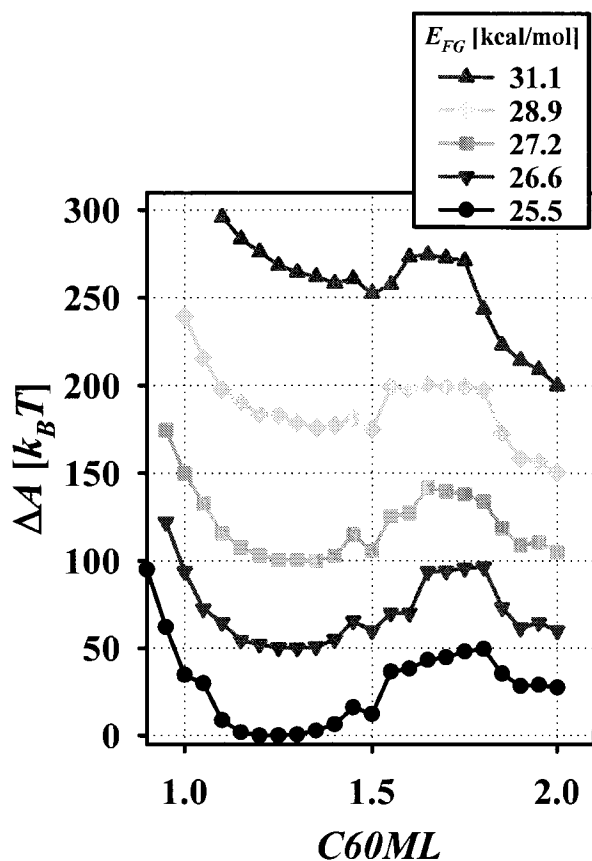


Figure IV-22. PMFs along the  $C60ML$  coordinate for various values of  $E_{FG}$ .  $T=400K$  is fixed in all cases.

When fullerene-substrate attraction is weak ( $E_{FG} \leq 27.2$  kcal/mol), the standing-up structure region is the thermodynamic ground state. In these cases, the lying-down region remains metastable, separated from the ground state by the large free energy barrier.

One limitation of this 1D analysis is that it cannot reveal what other structural variations might exist orthogonal to the  $C60ML$  coordinate. In particular, we noted earlier that there are considerable structural variations within the standing-up region (recall that the configurations in Figure IV-18 and Figure IV-19 both have  $C60ML=1.2$ ). The 2D PMF in Figure IV-23 shows how the upright structure basin forms a long valley along the

$P_{2z}$  coordinate. In contrast, the lying-down region occupies a narrower, funnel-like region of the  $C60ML$ - $P_{2z}$  parameter space. The parameters for the PMF are  $T=400\text{K}$  and  $E_{FG}=27.2$  kcal/mol (where standing-up and lying-down regions have nearly equal free energies). The valley in the standing-up basin spans  $P_{2z}$  values from 0 up to 0.8, and it contains structures with varying  $z_{bf}$  alignment. For comparison, the structures shown in Figure IV-19 and Figure IV-18 have  $P_{2z}$  values of 0.8 and 0.1, respectively.

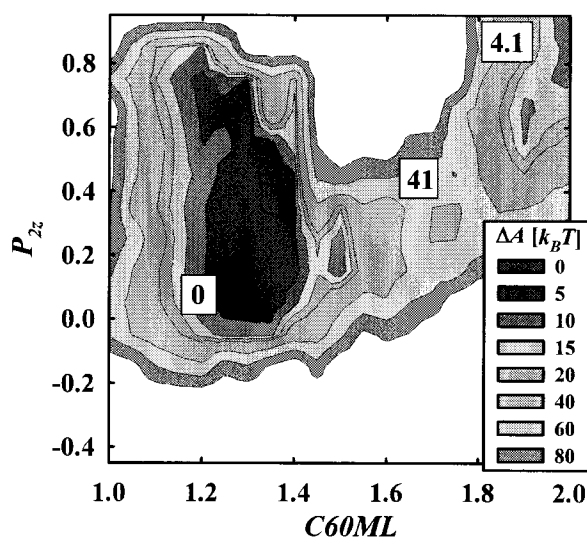


Figure IV-23. A 2D PMF for Molecule **8** where  $E_{FG}=27.2$  kcal/mol and  $T=400\text{K}$ .  $\Delta A$  values are given for the minima and for the barrier between the standing-up and lying-down regions.

Although additional 2D PMFs are not shown here, this  $P_{2z}$  valley does persist for different values of  $E_{FG}$ . Changing  $E_{FG}$  just alters the relative stability of the standing-up valley versus the lying-down funnel.

(b).ii. Temperature Dependence of The Free Energy Landscape

To study the effects of temperature, we focus on three  $E_{FG}$  values: 25.5, 27.2, and 31.1 kcal/mol. For each value, PMFs along the  $C60ML$  coordinate are plotted in Figure IV-24 for temperatures 400-800K. In all three cases (panels (a)-(c)), increasing

temperature smoothes the ruggedness of the profile and lowers (or eliminates) the barrier between the two stable regions.

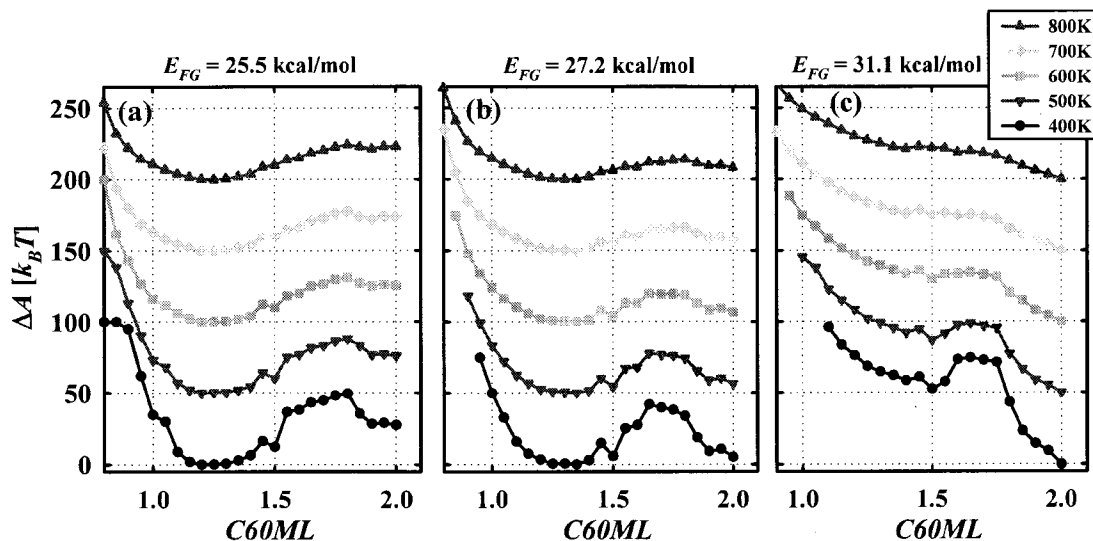


Figure IV-24. 1D PMF profiles for molecule **8** at 400K - 800K for  $E_{FG}$  values of 25.5 kcal/mol (a), 27.2 kcal/mol (b), and 31.1 kcal/mol (c). The ordinate axis ( $\Delta A$ ) indicated on the far left applies to all three panels.

Strong fullerene-surface attraction ( $E_{FG} = 31.1$  kcal/mol (panel (c))) destabilizes the standing-up structure region and stabilizes the lying-down structure region. At 400K, the standing-up region is metastable, but it is over  $50 k_B T$  higher in free energy than the ground state. From 600K to 800K, the standing-up region resembles a free energy plateau, with small variations of  $2-3 k_B T$ , but otherwise the free energy gradient slopes towards the lying-down region.

For the intermediate  $E_{FG}$  value (27.2 kcal/mol, panel (b)) at 400K, the standing-up and lying-down minima have relative free energies of 0 and  $5 k_B T$ , respectively, but they are separated by a barrier  $42 k_B T$  above the ground state. When  $T=800K$ , the standing up

region remains the ground state, the barrier decreases to  $14 k_B T$  and the lying-down region has a free energy minimum of  $8.1 k_B T$ .

Weak fullerene-surface attraction ( $E_{FG} = 25.5$  kcal/mol (panel (a)) favors the standing-up structures. Metastable lying-down configurations are about  $25 k_B T$  higher in free energy for temperatures 400K-800K. The escape barrier for a trapped, lying-down structure decreases from  $22 k_B T$  at 400K to just  $2 k_B T$  at 800K. Although the standing-up region is strongly preferred, we noted earlier that structures can vary considerably within this region (see Figure IV-23). In particular, they can be highly aligned or not very well aligned, and this alignment can be measured with the  $P_{2z}$  order parameter.

To see how temperature influences the stability of the various standing-up structures, we plot 2D PMFs using  $C60ML$  and  $P_{2z}$  as reduced coordinates (see Figure IV-25). Beginning at 400K (panel (a)), the contours show that the broad, standing-up free energy valley contains multiple minima separated by barriers of less than  $5 k_B T$ . These minima are most likely artifacts due to partial sampling and the finite size effects. When increasing temperature to 600K and 800K (panels (b) and (c), respectively) these individual regions pool to form a single flat basin. So throughout the temperatures 400K-800K the free energy landscape does not direct clusters to any specific ordered or disordered structure.



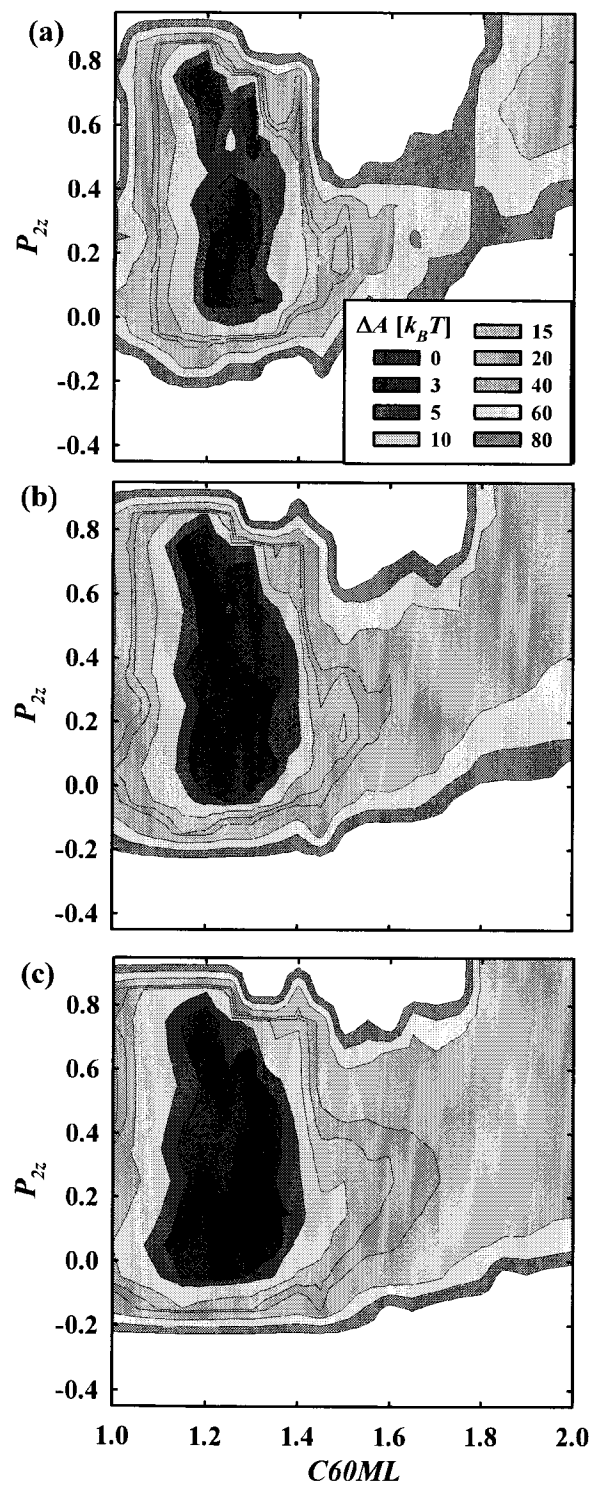


Figure IV-25. 2D PMFs for molecule 8 at 400K (a), 600K (b), and 800K (c). In all panels,  $E_{FG}=25.5$  kcal/mol. The  $C60ML$  scale below panel (c) applies to (a) and (b).

(c) Summary and Implications for self-assembly

Aside from setting the intramolecular C<sub>60</sub>-C<sub>60</sub> spacing, the bridging groups of molecule **8** have no direct influence on self-assembled patterns. It is primarily the strength of the fullerene-substrate attraction,  $E_{FG}$ , that determines structural behavior.

Within an intermediate range of  $E_{FG}$  values, approximately 26-30 kcal/mol, bistable free energy landscapes exist. Standing-up and lying-down morphologies have similar free energies, and are likely to coexist. In this case, direct self-assembly of a single target structure is unlikely.

Lower values of  $E_{FG}$  stabilize standing-up structures in which C<sub>60</sub> moieties form two hexagonal lattices separated by their molecules' bridging groups. Ordered, aligned motifs are observed (see Figure IV-18), but these ordered structures exist in a flat, free energy valley shared with other less ordered structures (Figure IV-19). These structural variations are partly due to the narrowness of the bridging groups which cannot interact to help stabilize ordered structures. This is in contrast to the outward pointing Ph moieties of molecule **6** which interlocked to form a herringbone pattern, thereby stabilizing the upright hexagonal phase. So, although configurations with standing-up character are thermodynamically stable, the free energy landscape for **8** does not drive self-assembly of highly ordered structures.

At high values of  $E_{FG}$ , above 30 kcal/mol, fullerenes all adsorb on the surface and we observe ordered lying-down structures. Molecules parallel each other but are slightly offset, and they form extended 1D rows. Adjacent rows are held together by zigzag C<sub>60</sub>-C<sub>60</sub> bonds. Neighboring rows can be translational copies or mirror images. Both cases are energetically degenerate and both are commonly observed in configuration snapshots. In

this case, the free energy landscape promotes direct self-assembly of these structures with no expected interference from kinetic/metastable traps.

#### **D. Concluding Remarks**

We have carried out coarse grained modeling simulations to study the self-assembly of bis-fullerene molecular clusters on surfaces. We considered three molecules, each having a different arrangement of phenyl groups to covalently “bridge” the fullerenes. Free energy landscapes for these systems were generally characterized by two prominent stable regions corresponding to standing-up and lying-down morphologies. To thoroughly sample these different structures, we used temperature replica exchange and fullerene-substrate energy biasing. Global free energy landscapes were determined with the use of the statistical reweighting methods T-WHAM and WHAM.

The relative stability of standing-up and lying-down structures depends primarily on the strength of the fullerene-substrate binding energy,  $E_{FG}$ , and to a lesser extent on temperature. For each molecule, we identified a critical value of  $E_{FG}$  where the system was bistable. At this critical value, spontaneous self-assembly to a single target structure would be unlikely. However, increasing or decreasing  $E_{FG}$  (relative to this value) would stabilize one structure and make the other metastable or unstable.

The specific standing-up and lying-down structures we observe and the critical  $E_{FG}$  value depend on the molecules’ bridging groups. The molecules with protruding Ph moieties (**6** and **7**) cannot pack hexagonally when lying-down on the substrate. However, both **6** and **7** self-assemble into ordered structures with lower symmetries. In upright configurations, **6** forms an ordered hexagonal structure where the bridging groups align to form a dense herringbone pattern. The bulky bridging groups of **7**, however, prevent

ordered upright structures, and only amorphous aggregates are observed. Molecule **8** differs from **6** and **7** in that its two C<sub>60</sub>s are spaced further apart and it has no Ph moieties perpendicular to its C<sub>60</sub>-C<sub>60</sub> axis. Standing-up structures of **8** have varying degrees of hexagonal packing, but they occupy a broad valley in the free energy landscape and do not self-assemble to a single target structure. The narrow bridging groups are unable to direct patterning. In lying-down structures, lamellar rows self-assemble, and parallel rows can have herringbone or translational symmetry.

In closing, we have presented a comprehensive modeling approach to determine free energy landscapes of bis-fullerene clusters adsorbed on surfaces. This approach has been applied to three different bis-fullerene compounds, each with a different “bridging group.” For each molecule, we have identified morphologies that spontaneously self-assemble. We have also identified cases where self-assembly is hindered by kinetic or metastable traps, and the best conditions for direct self-assembly.

## Appendix: Complete Potential Energy Functions

Here we detail the complete potential energy function for the cluster of fullerene thiolates and the Au(111) substrate. These definitions are presented so as to be self contained. Variable definitions and notation used herein do not apply in the chapter text, unless stated in the text. The total potential energy,  $U$ , for  $N$  molecules on the Au substrate is given by:

$$U(R_1, R_2, \dots, R_N) = \sum_{j=1}^N U_{mol-surf}(R_j) + \sum_{j=1}^N \sum_{k \neq j}^N U_{mol-mol}(R_j, R_k) \quad (\text{V.1})$$

Each rigid molecule  $j$  is fully defined by seven coordinates:

$$R_j = (x_j^o, y_j^o, z_j^o, q_{0,j}, q_{1,j}, q_{2,j}, q_{3,j}) \quad (\text{V.2})$$

where  $(x_j^o, y_j^o, z_j^o)$  are the Cartesian coordinates of the molecule's coordinate origin relative to the arbitrary global coordinate origin, and  $(q_0, q_1, q_2, q_3)$  is a unit quaternion specifying the orientation of the molecule's coordinate system with respect to the global coordinate frame.

Each molecule has three united-atom (UA) "sites": the  $C_{60}$  moiety, the phenyl moiety, and the S atom. Each UA's space-fixed Cartesian coordinates,  $\mathbf{r}_{j'} = (x_{j'}, y_{j'}, z_{j'})$ , are obtained from the 7-vector  $R_j$ , together with the geometry parameters of the molecule. The index  $j'$  implies that the UA site belongs to molecule  $j$ . The intermolecular potential,  $U_{mol-mol}(R_j, R_k)$ , is given by a sum over pairwise interactions of all UA site combinations between a pair of molecules.

$$U_{mol-mol}(R_j, R_k) = \sum_{j'} \sum_{k'} U_{UA-UA}(\mathbf{r}_{j'}, \mathbf{r}_{k'}). \quad (\text{V.3})$$

The molecule-surface potential is given by a sum over the individual UA-surface interactions

$$U_{mol-surf}(R_j) = \sum_{j'} U_{UA-surf}(\mathbf{r}_{j'}). \quad (\text{V.4})$$

### A. UA-UA interactions

The essential parameters of the UA-UA pairwise potentials are summarized in Table V-I.

	$C_{60}$	Ph	S
$C_{60}$	G (10.06, 6.4)		
Ph	LJ (8.2, 0.5)	LJ (6.4, 0.75)	
S	LJ (6.055, 1.137)	LJ (4.255, 0.389)	LJ (2.11, 0.397)

Table V-I. UA-UA pairwise potential parameters. Each entry lists the functional form (G stands for Girifalco and LJ for Lennard-Jones) and  $(r_e, E)$  where  $E$  is the minimum energy in kcal/mol and  $r_e$  is the equilibrium separation in Å.

The C<sub>60</sub>-C<sub>60</sub> interaction is described by the Girifalco potential [88]. Specifically, for two C<sub>60</sub>s with distance  $r$  between their centers of mass,

$$U_{C_{60}-C_{60}}(r) = \frac{-\alpha_1}{r} \left[ \frac{1}{(r-d_f)^3} + \frac{1}{(r+d_f)^3} - \frac{2}{r^3} \right] + \frac{\alpha_2}{r} \left[ \frac{1}{(r-d_f)^9} + \frac{1}{(r+d_f)^9} - \frac{2}{r^9} \right], \quad (\text{V.5})$$

and

$$d_f = 7.1\text{\AA}, \quad \alpha_1 = 27.39 \times 10^2 \frac{\text{kcal} \cdot \text{\AA}^4}{\text{mol}}, \quad \alpha_2 = 63.65 \times 10^4 \frac{\text{kcal} \cdot \text{\AA}^{10}}{\text{mol}}. \quad (\text{V.6})$$

The parameter  $d_f$  is the diameter of the C<sub>60</sub> cage.

All other site-site interactions are given by the Lennard-Jones (LJ) potential:

$$U_{LJ}(r) = E \left( \left( \frac{r_e}{r} \right)^{12} - 2 \left( \frac{r_e}{r} \right)^6 \right). \quad (\text{V.7})$$

## **B. UA-Surface interactions**

The C<sub>60</sub>-Au(111) potential and the S-Au(111) potential use the same functional form. This function is calculated using the Cartesian coordinates,  $\mathbf{r} = (x, y, z)$ , of the C<sub>60</sub> center of mass or those of the S atom. The potential assumes that the top layer of Au atoms lies in the x-y plane and  $z > 0$ . A Morse potential accounts for the average vertical attraction. Added to this, a corrugation term represents the Au atoms and the surface periodicity using the hexagonal lattice coordinates  $S_1$  and  $S_2$ . This is written as

$$U_{UA-Au(111)}(x, y, z) = \tilde{E}_M \left[ \exp(-2\tilde{\rho}(z - \tilde{z})) - 2 \exp(-\tilde{\rho}(z - \tilde{z})) \right] + \tilde{E}_{rep} \exp(-\tilde{\alpha}z) \left[ \cos(S_1) + \cos(S_2) + \cos(S_1 + S_2) \right], \quad (\text{V.8})$$

with

$$\begin{pmatrix} S_1 \\ S_2 \end{pmatrix} = \begin{pmatrix} 2\pi \\ s_{Au} \end{pmatrix} \begin{pmatrix} 0 & 2/\sqrt{3} \\ 1 & -1/\sqrt{3} \end{pmatrix} \begin{pmatrix} x \\ y \end{pmatrix}. \quad (\text{V.9})$$

The parameter  $s_{Au} = 2.89\text{\AA}$  is the Au-Au atom spacing. The parameters for both the S-Au(111) and C<sub>60</sub>-Au(111) potentials are given in Table V-II. The tildes are used to further distinguish these parameters from other parameters in the chapter text.

	$\tilde{E}_M$	$\tilde{\rho}$	$\tilde{z}$	$\tilde{E}_{rep}$	$\tilde{\alpha}$
	[kcal/mol]	[Å <sup>-1</sup> ]	[Å]	[kcal/mol]	[Å <sup>-1</sup> ]
C <sub>60</sub> -Au(111)	22.2	1.45	5.96	1.45e <sup>10</sup>	3.75
S-Au(111)	36.8	1.18	2.11	3630	3.35

Table V-II. Parameters for the S-Au(111) and C<sub>60</sub>-Au(111) potential energy function.

The phenyl-surface interaction is given by a z-dependent LJ potential with  $(r_e, E)=(4.6\text{Å}, 0.5\text{kcal/mol})$ .

## LIST OF REFERENCES

- [1] D.Y. Ryu, K. Shin, E. Drockenmuller, C.J. Hawker, and T.P. Russell, A Generalized Approach to the Modification of Solid Surfaces. *Science* **308**, 236-239 (2005).
- [2] M.K. Chaudhury and G.M. Whitesides, How to Make Water Run Uphill. *Science* **256**, 1539-1541 (1992).
- [3] A.L. Eckermann, D.J. Feld, J.A. Shaw, and T.J. Meade, Electrochemistry of Redox-Active Self-Assembled Monolayers. *Coord. Chem. Rev.* **254**, 1769-1802 (2010).
- [4] T. Sakanoue and H. Sirringhaus, Band-Like Temperature Dependence of Mobility in a Solution-Processed Organic Semiconductor. *Nat Mater* **9**, 736-740 (2010).
- [5] Y. Qi, X. Liu, B.L.M. Hendriksen, V. Navarro, J.Y. Park, I. Ratera, J.M. Klopp, C. Edder, F.J. Himpsel, J.M.J. Fréchet, E.E. Haller, and M. Salmeron, Influence of Molecular Ordering on Electrical and Friction Properties of  $\omega$ -(trans-4-Stilbene)Alkylthiol Self-Assembled Monolayers on Au (111). *Langmuir* **26**, 16522-16528 (2010).
- [6] C. Chen, M. Wang, J. Li, N. Pootrakulchote, L. Alibabaei, C. Ngoc-le, J. Decoppet, J. Tsai, C. Grätzel, C. Wu, S.M. Zakeeruddin, and M. Grätzel, Highly Efficient Light-Harvesting Ruthenium Sensitizer for Thin-Film Dye-Sensitized Solar Cells. *ACS Nano* **3**, 3103-3109 (2009).
- [7] Y. Hu and S. Granick, Microscopic Study of Thin Film Lubrication and Its Contributions to Macroscopic Tribology. *Tribology Letters* **5**, 81-88 (1998).
- [8] S. Ferretti, S. Paynter, D.A. Russell, K.E. Sapsford, and D.J. Richardson, Self-Assembled Monolayers: A Versatile Tool for the Formulation of Bio-Surfaces. *TrAC, Trends Anal. Chem.* **19**, 530-540 (2000).
- [9] J. Gooding, F. Mearns, W. Yang, and J. Liu, Self-Assembled Monolayers into the 21st Century: Recent Advances and Applications. *Electroanalysis* **15**, 81-96 (2003).
- [10] E.C.P. Smits, S.G.J. Mathijssen, P.A. van Hal, S. Setayesh, T.C.T. Geuns, K.A.H.A. Mutsaers, E. Cantatore, H.J. Wondergem, O. Werzer, R. Resel, M. Kemerink, S. Kirchmeyer, A.M. Muzafarov, S.A. Ponomarenko, B. de Boer, P.W.M. Blom, and D.M. de Leeuw, Bottom-up Organic Integrated Circuits. *Nature* **455**, 956-959 (2008).
- [11] D. Bonifazi, O. Enger, and F. Diederich, Supramolecular [60]fullerene Chemistry on Surfaces. *Chem. Soc. Rev.* **36**, 390-414 (2007).
- [12] H.W. Kroto, J.R. Heath, S.C. O'Brien, R.F. Curl, and R.E. Smalley, C60: Buckminsterfullerene. *Nature* **318**, 162-163 (1985).
- [13] S. Uemura, M. Sakata, C. Hirayama, and M. Kunitake, Fullerene Adlayers on Various Single-Crystal Metal Surfaces Prepared by Transfer from L Films. *Langmuir* **20**, 9198-9201 (2004).
- [14] G. Maruccio, R. Cingolani, and R. Rinaldi, Projecting the Nanoworld: Concepts, Results and Perspectives of Molecular Electronics. *J. Mater. Chem.* **14**, 542-554 (2004).



- [15] D.M. Guldi, in *Nanoparticles and Nanostructured Films* (Wiley-VCH, Weinheim, 1998), pp. 119-143.
- [16] A. Patnaik, H. Setoyama, and N. Ueno, Surface/Interface Electronic Structure in C60 Anchored Amino-thiolate Self-Assembled Monolayer: An Approach to Molecular Electronics. *J. Chem. Phys.* **120**, 6214-6221 (2004).
- [17] J.B. Briggs and G.P. Miller, [60]Fullerene-Acene Chemistry: A Review. *Comptes Rendus Chimie* **9**, 916-927 (2006).
- [18] P. Belik, A. Gügel, J. Spickermann, and K. Müllen, Reaction of Buckminsterfullerene with Ortho-Quinodimethane: A New Access to Stable C60 Derivatives. *Angew. Chem., Int. Ed. Engl.* **32**, 78-80 (1993).
- [19] V.K. Periya, I. Koike, Y. Kitamura, S. Iwamatsu, and S. Murata, Hydrophilic [60]fullerene Carboxylic Acid Derivatives Retaining the Original 60[pi] Electronic System. *Tetra. Lett.* **45**, 8311-8313 (2004).
- [20] L. Wang and H. Cheng, Density Functional Study of the Adsorption of a C60 Monolayer on Ag(111) and Au(111) Surfaces. *Phys. Rev. B* **69**, 165417 (2004).
- [21] E.I. Altman and R.J. Colton, Nucleation, Growth, and Structure of Fullerene Films on Au(111). *Surf. Sci.* **279**, 49-67 (1992).
- [22] E.I. Altman and R.J. Colton, The Interaction of C60 with Noble Metal Surfaces. *Surf. Sci.* **295**, 13-33 (1993).
- [23] E.I. Altman and R.J. Colton, Determination of the Orientation of C60 Adsorbed on Au(111) and Ag(111). *Phys. Rev. B* **48**, 18244-18249 (1993).
- [24] A. Ogawa, M. Tachibana, M. Kondo, K. Yoshizawa, H. Fujimoto, and R. Hoffmann, Orbital Interactions Between a C60 Molecule and Cu(111) Surface. *J. Phys. Chem. B* **107**, 12672-12679 (2003).
- [25] C. Tzeng, W. Lo, J. Yuh, R. Chu, and K. Tsuei, Photoemission, Near-Edge X-Ray-Absorption Spectroscopy, and Low-Energy Electron-Diffraction Study of C60 on Au(111) Surfaces. *Phys. Rev. B* **61**, 2263-2272 (2000).
- [26] S. Guo, D. Fogarty, P. Nagel, and S. Kandel, Thermal Diffusion of C60 Molecules and Clusters on Au(111). *J. Phys. Chem. B* **108**, 14074-14081 (2004).
- [27] A.V. Akimov, A.V. Nemukhin, A.A. Moskovsky, A.B. Kolomeisky, and J.M. Tour, Molecular Dynamics of Surface-Moving Thermally Driven Nanocars. *J. Chem. Theory Comput.* **4**, 652-656 (2008).
- [28] Y. Shirai, A.J. Osgood, Y. Zhao, Y. Yao, L. Saudan, H. Yang, C. Yu-Hung, L.B. Alemany, T. Sasaki, J. Morin, J.M. Guerrero, K.F. Kelly, and J.M. Tour, Surface-Rolling Molecules. *J. Am. Chem. Soc.* **128**, 4854-4864 (2006).
- [29] Y. Shirai, A.J. Osgood, Y. Zhao, K.F. Kelly, and J.M. Tour, Directional Control in Thermally Driven Single-Molecule Nanocars. *J. Am. Chem. Soc.* **5**, 2330-2334 (2005).
- [30] J.C. Hummelen, B.W. Knight, F. LePeq, F. Wudl, J. Yao, and C.L. Wilkins, Preparation and Characterization of Fulleroid and Methanofullerene Derivatives. *J. Org. Chem.* **60**, 532-538 (1995).
- [31] G. Li, V. Shrotriya, J. Huang, Y. Yao, T. Moriarty, K. Emery, and Y. Yang, High-Efficiency Solution Processable Polymer Photovoltaic Cells by Self-Organization of Polymer Blends. *Nat Mater* **4**, 864-868 (2005).
- [32] J.L. Segura, N. Martín, and D.M. Guldi, Materials for Organic Solar Cells: The C60-Conjugated Oligomer Approach. *Chem. Soc. Rev.* **34**, 31-47 (2005).

- [33] X. Yang, J. Loos, S.C. Veenstra, W.J.H. Verhees, M.M. Wienk, J.M. Kroon, M.A.J. Michels, and R.A.J. Janssen, Nanoscale Morphology of High-Performance Polymer Solar Cells. *Nano Lett.* **5**, 579-583 (2005).
- [34] B. Xue, B. Vaughan, C. Poh, K.B. Burke, L. Thomsen, A. Stapleton, X. Zhou, G.W. Bryant, W. Belcher, and P.C. Dastoor, Vertical Stratification and Interfacial Structure in P3HT:PCBM Organic Solar Cells. *J. Phys. Chem. C* **114**, 15797-15805 (2010).
- [35] C. Li, M. Liu, N.G. Pschirer, M. Baumgarten, and K. Müllen, Polyphenylene-Based Materials for Organic Photovoltaics. *Chem. Rev.* **110**, 6817-6855 (2010).
- [36] S. Günes, H. Neugebauer, and N.S. Sariciftci, Conjugated Polymer-Based Organic Solar Cells. *Chem. Rev.* **107**, 1324-1338 (2007).
- [37] X. Yang and J. Loos, Toward High-Performance Polymer Solar Cells: The Importance of Morphology Control. *Macromolecules* **40**, 1353-1362 (2007).
- [38] D.K. Schwartz, Mechanisms and Kinetics of Self-Assembled Monolayer Formation. *Annu. Rev. Phys. Chem.* **52**, 107-137 (2001).
- [39] A. Ulman, Formation and Structure of Self-Assembled Monolayers. *Chem. Rev.* **96**, 1533-1554 (1996).
- [40] F. Schreiber, Self-Assembled Monolayers: From 'simple' Model Systems to Biofunctionalized Interfaces. *J. Phys.: Condens. Matter* **16**, R881-R900 (2004).
- [41] A. Cossaro, R. Mazzarello, R. Rousseau, L. Casalis, A. Verdini, A. Kohlmeyer, L. Floreano, S. Scandolo, A. Morgante, M.L. Klein, and G. Scoles, X-Ray Diffraction and Computation Yield the Structure of Alkanethiols on Gold(111). *Science* **321**, 943-946 (2008).
- [42] C. Taut, A. Pertsin, and M. Grunze, Monte Carlo Studies of Self-Assembled Monolayers Using Simple Generalized Models. 1. Behavior of Headgroups in a Periodic Substrate Field. *Langmuir* **12**, 3481-3489 (1996).
- [43] A. Pertsin and M. Grunze, Monte Carlo Studies of Self-Assembled Monolayers Using Simple Generalized Models. II. A Two-Site Molecular Model. *J. Chem. Phys.* **106**, 7343-7351 (1997).
- [44] J. Hautman and M.L. Klein, Simulation of a Monolayer of Alkyl Thiol Chains. *J. Chem. Phys.* **91**, 4994-5001 (1989).
- [45] L. Zhang, W.A. Goddard III, and S. Jiang, Molecular Simulation Study of the C(4 X 2) Superlattice Structure of Alkanethiol Self-Assembled Monolayers on Au(111). *J. Chem. Phys.* **117**, 7342-7349 (2002).
- [46] O. Alexiadis, V.A. Harmandaris, V.G. Mavrantzas, and L.D. Site, Atomistic Simulation of Alkanethiol Self-Assembled Monolayers on Different Metal Surfaces Via a Quantum, First-Principles Parametrization of the Sulfur-Metal Interaction. *J. Phys. Chem. C* **111**, 6380-6391 (2007).
- [47] Y. Shon, K. Kelly, N. Halas, and T. Lee, Fullerene-Terminated Alkanethiolate SAMs on Gold Generated from Unsymmetrical Disulfides. *Langmuir* **15**, 5329-5332 (1999).
- [48] X. Shi, W.B. Caldwell, K. Chen, and C.A. Mirkin, A Well-Defined Surface-Confinable Fullerene: Monolayer Self-Assembly on Au(111). *J. Am. Chem. Soc.* **116**, 11598-11599 (1994).
- [49] J.V. Barth, Molecular Architectonic on Metal Surfaces. *Annu. Rev. Phys. Chem.* **58**, 375-407 (2007).

- [50] M.M. Ling and Z. Bao, Thin Film Deposition, Patterning, and Printing in Organic Thin Film Transistors. *Chem. Mater.* **16**, 4824-4840 (2004).
- [51] M. Lackinger, S. Griessl, W.M. Heckl, M. Hietschold, and G.W. Flynn, Self-Assembly of Trimesic Acid at the Liquid-Solid Interface: A Study of Solvent-Induced Polymorphism. *Langmuir* **21**, 4984-4988 (2005).
- [52] S. De Feyter and F.C. De Schryver, Two-Dimensional Supramolecular Self-Assembly Probed by Scanning Tunneling Microscopy. *Chem. Soc. Rev.* **32**, 139-150 (2003).
- [53] U. Schlickum, R. Decker, F. Klappenberger, G. Zoppellaro, S. Klyatskaya, W. Auwärter, S. Neppel, K. Kern, H. Brune, M. Ruben, and J.V. Barth, Chiral Kagomé Lattice from Simple Ditopic Molecular Bricks. *J. Am. Chem. Soc.* **130**, 11778-11782 (2008).
- [54] B. Diaconescu, T. Yang, S. Berber, M. Jazdyk, G. Miller, D. Tománek, and K. Pohl, Molecular Self-Assembly of Functionalized Fullerenes on a Metal Surface. *Phys. Rev. Lett.* **102**, 056102 (2009).
- [55] G. Pawin, K.L. Wong, K. Kwon, and L. Bartels, A Homomolecular Porous Network at a Cu(111) Surface. *Science* **313**, 961-962 (2006).
- [56] R.J. Wilson, G. Meijer, D.S. Bethune, R.D. Johnson, D.D. Chambliss, M.S. de Vries, H.E. Hunziker, and H.R. Wendt, Imaging C60 Clusters on a Surface Using a Scanning Tunneling Microscope. *Nature* **348**, 621-622 (1990).
- [57] M. Hietschold, M. Lackinger, S. Griessl, W. Heckl, T. Gopakumar, and G. Flynn, Molecular Structures on Crystalline Metallic Surfaces - From STM Images to Molecular Electronics. *Microelectronic Engineering* **82**, 207-214 (2005).
- [58] S. Clair, S. Pons, A.P. Seitsonen, H. Brune, K. Kern, and J.V. Barth, STM Study of Terephthalic Acid Self-Assembly on Au(111): Hydrogen-Bonded Sheets on an Inhomogeneous Substrate. *J. Phys. Chem. B* **108**, 14585-14590 (2004).
- [59] G. Tomba, L.C. Ciacchi, and A.D. Vita, Atomic-Level Studies of Molecular Self-Assembly on Metallic Surfaces. *Adv. Mater.* **21**, 1055-1066 (2009).
- [60] J.A. Theobald, N.S. Oxtoby, M.A. Phillips, N.R. Champness, and P.H. Beton, Controlling Molecular Deposition and Layer Structure with Supramolecular Surface Assemblies. *Nature* **424**, 1029-1031 (2003).
- [61] U.K. Weber, V.M. Burlakov, L.M.A. Perdigão, R.H.J. Fawcett, P.H. Beton, N.R. Champness, J.H. Jefferson, G.A.D. Briggs, and D.G. Pettifor, Role of Interaction Anisotropy in the Formation and Stability of Molecular Templates. *Phys. Rev. Lett.* **100**, 156101 (2008).
- [62] Y. Ye, W. Sun, Y. Wang, X. Shao, X. Xu, F. Cheng, J. Li, and K. Wu, A Unified Model: Self-Assembly of Trimesic Acid on Gold. *J. Phys. Chem. C* **111**, 10138-10141 (2007).
- [63] L.M.A. Perdigão, N.R. Champness, and P.H. Beton, Surface Self-Assembly of the Cyanuric Acid-Melamine Hydrogen Bonded Network. *Chem. Commun.* 538-540 (2006).
- [64] P.A. Staniec, L.M.A. Perdigão, B.L. Rogers, N.R. Champness, and P.H. Beton, Honeycomb Networks and Chiral Superstructures Formed by Cyanuric Acid and Melamine on Au(111). *J. Phys. Chem. C* **111**, 886-893 (2007).
- [65] O. Ivasenko and D.F. Perepichka, Mastering Fundamentals of Supramolecular Design with Carboxylic Acids. Common Lessons from X-Ray Crystallography and

- Scanning Tunneling Microscopy. *Chem. Soc. Rev.* (2011).
- [66] J. Zhao, Y. Li, Z. Lin, L. Xie, N. Shi, X. Wu, C. Wang, and W. Huang, Molecule Length Directed Self-Assembly Behavior of Tetratopic Oligomeric Phenylene–Ethylenes End-Capped with Carboxylic Groups by Scanning Tunneling Microscopy. *J. Phys. Chem. C* **114**, 9931-9937 (2010).
- [67] T. Yokoyama, T. Kamikado, S. Yokoyama, and S. Mashiko, Conformation Selective Assembly of Carboxyphenyl Substituted Porphyrins on Au (111). *J. Chem. Phys.* **121**, 11993-11997 (2004).
- [68] L. Schmidt-Mende, A. Fechtenkötter, K. Müllen, E. Moons, R.H. Friend, and J.D. MacKenzie, Self-Organized Discotic Liquid Crystals for High-Efficiency Organic Photovoltaics. *Science* **293**, 1119-1122 (2001).
- [69] K. Tahara, S. Furukawa, H. Uji-i, T. Uchino, T. Ichikawa, J. Zhang, W. Mamdouh, M. Sonoda, F.C. De Schryver, S. De Feyter, and Y. Tobe, Two-Dimensional Porous Molecular Networks of Dehydrobenzo[12]annulene Derivatives Via Alkyl Chain Interdigitation. *J. Am. Chem. Soc.* **128**, 16613-16625 (2006).
- [70] G. Schull, L. Douillard, C. Fiorini-Debuisschert, F. Charra, F. Mathevet, D. Kreher, and A. Attias, Single-Molecule Dynamics in a Self-Assembled 2D Molecular Sieve. *Nano Lett.* **6**, 1360-1363 (2006).
- [71] Y. Wei, W. Tong, and M.B. Zimmt, Self-Assembly of Patterned Monolayers with Nanometer Features: Molecular Selection Based on Dipole Interactions and Chain Length. *J. Am. Chem. Soc.* **130**, 3399-3405 (2008).
- [72] M. Matsumoto, J. Inukai, S. Yoshimoto, Y. Takeyama, O. Ito, and K. Itaya, Two-Dimensional Network Formation in the C60 Malonic Acid Adlayer on Au(111). *J. Phys. Chem. C* **111**, 13297-13300 (2007).
- [73] X. Zhang, F. Yin, R. Palmer, and Q. Guo, The C60/Au(111) Interface at Room Temperature: A Scanning Tunneling Microscopy Study. *Surf. Sci.* **602**, 885-892 (2008).
- [74] Y. Shirai, L. Cheng, B. Chen, and J.M. Tour, Characterization of Self-Assembled Monolayers of Fullerene Derivatives on Gold Surfaces: Implications for Device Evaluations. *J. Am. Chem. Soc.* **128**, 13479-13489 (2006).
- [75] N. Sändig and F. Zerbetto, Molecules on Gold. *Chem. Commun.* **46**, 667-676 (2010).
- [76] L. Sánchez, R. Otero, J.M. Gallego, R. Miranda, and N. Martín, Ordering Fullerenes at the Nanometer Scale on Solid Surfaces. *Chem. Rev.* **109**, 2081-2091 (2009).
- [77] A. Kühnle, Self-Assembly of Organic Molecules at Metal Surfaces. *Curr. Opin. Colloid Interface Sci.* **14**, 157-168 (2009).
- [78] S. Yoshimoto and K. Itaya, Advances in Supramolecularly Assembled Nanostructures of Fullerenes and Porphyrins at Surfaces. *J. Porphyrins Phthalocyanines* **11**, 313-333 (2007).
- [79] T. Nakanishi, N. Miyashita, T. Michinobu, Y. Wakayama, T. Tsuruoka, K. Ariga, and D.G. Kurth, Perfectly Straight Nanowires of Fullerenes Bearing Long Alkyl Chains on Graphite. *J. Am. Chem. Soc.* **128**, 6328-6329 (2006).
- [80] D. Bonifazi, H. Spillmann, A. Kiebele, M.D. Wild, P. Seiler, F. Cheng, H. Güntherodt, T. Jung, and F. Diederich, Supramolecular Patterned Surfaces Driven by Cooperative Assembly of C60 and Porphyrins on Metal Substrates. *Angew.*

- Chem., Int. Ed.* **43**, 4759-4763 (2004).
- [81] S.J.H. Griessl, M. Lackinger, F. Jamitzky, T. Markert, M. Hietschold, and W.M. Heckl, Room-Temperature Scanning Tunneling Microscopy Manipulation of Single C60 Molecules at the Liquid–Solid Interface: Playing Nanosoccer. *J. Phys. Chem. B* **108**, 11556-11560 (2004).
- [82] D. Frenkel and B. Smit, *Understanding Molecular Simulations*, 2nd ed. (Academic Press, 1996).
- [83] D.J. Wales, *Energy Landscapes* (Cambridge University Press, Cambridge, U.K., 2004).
- [84] K. Kannappan, T.L. Werblowsky, K.T. Rim, B.J. Berne, and G.W. Flynn, An Experimental and Theoretical Study of the Formation of Nanostructures of Self-Assembled Cyanuric Acid Through Hydrogen Bond Networks on Graphite. *J. Phys. Chem. B* **111**, 6634-6642 (2007).
- [85] T. Müller, T.L. Werblowsky, G.M. Florio, B.J. Berne, and G.W. Flynn, Ultra-High Vacuum Scanning Tunneling Microscopy and Theoretical Studies of 1-Halo-hexane Monolayers on Graphite. *Proc. Natl. Acad. US* **102**, 5315-5322 (2005).
- [86] S. Izvekov and G.A. Voth, Multiscale Coarse Graining of Liquid-State Systems. *J. Chem. Phys.* **123**, 134105 (2005).
- [87] G.A. Voth, *Coarse-Graining of Condensed Phase and Biomolecular Systems*, 1st ed. (CRC Press, 2008).
- [88] L.A. Girifalco, Molecular Properties of Fullerene in the Gas and Solid Phases. *J. Phys. Chem.* **96**, 858-861 (1992).
- [89] I. Paci, I. Szleifer, and M. Ratner, Structural Behavior and Self-Assembly of Lennard-Jones Clusters on Rigid Surfaces. *J. Phys. Chem. B* **109**, 12935-12945 (2005).
- [90] B. Roux and T. Simonson, Implicit Solvent Models. *Biophys. Chem.* **78**, 1-20 (1999).
- [91] C. Rey, J. García-Rodeja, L.J. Gallego, and J.A. Alonso, Clusters and Layers of C60 Molecules Supported on a Graphite Substrate. *Phys. Rev. B* **55**, 7190–7197 (1997).
- [92] R.S. Ruoff and A.P. Hickman, Van Der Waals Binding to Fullerenes to a Graphite Plane. *J. Phys. Chem.* **97**, 2494-2496 (1993).
- [93] S.S. Konyukhov, I.V. Kupchenko, A.A. Moskovsky, A.V. Nemukhin, A.V. Akimov, and A.B. Kolomeisky, Rigid-Body Molecular Dynamics of Fullerene-Based Nanocars on Metallic Surfaces. *J. Chem. Theory Comput.* **6**, 2581-2590 (2010).
- [94] S.M. Cleary, M.S. Thesis, University of New Hampshire, 2008.
- [95] C.W. Cross and B.M. Fung, A Simplified Approach to Molecular Dynamics Simulations of Liquid Crystals with Atom--Atom Potentials. *J. Chem. Phys.* **101**, 6839-6848 (1994).
- [96] Y. Tao, C. Wu, J. Eu, W. Lin, K. Wu, and C. Chen, Structure Evolution of Aromatic-Derivatized Thiol Monolayers on Evaporated Gold. *Langmuir* **13**, 4018-4023 (1997).
- [97] A. Dhirani, R. Zehner, R. Hsung, P. Guyot-Sionnest, and L. Sita, Self-Assembly of Conjugated Molecular Rods: A High-Resolution STM Study. *J. Am. Chem. Soc.* **118**, 3319-3320 (1996).

- [98] R. Mahaffy, R. Bhatia, and B. Garrison, Diffusion of a Butanethiolate Molecule on a Au{111} Surface. *J. Phys. Chem. B* **101**, 771-773 (1997).
- [99] S. Franzen, Density Functional Calculation of a Potential Energy Surface for Alkane Thiols on Au(111) as Function of Alkane Chain Length. *Chem. Phys. Lett.* **381**, 315-321 (2003).
- [100] Y. Leng, P.S. Krstic, J.C. Wells, P.T. Cummings, and D.J. Dean, Interaction Between Benzenedithiolate and Gold: Classical Force Field for Chemical Bonding. *J. Chem. Phys.* **122**, 244721 (2005).
- [101] H. Park, J. Park, A.K.L. Lim, E.H. Anderson, A.P. Alivisatos, and P.L. McEuen, Nanomechanical Oscillations in a Single-C60 Transistor. *Nature* **407**, 57-60 (2000).
- [102] C. Rogero, J.I. Pascual, J. Gomez-Herrero, and A.M. Baro, Resolution of Site-Specific Bonding Properties of C60 Adsorbed on Au(111). *J. Chem. Phys.* **116**, 832-836 (2002).
- [103] Á.J. Pérez-Jiménez, J.J. Palacios, E. Louis, E. SanFabián, and J.A. Vergés, Analysis of Scanning Tunneling Spectroscopy Experiments from First Principles: The Test Case of C60 Adsorbed on Au(111). *ChemPhysChem* **4**, 388-392 (2003).
- [104] M.P. Allen and D.J. Tildesley, in *Computer Simulation of Liquids* (Clarendon Press, Oxford, U.K., 1987), p. 21.
- [105] N. Metropolis, A.W. Rosenbluth, M.N. Rosenbluth, A.H. Teller, and E. Teller, Equation of State Calculations by Fast Computing Machines. *J. Chem. Phys.* **21**, 1087-1092 (1953).
- [106] S. Kirkpatrick, C.D. Gelatt, and M.P. Vecchi, Optimization by Simulated Annealing. *Science* **220**, 671-680 (1983).
- [107] G.J. Bubnis, S.M. Cleary, and H.R. Mayne, Self-Assembly and Structural Behavior of a Model Rigid C60-Terminated Thiolate on Au(111). *Chem. Phys. Lett.* **470**, 289-294 (2009).
- [108] J.K. Gimzewski, S. Modesti, T. David, and R.R. Schlittler, Scanning Tunneling Microscopy of Ordered C60 and C70 Layers on Au(111), Cu(111), Ag(110), and Au(110) Surfaces. *J. Vac. Sci. Technol., B* **12**, 1942-1946 (1994).
- [109] T. Sakurai, X. Wang, Q.K. Xue, Y. Hasegawa, T. Hashizume, and H. Shinohara, Scanning Tunneling Microscopy Study of Fullerenes. *Prog. Surf. Sci.* **51**, 263-408 (1996).
- [110] S. Yoshimoto, R. Narita, E. Tsutsumi, M. Matsumoto, K. Itaya, O. Ito, K. Fujiwara, Y. Murata, and K. Komatsu, Adlayers of Fullerene Monomer and [2 + 2]-Type Dimer on Au(111) in Aqueous Solution Studied by in Situ Scanning Tunneling Microscopy. *Langmuir* **18**, 8518-8522 (2002).
- [111] Y. Wang, M. Alcamí, and F. Martín, Understanding the Supramolecular Self-Assembly of the Fullerene Derivative PCBM on Gold Surfaces. *ChemPhysChem* **9**, 1030-1035 (2008).
- [112] X. Lu, M. Grobis, K.H. Khoo, S.G. Louie, and M.F. Crommie, Charge Transfer and Screening in Individual C60 Molecules on Metal Substrates: A Scanning Tunneling Spectroscopy and Theoretical Study. *Phys. Rev. B* **70**, 115418 (2004).
- [113] D. Écija, R. Otero, L. Sánchez, J.M. Gallego, Y. Wang, M. Alcamí, F. Martín, N. Martín, and R. Miranda, Crossover Site-Selectivity in the Adsorption of the Fullerene Derivative PCBM on Au(111). *Angew. Chem., Int. Ed.* **46**, 7874-7877

- (2007).
- [114] T. Chen, G. Pan, H. Yan, L. Wan, Y. Matsuo, and E. Nakamura, Substituent-Dependent Ordering of Adlayer Structures of Fullerene Derivatives Adsorbed on Au(111): A Scanning Tunneling Microscopy Study. *J. Phys. Chem. C* **114**, 3170-3174 (2010).
- [115] T. Yokoyama, S. Yokoyama, T. Kamikado, Y. Okuno, and S. Mashiko, Selective Assembly on a Surface of Supramolecular Aggregates with Controlled Size and Shape. *Nature* **413**, 619-621 (2001).
- [116] K.G. Nath, O. Ivasenko, J.A. Miwa, H. Dang, J.D. Wuest, A. Nanci, D.F. Perepichka, and F. Rosei, Rational Modulation of the Periodicity in Linear Hydrogen-Bonded Assemblies of Trimesic Acid on Surfaces. *J. Am. Chem. Soc.* **128**, 4212-4213 (2006).
- [117] S. Fortuna, D.L. Cheung, and A. Troisi, Hexagonal Lattice Model of the Patterns Formed by Hydrogen-Bonded Molecules on the Surface. *J. Phys. Chem. B* **114**, 1849-1858 (2010).
- [118] K.A.T. Silverstein, A.D.J. Haymet, and K.A. Dill, A Simple Model of Water and the Hydrophobic Effect. *J. Am. Chem. Soc.* **120**, 3166-3175 (1998).
- [119] A. Morriss-Andrews, J. Rottler, and S.S. Plotkin, A Systematically Coarse-Grained Model for DNA and Its Predictions for Persistence Length, Stacking, Twist, and Chirality. *J. Chem. Phys.* **132**, 035105-18 (2010).
- [120] A.W. Wilber, J.P.K. Doye, A.A. Louis, E.G. Noya, M.A. Miller, and P. Wong, Reversible Self-Assembly of Patchy Particles into Monodisperse Icosahedral Clusters. *J. Chem. Phys.* **127**, 085106-11 (2007).
- [121] D.C. Rapaport, Role of Reversibility in Viral Capsid Growth: A Paradigm for Self-Assembly. *Phys. Rev. Lett.* **101**, 186101 (2008).
- [122] T.A. Halgren, Merck Molecular Force Field. I. Basis, Form, Scope, Parameterization, and Performance of MMFF94. *J. Comput. Chem.* **17**, 490-519 (1996).
- [123] A. Bilic, J.R. Reimers, N.S. Hush, R.C. Hoft, and M.J. Ford, Adsorption of Benzene on Copper, Silver, and Gold Surfaces. *J. Chem. Theory Comput.* **2**, 1093-1105 (2006).
- [124] J. Wang and A. Selloni, First Principles Study of Fatty Acid Monolayers on Au(111). *J. Phys. Chem. C* **113**, 8895-8900 (2009).
- [125] D.R. Nelson and J. Toner, Bond-Orientational Order, Dislocation Loops, and Melting of Solids and Smectic-A Liquid Crystals. *Phys. Rev. B* **24**, 363-387 (1981).
- [126] J. Krim, J. Suzanne, H. Shechter, R. Wang, and H. Taub, A LEED and Neutron Diffraction Study of Hexane Adsorbed on Graphite in the Monolayer Range: Uniaxial Commensurate-Incommensurate Transition. *Surf. Sci.* **162**, 446-451 (1985).
- [127] O.G. Mouritsen and A.J. Berlinsky, Fluctuation-Induced First-Order Phase Transition in an Anisotropic Planar Model of N<sub>2</sub> on Graphite. *Phys. Rev. Lett.* **48**, 181-184 (1982).
- [128] G.H. Peters and D.J. Tildesley, Molecular Dynamics Simulations of the Melting of a Hexane Monolayer: Isotropic Versus Anisotropic Force Fields. *Langmuir* **12**, 1557-1565 (1996).

- [129] S. Priyadarshy and P. Harrowell, Rotational Relaxation in a 2D Crystal of Soft-Core Diatomic Molecules. *J. Phys. Chem.* **96**, 4040-4046 (1992).
- [130] G.J. Bubnis and H.R. Mayne, A Modeling Study of the Self-Assembly of Various Hydrogen-Bonding Fullerene Derivatives on Au(111). *J. Phys. Chem. C* **114**, 13071-13082 (2010).
- [131] S. Yoshimoto, E. Tsutsumi, R. Narita, Y. Murata, M. Murata, K. Fujiwara, K. Komatsu, O. Ito, and K. Itaya, Epitaxial Supramolecular Assembly of Fullerenes Formed by Using a Coronene Template on a Au(111) Surface in Solution. *J. Am. Chem. Soc.* **129**, 4366-4376 (2007).
- [132] M. Matsumoto, J. Inukai, E. Tsutsumi, S. Yoshimoto, K. Itaya, O. Ito, K. Fujiwara, M. Murata, Y. Murata, and K. Komatsu, Adlayers of C<sub>60</sub>-C<sub>60</sub> and C<sub>60</sub>-C<sub>70</sub> Fullerene Dimers Formed on Au(111) in Benzene Solutions Studied by STM and LEED. *Langmuir* **20**, 1245-1250 (2004).
- [133] S. Lebedkin, S. Ballenweg, J. Gross, R. Taylor, and W. Krätschmer, Synthesis of C<sub>1200</sub>: A New Dimeric [60]fullerene Derivative. *Tetra. Lett.* **36**, 4971-4974 (1995).
- [134] J. Osterodt and F. Vögtle, C<sub>61</sub>Br<sub>2</sub>: A New Synthesis of Dibromomethanofullerene and Mass Spectrometric Evidence of the Carbon Allotropes C<sub>121</sub> and C<sub>122</sub>. *Chem. Commun.* 547-548 (1996).
- [135] A.L. Balch, D.A. Costa, W.R. Fawcett, and K. Winkler, Electronic Communication in Fullerene Dimers. Electrochemical and Electron Paramagnetic Resonance Study of the Reduction of C<sub>1200</sub>. *J. Phys. Chem.* **100**, 4823-4827 (1996).
- [136] K. Komatsu, N. Takimoto, Y. Murata, T.S.M. Wan, and T. Wong, Synthesis and Properties of Dialkyl Derivatives of Di[60]fullerenylbutadiyne and Di[60]fullerenylacetylene: The Buckydumbbells. *Tetra. Lett.* **37**, 6153-6156 (1996).
- [137] T.S. Fabre, W.D. Treleaven, T.D. McCarley, C.L. Newton, R.M. Landry, M.C. Saraiva, and R.M. Strongin, The Reaction of Buckminsterfullerene with Diazotetrazole. Synthesis, Isolation, and Characterization of (C<sub>60</sub>)<sub>2</sub>C<sub>2</sub>. *J. Org. Chem.* **63**, 3522-3523 (1998).
- [138] K. Komatsu, G. Wang, Y. Murata, T. Tanaka, K. Fujiwara, K. Yamamoto, and M. Saunders, Mechanochemical Synthesis and Characterization of the Fullerene Dimer C<sub>120</sub>. *J. Org. Chem.* **63**, 9358-9366 (1998).
- [139] N. Dragoe, S. Tanibayashi, K. Nakahara, S. Nakao, H. Shimotani, L. Xiao, K. Kitazawa, K. Kitazawa, Y. Achiba, K. Kikuchi, and K. Nojima, Carbon Allotropes of Dumbbell Structure: C<sub>121</sub> and C<sub>122</sub>. *Chem. Commun.* 85-86 (1999).
- [140] N. Dragoe, H. Shimotani, M. Hayashi, K. Saigo, A. de Bettencourt-Dias, A.L. Balch, Y. Miyake, Y. Achiba, and K. Kitazawa, Electronic Interactions in a New Fullerene Dimer: C<sub>122</sub>H<sub>4</sub>, with Two Methylene Bridges. *J. Org. Chem.* **65**, 3269-3273 (2000).
- [141] N. Dragoe, H. Shimotani, J. Wang, M. Iwaya, A. de Bettencourt-Dias, A.L. Balch, and K. Kitazawa, First Unsymmetrical Bisfullerene, C<sub>121</sub>: Evidence for the Presence of Both Homofullerene and Methanofullerene Cages in One Molecule. *J. Am. Chem. Soc.* **123**, 1294-1301 (2001).
- [142] M. Fujitsuka, H. Takahashi, T. Kudo, K. Tohji, A. Kasuya, and O. Ito,



- Photophysical and Photochemical Properties of C120O, a C60 Dimer Linked by a Saturated Furan Ring. *J. Phys. Chem. A* **105**, 675-680 (2001).
- [143] Y. Zhao, Z. Chen, H. Yuan, X. Gao, L. Qu, Z. Chai, G. Xing, S. Yoshimoto, E. Tsutsumi, and K. Itaya, Highly Selective and Simple Synthesis of C<sub>2m</sub>-X-C<sub>2n</sub> Fullerene Dimers. *J. Am. Chem. Soc.* **126**, 11134-11135 (2004).
- [144] T. Ren, B. Sun, Z. Chen, L. Qu, H. Yuan, X. Gao, S. Wang, R. He, F. Zhao, Y. Zhao, Z. Liu, and X. Jing, Photochemical and Photophysical Properties of Three Carbon-Bridged Fullerene Dimers: C121 (I, II, III). *J. Phys. Chem. B* **111**, 6344-6348 (2007).
- [145] B. Sun, T. Ren, X. Miao, F. Dai, L. Jin, H. Yuan, G. Xing, M. Li, J. Dong, F. Chang, J. Hu, H. Chen, F. Zhao, X. Gao, and Y. Zhao, Isomeric and Structural Impacts on Electron Acceptability of Carbon Cages in Atom-Bridged Fullerene Dimers. *J. Phys. Chem. C* **112**, 741-746 (2008).
- [146] F. Langa, M.J. Gomez-Escalonilla, J. Rueff, T.M. Figueira Duarte, J. Nierengarten, V. Palermo, P. Samori, Y. Rio, G. Accorsi, and N. Armaroli, Pyrazolino[60]fullerene-Oligophenylenevinylene Dumbbell-Shaped Arrays: Synthesis, Electrochemistry, Photophysics, and Self-Assembly on Surfaces. *Chem. Eur. J.* **11**, 4405-4415 (2005).
- [147] V. Biju, P.K. Sudeep, K.G. Thomas, M.V. George, S. Barazzouk, and P.V. Kamat, Clusters of Bis- and Tris-Fullerenes. *Langmuir* **18**, 1831-1839 (2002).
- [148] A. Jalbout, Substitution Effects in Biphenyl Linked Fullerene Dimer Systems. *J. Comput. Theor. Nanosci* **5**, 505-511 (2008).
- [149] C.A. Martin, D. Ding, J.K. Sørensen, T. Bjørnholm, J.M. van Ruitenbeek, and H.S.J. van der Zant, Fullerene-Based Anchoring Groups for Molecular Electronics. *J. Am. Chem. Soc.* **130**, 13198-13199 (2008).
- [150] G. Teobaldi and F. Zerbetto, C60 on Gold: Adsorption, Motion, and Viscosity. *Small* **3**, 1694-1698 (2007).
- [151] R.H. Swendsen and J. Wang, Replica Monte Carlo Simulation of Spin-Glasses. *Phys. Rev. Lett.* **57**, 2607-2609 (1986).
- [152] D.J. Earl and M.W. Deem, Parallel Tempering: Theory, Applications, and New Perspectives. *Phys. Chem. Chem. Phys.* **7**, 3910-3916 (2005).
- [153] G.M. Torrie and J.P. Valleau, Monte Carlo Study of a Phase-Separating Liquid Mixture by Umbrella Sampling. *J. Chem. Phys.* **66**, 1402-1408 (1977).
- [154] J.S. van Duijneveldt and D. Frenkel, Computer Simulation Study of Free Energy Barriers in Crystal Nucleation. *J. Chem. Phys.* **96**, 4655-4668 (1992).
- [155] A.M. Ferrenberg and R.H. Swendsen, Optimized Monte Carlo Data Analysis. *Phys. Rev. Lett.* **63**, 1195-1198 (1989).
- [156] E. Gallicchio, M. Andrec, A.K. Felts, and R.M. Levy, Temperature Weighted Histogram Analysis Method, Replica Exchange, and Transition Paths. *J. Phys. Chem. B* **109**, 6722-6731 (2005).
- [157] W. Branz, N. Malinowski, H. Schaber, and T.P. Martin, Thermally Induced Structural Transition in (C60)<sub>n</sub> Clusters. *Chem. Phys. Lett.* **328**, 245-250 (2000).
- [158] J.P.K. Doye, D.J. Wales, W. Branz, and F. Calvo, Modeling the Structure of Clusters of C60 Molecules. *Phys. Rev. B* **64**, 235409 (2001).
- [159] J.M. Pacheco and J.P. Prates Ramalho, First-Principles Determination of the Dispersion Interaction Between Fullerenes and Their Intermolecular Potential.

- Phys. Rev. Lett.* **79**, 3873–3876 (1997).
- [160] F. Baletto and R. Ferrando, Structural Properties of Nanoclusters: Energetic, Thermodynamic, and Kinetic Effects. *Rev. Mod. Phys.* **77**, 371–423 (2005).
- [161] F. Calvo, Thermal Stability of the Solidlike and Liquidlike Phases of (C60)<sub>n</sub> Clusters. *J. Phys. Chem. B* **105**, 2183-2190 (2001).
- [162] H. Eisler, F.H. Hennrich, S. Gilb, and M.M. Kappes, Low Frequency Raman Active Vibrations in Fullerenes. 2. Quadrupolar Modes. *J. Phys. Chem. A* **104**, 1769-1773 (2000).
- [163] A.J. Britton, A. Rienzo, J.N. O'Shea, and K. Schulte, Charge Transfer Between the Au(111) Surface and Adsorbed C60: Resonant Photoemission and New Core-Hole Decay Channels. *J. Chem. Phys.* **133**, 094705 (2010).
- [164] J.P.K. Doye, D.J. Wales, and R.S. Berry, The Effect of the Range of the Potential on the Structures of Clusters. *J. Chem. Phys.* **103**, 4234-4249 (1995).
- [165] F. Calvo, All-Exchanges Parallel Tempering. *J. Chem. Phys.* **123**, 124106-7 (2005).
- [166] J. Kim, T. Keyes, and J.E. Straub, Generalized Replica Exchange Method. *J. Chem. Phys.* **132**, 224107 (2010).
- [167] S. Trebst, M. Troyer, and U.H.E. Hansmann, Optimized Parallel Tempering Simulations of Proteins. *J. Chem. Phys.* **124**, 174903 (2006).
- [168] D. Sabo, M. Meuwly, D.L. Freeman, and J.D. Doll, A Constant Entropy Increase Model for the Selection of Parallel Tempering Ensembles. *J. Chem. Phys.* **128**, 174109-5 (2008).